NTNU – Trondheim
Norwegian University of
Science and Technology

A study of eddy current field interactions in ferromagnetic / normal metal thin film structures and its impact on ferromagnetic resonance

Bjørn Holst Pettersen

Nanotechnology
Submission date: July 2015
Supervisor: Erik Wahlstrøm, IFY

Norwegian University of Science and Technology
Department of Physics

Abstract

This study investigates the eddy current field interaction in ferromagnetic (FM) / normal-metal (NM) thin film structures and its impact on ferromagnetic resonance (FMR). Eddy currents correspond to circulating currents induced in conductors by time varying magnetic fields. When induced in the NM layer of a FM/NM thin film structure these currents give rise to secondary inhomogeneous magnetic fields that may perturb the magnetization-dynamics in the FM layer. To probe this interaction an FMR setup was employed to both excite eddy currents in fabricated FM/NM structures and to study how the associated magnetic fields perturb the dynamics of the system. A series of thin film structures composed of patterned 10nm Permalloy / 10nm gold thin films with lateral dimensions in the micron-millimeter range were prepared using a lift off process combining optical lithography, DC magnetron sputtering and Electron beam evaporation. The FMR response of produced thin film samples was measured using a commercial electron paramagnetic resonance (EPR) setup and variations in extracted FMR lineshape parameters used to map the eddy current field interaction. To interpret obtained FMR results a theoretical model describing the impact of eddy current fields on FMR lineshapes was developed. The derived model was found to be in qualitative agreement with FMR results obtained for some, but not all analyzed thin film structures.

FMR results obtained from uncapped circular Permalloy thin film structures indicated significant eddy current field interactions in Permalloy alone. While complicating the analysis of results obtained from FM/NM thin film structures, this observation may be of interest due to the widespread use of Permalloy in magnonics related research.

In the study of FM/NM ring structures a tunable suppression of the FMR signal amplitude was observed when varying the width of the NM loop enveloping the inner FM sheet, this indicating that the FMR response can be tuned by manipulating the geometry of NM thin film structures in close proximity to FM thin films.

Results obtained from the FMR analysis of rectangular FM/NM bilayer structures indicate that the dynamics of the system is locally dominated by in-plane eddy current field components, this implying a local amplification of the applied microwave magnetic field.

Sammendrag

Dette studiet undersøker hvordan magnetiske felt indusert av virvelstrømmer i ferromagnet- (FM) / normalmetall- (NM) tynnfilmstrukturer påvirker ferromagnetisk resonans (FMR), og hvordan denne effekten kan kontrolleres. Relevante tynnfilmsystemer ble produsert ved hjelp av optisk litografi, magnetron-sputterdeponering og elektronstrålefordampning. Produserte prøver besto av mønstrede tynnfilmer bestående av 10nm Permalloy og 10nm gull med dimensjoner på mikro-/millimeterskala. FMR responsen til produserte tynnfilmstrukturer ble målt ved hjelp av et kommersielt EPR spektrometer og effekten av virvelstrøminduserte felt studert ut fra asymmetrier i målte FMR linjeformer. For å tolke FMR resultater ble en teoretisk modell utarbeidet for å beskrive hvordan virvelstrømeffekter kan påvirke FMR linjeformer. Denne modellen viste seg å være i kvalitativ overenstemmelse med FMR resultater hentet fra noen, men ikke alle målte tynnfilmstrukturer.

FMR resultatene fra sirkulær tynnfilmstrukturer av Permalloy indikerte signifikante virvelstrømeffekter i Permalloy selv uten nærliggende NM strukturer. Selv om dette vanskeliggjorde analysen av FM/NM tynnfilmstrukturer kan denne observasjonen være av interesse på grunn av den utbredte bruken av Permalloy i magnonikk relatert forskning.

I studiet av FM/NM ringstrukturer ble det observert en dempning i FMR signal amplitude for økende NM bredde. Dette indikerer at FMR responsen kan manipuleres ved å variere geometrien til NM strukutrer i nærhet av en FM tynnfilm.

Resultater oppnådd fra FMR analysen av rektangulære FM / NM bilagsstrukturer indikerte at FMR responsen er lokalt dominert av virvelstrøminsuserte magnetiske felt med komponent i tynnfilmplanet, noe som innebærer en lokal forsterkning av det påførte mikrobølgemagnetfelt.

Preface

This master's thesis was written as a part of my master's degree in nanotechnology at the Norwegian University of Science and Technology, NTNU. The documented work was conducted at the Department of Physics during the spring of 2015 under the supervision of associate professor Erik Wahlström. All investigated samples were prepared and characterized in NTNU Nanolab and the ferromagnetic resonance response of said samples analyzed at the Department of Physics.

I would first like to extend my gratitude to Erik Wahlström for his patience and support during this thesis work and during the project leading up to this thesis. Vegard Flovik is also acknowledged for his thoughts and inputs regarding the interpretation of experimental results. I would also like to thank the technical staff of NTNU NanoLab for providing instrument training and general advice, Espen Rogstad and Mark Chiappa deserving special mention. The Research Council of Norway is also acknowledged for the support to NTNU NanoLab through the Norwegiaon Micro- and Nano-Fabrication Facility, NorFab (197411/V30). Lastly, I thank my friends and family for their unconditional love and support.

Contents

Abstract iii

Sammendrag v

Preface vii

Table of Contents xi

1 Introduction 1
- 1.1 Motivation and Background . . . 1
- 1.2 Description . . . 3
- 1.3 Outline . . . 4

2 Theory 5
- 2.1 Magnetism in Condensed Matter . . . 5
- 2.2 Magnetic Interactions . . . 6
  - 2.2.1 Magnetic Dipolar Ineteraction . . . 6
  - 2.2.2 Exchange Interaction . . . 7
  - 2.2.3 Spin-orbit Interaction . . . 8
- 2.3 The Magnetic Energy Functional . . . 8
  - 2.3.1 Exchange Energy . . . 9
  - 2.3.2 Magneto Anisotropic Energy Terms . . . 9
  - 2.3.3 Magneto-crystalline Anisotropic Energy . . . 10
  - 2.3.4 Zeeman Energy . . . 11
- 2.4 Magnetization Dynamics . . . 11
  - 2.4.1 Larmor Precession . . . 12
  - 2.4.2 The Landau-Lifshitz-Gilbert Equation . . . 13
  - 2.4.3 Uniform FMR excitation in ferromagnetic thin films . . . 14
- 2.5 Electromagnetic Induction and Eddy Currents . . . 20
  - 2.5.1 Electromagnetic Induction . . . 20
  - 2.5.2 Magnetic Flux Density From a Circular Current Loop . . . 20
  - 2.5.3 Self Inductance and Phase Shifts . . . 21
  - 2.5.4 Eddy Current Induction in a NM Thin Film Plane . . . 22

3 Eddy Current Field Perturbations in FMR Lineshapes **25**
3.1 Experimental Setup . . . 25
3.2 Electromagnetic Loss and FMR . . . 27
3.2.1 Dielectric Loss . . . 27
3.2.2 Joule Loss . . . 27
3.2.3 Magnetic Loss . . . 28
3.3 Eddy Current Effects in FMR Lineshapes . . . 29

4 Experimental Materials, Methods and Procedures **33**
4.1 Overview . . . 33
4.2 Fabrication Techniques . . . 35
4.2.1 Photolithography . . . 35
4.2.2 Physical Vapor Deposition . . . 36
4.2.3 Die Separation . . . 37
4.3 Fabrication Procedure . . . 38
4.3.1 Substrate Preparation . . . 38
4.3.2 Photolithography . . . 38
4.3.3 Photomask . . . 41
4.3.4 Thin Film Deposition . . . 42
4.3.5 Lift Off . . . 45
4.3.6 Die Separation . . . 45
4.4 Characterization . . . 46
4.4.1 Atomic Force Microscopy . . . 46
4.4.2 Ferromagnetic Resonance Spectroscopy . . . 47
4.4.3 FMR Procedures . . . 50
4.5 Data Analysis . . . 53

5 Results and Discussion **57**
5.1 Sample Fabrication . . . 58
5.1.1 Circular Disk Structures . . . 58
5.1.2 Ring Structures . . . 59
5.1.3 Rectangular Samples . . . 60
5.1.4 AFM Characterization Results . . . 62
5.2 Ferromagnetic Resonance Results . . . 63
5.2.1 Circular Permalloy Samples . . . 63
5.2.2 Circular Ring Structures . . . 69
5.2.3 Rectangular Py/Au Bilayer Structures . . . 73
5.2.4 Circular Py/Au Thin Film Structures . . . 84

6 Conclusion **87**
6.1 Further Work . . . 88

Bibliography **91**

A Power dissipation of time harmonic EM fields **95**

B Photo Mask **97**
B.1 Mask Design 97
B.2 Mask Layout 99

C Thin film growth parameters **103**

D Supplementary data **109**
D.1 AFM thickness measurements 109
D.2 Supplementary FMR parameterization data 111

E Materials **115**
E.0.1 Intrinsic Silicon Substrates 115
E.0.2 List of Materials 115

Acronyms

AFM	Atomic Force Microscopy
Au	Gold
DC	Direct current
DI-water	Deionized water
EBR	Edge Bead Remover
EPR	Electron Paramagnetic Resonance
FM	Ferromagnet(ic)
FMR	Ferromagnetic resonance
IPA	Isopropyl alcohol
NM	Normal-metal
Py	Permalloy ($Ni_{0.81}Fe_{0.19}$)
RF	Radio frequency
RMS	Root mean square
SEM	Scanning Electron Microscope

Chapter 1

Introduction

1.1 Motivation and Background

Innovations in thin film processing combined with an ever growing need for high frequency/frequency tunable/low power electronic components have in recent decades sparked a flurry of research into the emerging field of spintronics/magnonics. Spintronics/magnonics based technologies offer functionalities beyond current semiconductor based devices by exploiting the electron spin degree of freedom to either manipulate currents in conductors or to excite and manipulate spin-waves [23, 33]. Novel spintronics based device concepts, examples being magnetic random access memory (MRAM), spin-torque MRAM and spin torque nano oscillators [1], typically operate at microwave frequencies and rely on the magneto-dynamical properties of multilayers consisting of ferromagnetic (FM) and normal-metal (NM) thin films [22]. As such, the study of physical phenomena affecting the magnetization dynamics of such multilayer structures is of importance for the continued advancement of spintronics/magnonics based technologies.

Ferromagnetic resonance (FMR) spectroscopy is among the most common techniques for probing both the static and dynamic properties of nanoscale magnetic materials and multilayers [26, 35]. In an FMR experiment the magneto-dynamical response of the studied sample is probed by applying a radio frequency (RF) magnetic field in conjunction with an orthogonal static magnetic field. Depending on the FMR setup either the static field magnitude or RF field frequency is tuned to vary the coupling between excitable magneto-dynamical modes and the applied rf field. By measuring the corresponding change in absorbed RF power as a function of the varied experimental parameter one may probe the spin-wave manifold of the studied system, this providing a wealth of information regarding its static and dynamic magnetic properties [7].

When FMR is employed in the study of FM/NM multilayers the applied RF field will interact not only with FM thin films but also with incorporated NM layers.

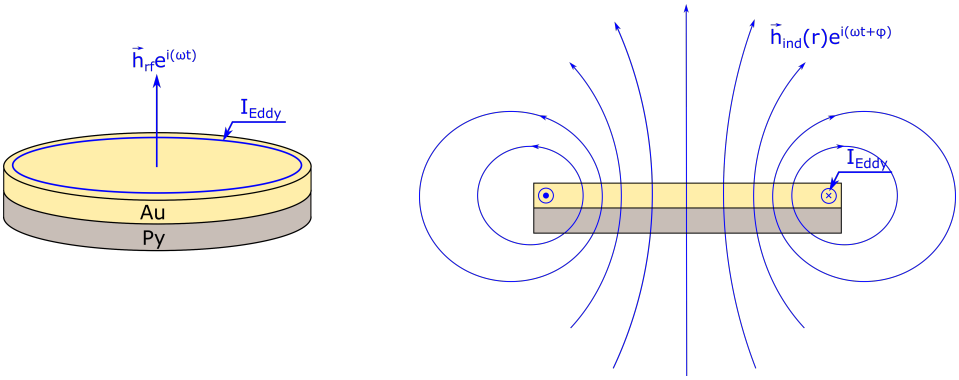

Figure 1.1: (Left) Illustration of induced eddy current in a circular FM/NM bilayer structure. As shown the induced current density is expected to be largest along the sample edge [21,27]. (Right) Sketched eddy current field distribution when assuming the induced current to primarily flow along the sample edge. The thickness of depicted thin films has been exaggerated.

This interaction may excite eddy currents in the NM layer by virtue of electromagnetic induction. Eddy currents correspond to circulating currents induced in conductive materials by time varying magnetic fields. As Figure 1.1 illustrates, these currents flow in closed loops at right angles to the applied field, and give rise to secondary inhomogeneous magnetic field components, phase shifted relative to the applied pumping field. Induced secondary magnetic fields may in turn interact with FM films in close proximity to the NM, thus altering the dynamics response of the system.

While the effects of eddy currents on FMR are well known for film thicknesses above the electromagnetic skin depth (∼800nm for Au at 10GHz [10]), these effects are usually neglected when considering thin film systems of a thickness well below this depth. As such, a limited number of papers have been published on eddy current effects in the sub skin-depth thickness regime, most of which treating eddy current screening effects rather than the effect of induced secondary magnetic fields on FMR [8, 13, 24, 25]. A recently published study conducted at NTNU sought to bridge this gap by focusing on how eddy current induced magnetic fields perturb FMR lineshapes in FM/NM thin film bilayer structures [10]. In these experiments a cavity based FMR setup was employed to direct a magnetic flux along the thin film normal of rectangular 10nm Py/10nm Au thin film bilayers, this to both excite eddy currents in the Au thin film plane while also studying its impact on the resonance condition of the underlying ferromagnetic thin film. These experiments found that the inclusion of an Au capping layer induced significant perturbations in recorded FMR absorption curves for sample geometries with lateral dimensions above 1mm^2 and for NM layers with a thicknesses below 50nm. These perturbations were argued to be the results of induced eddy current fields interacting with

the FM thin film, this indicating that the system dynamics is defined by the interplay of applied RF fields and induced magnetic fields when the RF field has an appreciable component directed along the NM normal axis. Furthermore, this field coupling was observed to be tunable as the degree to which FMR lineshapes were perturbed depended on both sample geometry and its orientation with respect to applied fields. This tunability could prove useful for spintronics applications as eddy current engineering would allow one to manipulate the local field geometry and phase of an applied homogeneous magnetic field. An improved understanding of eddy current effects in FMR is also of importance from a scientific standpoint as it does significantly affect FMR results given the right experimental conditions. Further knowledge regarding when eddy current effects become significant is therefore also a topic of interest.

1.2 Description

This work aims to further study the eddy current field interaction by employing the following methods of inquiry.

The primary component of this work is experimental. To study how the eddy current field interaction may be manipulated a range of FM/NM thin film geometries were prepared using a lift off process combining optical lithography, DC magnetron sputtering and electron-beam evaporation. As compared to the scribing process applied in Flovik et.al's [10] initial study this fabrication procedure provides an enhanced degree of freedom regarding the types of thin film geometries that may be studied. By manipulating the paths in which eddy currents could flow it was anticipated that one would be able to isolate different aspects of the eddy current field interaction, which in turn could provide valuable information regarding the system dynamics. Prepared samples were analyzed using the same commercial EPR setup as that used during Flovik et.al's [10] initial study.

In Flovik et.al's [10] work on this topic a simplified model was adopted to describe how eddy current induced magnetic fields affect FMR. While this model produced an expression for FMR lineshapes of correct functional form, it did not explicitly correlate curve fitted parameters to physical system parameters. Efforts were therefore made to improve this model in order to more easily extract insights from experimental results.

1.3 Outline

This masters thesis is structured as follows:

Chapter 2 presents the basic theory of magnetism, magnetization dynamics and electromagnetic induction. A general introduction to magnetic moments, how these interact and the free energy terms defined by these interactions is first given. Subsequent sections describes the magnteic response of ferromagnetic thin films to time varying magnetic fields and the physical principles governing ferromagnetic resonance. The remaining portion of chapter 2 is devoted to electromagnetic induction and eddy currents.

Chapter 3 aims to explain how inhomogeneous eddy current fields may affect the FMR response of FM/NM thin film structures. In doing so a new model explaining the induced perturbation of FMR absorption curves is presented.

Chapter 4 first presents the primary fabrication techniques and procedures used to manufacture the thin film systems studied in this report. Used characterization techniques are then presented, the main emphasis here being on the used cavity-FMR setup. A description of used materials will also be given after discussing how the obtained experimental data was analyzed.

Chapter 5 first presents the thin film geometries chosen in this study followed by discussion regarding the quality of realized FM/NM geometries. Subsequent sections provides a discussion regarding obtained FMR spectroscopy results for each sample series.

Chapter 2

Theory

This chapter provides the theoretical foundation for a discussion of eddy current field interactions in FMR. A general introduction to magnetism in condensed matter is first presented where the main emphasis is on the magnetic interactions defineing the energy landscape of a ferromagnet. Subsequent sections treat the physical phenomena governing ferromagnetic resonance in thin films subject to homogeneous RF magnetic fields. Remaining sections are devoted to a general discussion of electromagnetic induction, eddy currents and resulting inhomogeneous magnetic fields.

2.1 Magnetism in Condensed Matter

All materials display magnetic properties in that they to some extent respond to applied magnetic fields. This response entails the alignment of intrinsic or induced magnetic moments associated with the charged particles making up the material. For an atom/ion the associated magnetic moment has two primary sources: The orbital angular momentum of electrons bound to the atomic core, $\mathbf{L}$, and the intrinsic spin angular momentum of these electrons, $\mathbf{S}$ [14]. These angular momenta give rise to a total angular momentum, $\mathbf{J} = \mathbf{L} + \mathbf{S}$, with an associated magnetic moment given by [3]

$$\boldsymbol{\mu} = -|\gamma_J|\mathbf{J} \tag{2.1}$$

Here $\gamma_J = -g_J|e|/2m_e$ is the gyromagnetic ration, e being the electron charge, m_e the electron rest mass and g_J a factor describing the relative contributions from $\mathbf{L}$ and $\mathbf{S}$ ($g_J \approx 2$ for an isolated electron spin).

The magnetic state of an ensemble of magnetic moments is characterized by its magnetization, the average alignment of moments per unit volume V:

$$\mathbf{M} = \frac{\sum_i \boldsymbol{\mu_i}}{V} \tag{2.2}$$

As a magnetic ensemble strives towards lower energy states the resulting magnetic configuration is defined by the magnetic interactions present in the system and their respective contributions to the magnetic free energy. As these interactions are intimately linked to the electronic structure of a material different classes of matter exhibit different magnetic properties. The different classes of magnetism, these being diamagnetism, papamagnetism, ferromagnetism, ferrimagnetism and anti-ferromagnetism, are in part distinguished by differences in their magnetic response to applied magnetic fields, and their magnetic state in the absence of such fields.

The primary property of ferromagnetic materials is the spontaneous ordering of magnetic moments in the absence of externally applied magnetic fields, provided that the system temperature lies below the Curie temperature [3]. This spontaneous magnetization is attributed to a strong coupling of neighboring electron spins trough the exchange interaction, as discussed shortly, this resulting in their local alignment. While strong, the forces associated with the exchange interaction are also very local. As such, weaker but more long ranged magnetic interactions usually define the magnetic state of a ferromagnet on a macroscopic scale, this generally resulting in the formation of magnetic domains within which the local magnetization reaches the saturation value [3]. An understanding of the dominant magnetic interactions and their contributions to the magnetic free energy functional is therefore necessary as these define the magnetic evolution of a ferromagnet both in the static limit and in response to dynamic magnetic fields.

2.2 Magnetic Interactions

The following sections will introduce the primary magnetic interactions affecting magnetic order in condensed matter as associated energies define the energy landscape of a material. Emphasis is here put on interactions affecting magnetic order in ferromagnetic materials.

2.2.1 Magnetic Dipolar Ineteraction

Consider two magnetic dipoles $\boldsymbol{\mu}_1$ and $\boldsymbol{\mu}_2$ separated by a distance $\mathbf{r}$. These dipoles will each give rise to a magnetic field that will interact with neighboring poles. For such a pair the associated energy will be given by [3]

$$E = \frac{\mu_0}{4\pi r^3}[\boldsymbol{\mu}_1 \cdot \boldsymbol{\mu}_2 - \frac{3}{r^2}(\boldsymbol{\mu}_1 \cdot \mathbf{r})(\boldsymbol{\mu}_2 \cdot \mathbf{r})] \tag{2.3}$$

As indicated the magnetic dipolar energy depends on the separation and alignment of interacting magnetic dipoles. For two electron spins separated by $r \approx 1$Å the energy reduction from an aligned configuration is in the order of 10^{-6}eV which is equivalent to a thermal energy of 1K [3]. As the Curie temperature, above which ferromagnetic order is lost, exceeds room temperature in common ferromagnetic materials the dipolar interaction is too weak to account for the ordering of most

magnetic materials. It does however give rise to the demagnetization field dictating magnetic orientation in thin films, while also affecting the shape of spin wave dispersion relations [7].

2.2.2 Exchange Interaction

The exchange interaction constitutes the primary mechanism by which long range magnetic order is achieved in ferromagnetic materials. This interaction and the corresponding exchange energy is a direct consequence of the Pauli exclusion principle which prevents electrons of parallel spin from occupying the same orbital state [4] [3]. The energy of an electron pair is by this principle dependent on the alignment of their spins as this determins the allowed electron states, and thus their mutual effective Coulomb repulsion. In the Heisenberg model the exchange energy is described by the Hamiltonian [3]

$$\boldsymbol{\mathcal{H}_{ex}} = -\frac{1}{2}\sum_{i<j} J_{ij}\mathbf{S}_i \cdot \mathbf{S}_j \tag{2.4}$$

where the sign and magnitude of J_{ij}, the exchange integral, determines the configuration of neighboring electron spins. In ferromagnetic materials the exchange integral assumes a positive sign, favoring the alignment of nearest neighboring spins $\mathbf{S}_i$ and $\mathbf{S}_j$, as this configuration reduces the energy of the system. A negative sign

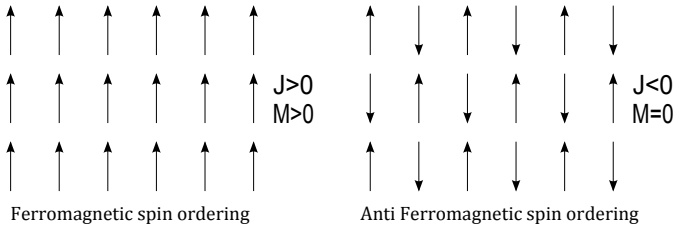

Figure 2.1: Ordering of magnetic moments below the Curie temperature, as determined by the sign of the exchange integral. The image to the left illustrates the parallel orientation of spins common for ferromagnets whereas the left image illustrates the ordering of anti-ferromagnetic materials. As indicated ferromagnetic ordering results in a net magnetization of the material, whereas an anti-parallel configuration of spins does not.

favors an anti-parallel alignment where spins are oriented in an alternating fashion as illustrated in Figure 2.1. In a macroscopic treatment of ferromagnetism where the discrete nature of the crystal lattice is ignored and the magnetization treated as a continuous vector field rather than the sum of quantized magnetic moments, the exchange energy density is given by [12] [3]

$$\epsilon_{ex} = \frac{A}{V}\int_V (\nabla \cdot \mathbf{m})^2 dV \qquad \text{where} \qquad \mathbf{m} = \frac{\mathbf{M}}{M_S} \tag{2.5}$$

$A = 2JS^2z/a$[1] begin the exchange stiffness constant and M_S the saturation magnetization of the material. While strong, the exchange interaction is very local as it relies on the overlap of electron wave functions.

2.2.3 Spin-orbit Interaction

As discussed in section 2.1 the magnetic moment of an electron has two principal sources: The orbital angular momentum of the electron, **L**, and its spin angular momentum, **S** [3]. These two angular momenta in turn interact through their associated magnetic moments and give rise to a splitting of degenerate atomic energy states based their mutual alignment [4]. This coupling is referred to as the spin-orbit interaction.

For atoms in a crystal lattice the orientation of atomic orbitals will depend on the atomic ordering within the crystal. This produces a directional dependence in orbital angular momentum states matching the symmetry of the crystal. Consequently, the energy of an electron spin will depend on its orientation relative to the lattice, by virtue of the spin-orbit interaction, thus introducing one source of magnetic anisotropy [34]. In addition, by linking the spin system to the crystal lattice the spin-orbit interactions provides a channel for energy transfer between the two systems. As will be discussed in subsequent sections this represents a key mechanics in the intrinsic damping of spin-wave excitations in ferromagnetic materials.

2.3 The Magnetic Energy Functional

As discussed in the previous section, magnetic moments in solid materials do not solely interact with applied magnetic fields, but will also have energies dependent on their orientation with respect to neighboring moments and the local environment. These interactions define the magnetic energy density of the system ϵ_{Total}. The effective magnetic field $\mathbf{H_{eff}}$ acting on the magnetization may be found from the functional derivative of the total energy density with respect to the normalized magnetization vector $\mathbf{m}(\mathbf{r}) = \mathbf{M}(\mathbf{r})/M_S$, M_S being the saturation magnetization [12]:

$$\mathbf{H_{eff}} = -\frac{1}{\mu_0}\frac{\partial \epsilon_{Total}}{\partial \mathbf{m}} \tag{2.6}$$

For ferromagnetic materials the magnetic energy functional is generally written as [35]

$$\epsilon_{Total} = \epsilon_{Zeeman} + \epsilon_{Ex} + \epsilon_{Crystal} + \epsilon_D \tag{2.7}$$

where individual components represent; ϵ_{Zeeman} - the Zeeman energy, ϵ_{Ex} - the exchange energy, $\epsilon_{Crystal}$ - the crystalline anisotropy energy and ϵ_D the demagnetization energy. The various components of the energy functional will be briefly introduced in the following sections.

[1] Here J represents the exchange integral, S=1/2, z the number of sites in the unit zell containing unpaired electrons and a the lattice spacing

2.3.1 Exchange Energy

The exchange energy is as already discussed in section 2.2.2 given by

$$\epsilon_{ex} = \frac{A}{V}\int_V (\nabla \cdot \mathbf{m})^2 dV \tag{2.8}$$

2.3.2 Magneto Anisotropic Energy Terms

While the exchange energy favors the collective alignment of spins along a unique direction, this direction has yet to be defined. Experiments have shown that for most materials there exists an easy axis of magnetization along which spins tend to align. Consequently there also exists a hard axis of magnetization along which magnetic alignment is less energetically favorable [34]. The principal contributing factors to the observed magnetic anisotropy are related to the crystal structure of the sample, its magnetic state and its geometry. Corresponding energy contributions to the magnetic energy functional will be discussed in subsequent sections, these being the demagnetization energy and magneto crystalline anisotropic energy.

Demagnetization Energy

The demagnetization energy follows directly from Gauss' law of flux conservation ($\nabla \cdot \mathbf{B} = 0$) which when combined with $\mathbf{B} = \mu_0(\mathbf{H} + \mathbf{M}$ results in the following expression [3]:

$$\nabla \cdot \mathbf{H} = -\nabla \cdot \mathbf{M} \tag{2.9}$$

At the surface of a magnetized body there will be a divergence in the magnetization resulting in an opposite divergence in the magnetic field, as indicated by equation (2.9). The magnetic field caused by this divergence, from heron referred to as the demagnetization field $\mathbf{H_D}$, can be seen as arising from virtual magnetic monopoles generated at the surface wherever $\nabla \cdot \mathbf{M} \neq 0$. The energy associated with demagnetization accounts for energy storage in stray magnetic fields both inside and outside the ferromagnet, and is represented by [3]:

$$E_D = -\frac{\mu_0}{2}\int_V \mathbf{M} \cdot \mathbf{H_D} dV \tag{2.10}$$

V being the volume of the ferromagnet. As the demagnetization field can be seen as arising from magnetic poles generated at the surface of the magnetic body, $\mathbf{H_D}$ and the associated energy depends on both sample geometry and magnetization state as these parameters define the magnetic divergence at the bounding surface. For an arbitrarily shaped body the demagnetization field generally shows a complex dependence on position, complicating the calculation of its associated energy. The problem is, however, simplified for homogeneously magnetized ellipsoids in which case $\mathbf{H_D}$ becomes homogeneous. The geometric dependence is for ellipsoidal samples described by the demagnetization tensor $\hat{\mathbf{N}}$:

$$\mathbf{H_D} = -\hat{\mathbf{N}}\mathbf{M} \tag{2.11}$$

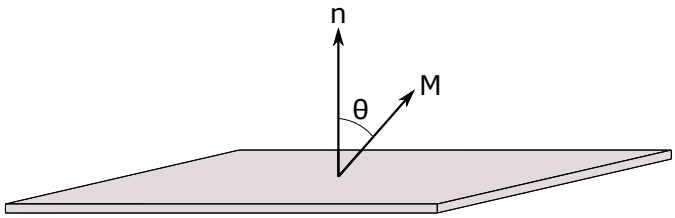

Figure 2.2: Out of plane magnetization in a homogeneously magnetized thin film

For an ellipsoid whose principal axes are aligned along the (xyz) axes of a Cartesian coordinate system the demagnetization tensor may be diagonalized and satisfies $Tr(\bar{\mathbf{N}}) = N_x + N_y + N_z = 1$. In ferromagnetic thin films whose lateral extent is much greater than the film thickness the geometry of the sample is well approximated by an ellipsoid where two axes are taken to be infinite. Applying this approximation while assuming the z-axis to be oriented along the film plane normal yields the demagnetization tensor; $N_x = N_y = 0$, $N_z = 1$, which when substituted into equation (2.11) yields

$$\mathbf{H_D} = M_z\hat{\mathbf{z}} = M_z\hat{\mathbf{n}} \tag{2.12}$$

The resulting demagnetization energy is found by solving equation (2.10) in a cylindrical coordinate system;

$$\epsilon = \frac{\mu_0}{2} M_S^2 \cos^2(\theta) \tag{2.13}$$

where M_S is the saturation magnetization and θ the angle enclosed by $\mathbf{M}$ and the plane normal as illustrated in Figure 2.2. As equation (2.13) indicates the demagnetization energy favors an in plane orientation of the magnetization for ferromagnetic thin films.

2.3.3 Magneto-crystalline Anisotropic Energy

The magneto-crystalline anisotropic energy originates from the spin-orbit interaction, as discussed in section 2.2.3, and depends on the orientation of electron spins relative to the crystallographic axes of the material. This energy density is defined as the energy per unit volume needed to rotate the magnetization from the easy axis of magnetization. For a ferromagnet of cubic crystal symmetry this energy can be expressed as an even power series of α_i, the directional cosines of the normalized magnetization $\mathbf{m}$ with respect to the crystallographic axes, which to first order yields [5]

$$\epsilon_{crystal} = K_1[(\alpha_x\alpha_y)^2 + (\alpha_y\alpha_z)^2 + (\alpha_z\alpha_x)^2] + K_2(\alpha_x\alpha_y\alpha_z)^2 \tag{2.14}$$

where K_1 and K_2 represents material specific anisotropy constants of units energy/volume.

For Permalloy, the $Ni_{0.81}Fe_{0.19}$ alloy used in this study, the first order anisotropy

constants has been found to approach zero for Ni compositions in the 80% range [37]. Furthermore, magnetron sputter deposition was used to grow the Permalloy thin films studied in this thesis, a deposition technique known to produce polycrystalline films [29]. This should in principle further reduce the magneto-crystalline anisotropy contribution to the magnetic energy functional, even if grains are preferentially oriented with respect to the (100) oriented silicon substrate. The magneto-anisotropic contribution to the magnetic energy functional is therefore expected to not dominate, allowing one to neglect its contribution to the effective magnetic field affecting the resonance condition in the studied thin films.

2.3.4 Zeeman Energy

The Zeeman energy describes the potential energy of a magnetized object interaction with an externally applied magnetic field **H**. This energy is for an isolated electron spin given by [3]

$$E = -\mu_0 \boldsymbol{\mu}_S \cdot \mathbf{H} \tag{2.15}$$

$\boldsymbol{\mu}_S$ being the magnetic moment of the spin. For a ferromagnet with local magnetization $\mathbf{M}(\mathbf{r})$ the Zeeman energy density equals

$$\epsilon_{Zeeman} = -\frac{1}{V}\int_V \mathbf{M}(\mathbf{r}) \cdot \mathbf{H} dV \tag{2.16}$$

V being the volume of the magnetic body. The Zeeman energy favors the alignment of the magnetization in the direction of the applied magnetic field.

2.4 Magnetization Dynamics

While the dynamic response of a ferromagnet to transient magnetic fields, and associated resonance phenomena, are only fully described in terms of quantum mechanical spin wave excitations [7], thin film systems are for most purposes adequately described macroscopically in a quasi classical framework [35]. In the following introduction to ferromagnetic resonance this quasi classical formalism will be employed as it is more in line with the scope of this thesis.

The following discussion will first present the equations of motion for a single classical electron spin in a static magnetic field, this to illustrate the time evolution of an isolated magnetic moment. Subsequent sections will treat the dynamic response of a ferromagnetic thin film to a weak, spatially homogeneous, time harmonic magnetic field after first presenting the relevant equations of motion. Presented results will form the basis for understanding the FMR spectroscopy data obtained in this thesis.

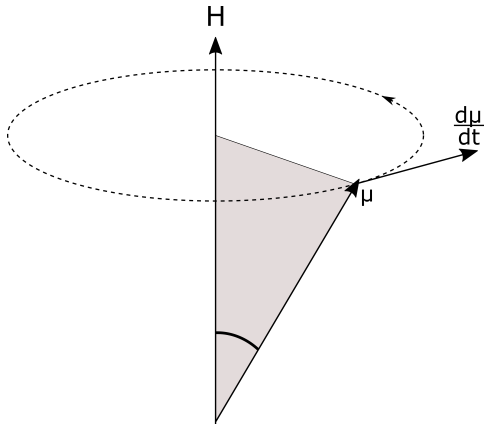

Figure 2.3: Scematic illustration of the precessional motion induced in $\boldsymbol{\mu}_S$ by an externally applied magnetic field $\mathbf{H}$

2.4.1 Larmor Precession

The energy of an isolated electron spin subject to a static magnetic field $\mathbf{H}$ is as described in section 2.3.4 given by the Zeeman energy

$$E = -\mu_0 \boldsymbol{\mu}_S \cdot \mathbf{H} \tag{2.17}$$

where μ_S is the magnetic moment associated with the electron[2]. By virtue of energy minimization this should result in the spin aligning with the magnetic field. However, as discussion in section 2.1 the magnetic moment of an isolated electron is related to its spin angular momentum $\mathbf{S}$

$$\boldsymbol{\mu}_S = -|\gamma_S|\mathbf{S} \tag{2.18}$$

on which the field will exert a torque given by [34]

$$\boldsymbol{\tau} = \mu_0[\boldsymbol{\mu}_S \times \mathbf{H}] \tag{2.19}$$

Since the torque acting on an object is equal to the rate of change in the objects angular momentum, equations (2.18) and (2.19) may be combined as

$$\frac{\partial \boldsymbol{\mu}_S}{\partial t} = -\mu_0|\gamma_S|[\boldsymbol{\mu}_S \times \mathbf{H}] \tag{2.20}$$

where the rate of change in the magnetic moment is perpendicular to the plane spanned by $\mathbf{H}$ and $\boldsymbol{\mu}_S$. The resulting motion is schematically illustrated in Figure 2.3 where the applied field is seen to induce a precession in $\boldsymbol{\mu}_S$ around $\mathbf{H}$.

[2]In the current semi-classical treatment the spin angular momentum and its associated magnetic moment is interpreted as the polarization vector associated with the expectation values of the quantum mechanical spin operator [14]

Solving equation (2.20) yields the Lamour frequency [34];

$$\omega_L = \mu_0 |\gamma_S| H \tag{2.21}$$

which describes the relation between the magnitude of the magnetic field felt by a magnetic moment and the resulting frequency of precession. Larmor precession is the governing principle behind spectroscopy techniques relying on the interactions between magnetic moments and magnetic fields, prime examples being nuclear magnetic resonance (NMR), electron paramagnetic resonance (EPR) and ferromagnetic resonance (FMR) [3].

2.4.2 The Landau-Lifshitz-Gilbert Equation

Moving over from a single electron spin to that of a macrospin, the time evolution of the magnetization $\mathbf{M}(\mathbf{r}, t)$[3] to both static and temporal magnetic fields is generally modeled by the Landau-Lifshitz-Gilbert equation [12]

$$\frac{\partial \mathbf{M}}{\partial t} = -\mu_0 |\gamma| \mathbf{M} \times \mathbf{H_{eff}} + \frac{\alpha}{M_S} [\mathbf{M} \times \frac{\partial \mathbf{M}}{\partial t}] \tag{2.22}$$

Here γ represents the gyromagnetic ratio, M_S the saturation magnetization, α the Gilbert damping parameter and $\mathbf{H_{eff}}$ the effective magnetic field introduced in section 2.3. As shown in Figure 2.4 the first term in equation (2.22) corresponds to the torque exerted on the magnetization vector by the effective field $\mathbf{H_{eff}}$ and describes the Lamour precession of $\mathbf{M}$ around $\mathbf{H_{eff}}$. The second term constitutes a phenomenological damping torque responsible for the magnetization eventually relaxing towards the effective field. The LLG equation treats the viscous damp-

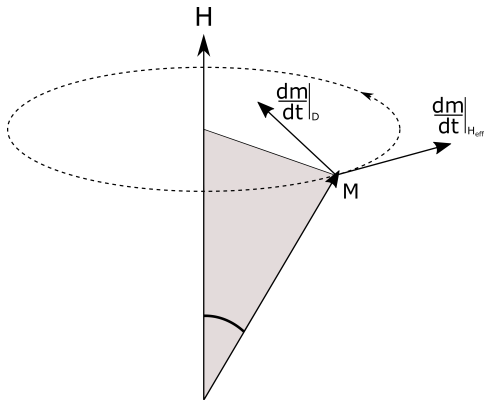

Figure 2.4: Schematic illustration of magnetic time evolution as described by the Landau-Lifshitz-Gilbert (LLG) equation

ing of magnetization in a phenomenological manner where the Gilbert damping

[3]The local magnetization field is here defined as the expectation value of the magnetic moment arising from the spin/orbital momentum of electrons, averaged over a few unit cells [12]

parameter α represents a measure of the energy transfer rate between magnetic degrees of freedom and other energy reservoirs. The various microscopic mechanisms contributing to Gilbert damping are commonly divided into intrinsic and extrinsic processes. Unavoidable processes such as the direct coupling of magnons to the crystal lattice via the spin-orbit interaction and the excitation of eddy currents in conducting ferromagnets are termed intrinsic. Extrinsic contributions to Gilbert damping include processes mediated by sample imperfections or interface effects such as magnon scattering.

2.4.3 Uniform FMR excitation in ferromagnetic thin films

As the Landau-Lifshitz-Gilbert equation constitutes a coupled non-linear second order differential equation, analytical solutions for the magnetic time evolution are only attainable for a limited number of systems. This section will present the solution for one such system; when considering the magnetic time evolution of a homogeneously magnetized ferromagnetic thin film subject to a weak, spatially homogeneous, time harmonic magnetic field:

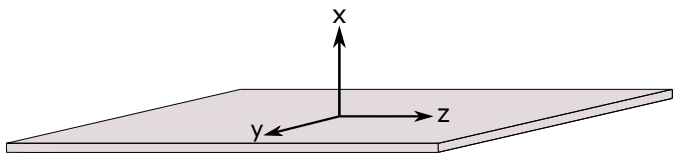

Figure 2.5: Orientation of ferromagnetic thin film

Consider a ferromagnetic thin film, as depicted in Figure 2.5, where the film plane normal is oriented along the $\hat{\boldsymbol{x}}$ direction of a Cartesian coordinate system. To study the dynamics of the system a static magnetic field $\mathbf{H_0}$ is applied along the z-axis, in the thin film plane, in conjunction with a weak alternating high frequency magnetic field $\mathbf{h_{rf}}$. The static magnetic field serves to homogeneously magnetize the ferromagnet whereas the time varying field perturbs the magnetization from its equilibrium position, inducing a precession in magnetization. Both fields are assumed to be spatially homogeneous such that the magnetization can be treated as a vector quantity rather than a spatially dependent magnetization field. Encountered field quantities may thus be written as

$$\mathbf{H(t)} = \mathbf{H_0} + \mathbf{h_{rf}} \cdot e^{i(\omega t)} = H_0 \hat{\boldsymbol{z}} + \begin{pmatrix} h_x \\ h_y \\ h_z \end{pmatrix} \cdot e^{i(\omega t)} \tag{2.23}$$

$$\mathbf{M(t)} = \mathbf{M_0} + \mathbf{m} \cdot e^{i(\omega t)} = M_0 \hat{\boldsymbol{z}} + \begin{pmatrix} m_x \\ m_y \\ m_z \end{pmatrix} \cdot e^{i(\omega t)} \tag{2.24}$$

where $\mathbf{m}$ is the perturbation in $\mathbf{M_0}$, induced by $\mathbf{h_{rf}}$. The macroscopic precession in magnetization is here assumed to show the same frequency dependence as the

perturbing field as this is the only encountered time constant in the system. Furthermore it will be assumed that the field associated with the magneto anisotropic energy is negligible, as will be the case for the Permalloy thin films studied in this thesis. This leaves only the field contributions from the Zeeman and demagnetization energy as a homogeneous magnetization is assumed, thus producing an exchange field contribution equal to zero. The effective field acting on the magnetization may under the stated constraints be expressed as the sum of applied fields and the demagnetization field described in section 2.3.2:

$$\mathbf{H_{eff}} = \mathbf{H(t)} - \hat{\mathbf{N}}\mathbf{M(t)} \tag{2.25}$$

Substituting equations (2.23), (2.24) and (2.25) into the Landau-Lifshitz-Gilbert equation yields the following set of equations [15]:

$$\begin{aligned} i\omega m_x =& -\mu_0|\gamma|[m_y(H_0 - N_z M_0 + h_z(t) - N_z m_z(t)) - (m_z(t) + M_0)(h_y - N_y m_y)] \\ &+ \frac{i\alpha\omega}{M_S}[m_y(t)m_z - (m_z(t) + M_0)m_y] \end{aligned} \tag{2.26}$$

$$\begin{aligned} i\omega m_y =& -\mu_0|\gamma|[(m_z(t) + M_0)(h_x - N_x m_x) - m_x(H_0 - N_z M_0 + h_z(t) - N_z m_z(t))] \\ &+ \frac{i\alpha\omega}{M_S}[(m_z(t) + M_0)m_x - m_x(t)m_z] \end{aligned} \tag{2.27}$$

$$\begin{aligned} i\omega m_z =& -\mu_0|\gamma|[m_x(t)(h_y - N_y m_y) - m_y(t)(h_x - N_x m_x)] \\ &+ \frac{i\alpha\omega}{M_S}[m_x(t)m_y - m_y(t)m_x] \end{aligned} \tag{2.28}$$

where $m_i(t) = m_i \cdot e^{i(\omega t)}$. For a weak pumping field relative to the applied static field[4] one may assume that the induced magnetic perturbation $\mathbf{m}$ is small compared to the magnetization magnitude M_0, that is $|\mathbf{h_{rf}}| \ll H_0$ and $|\mathbf{m}| \ll M_S$ such that $M_0 \simeq M_S$. This allows one to consider only linear terms in h and m:

$$\omega_M h_x = -i\omega m_x + [\omega_H + (N_y - N_z)\omega_M - i\alpha\omega]m_y \tag{2.29}$$

$$\omega_M h_y = [\omega_H + (N_x - N_z)\omega_M - i\alpha\omega]m_x + i\omega m_y \tag{2.30}$$

where the following abbreviations have been used:

$$\omega_M = \mu_0|\gamma|M_s \tag{2.31}$$

$$\omega_H = \mu_0|\gamma|H_0 \tag{2.32}$$

As shown, all terms of m_z disappear when linearizing the LLG equation as it implicitly assumes a negligible perturbation in the magnetization direction relative to the saturation magnetization. From equations (2.29) and (2.30) one obtains a matrix relating the field perturbation to the resulting perturbation in magnetization

$$\omega_M \begin{pmatrix} h_x \\ h_y \end{pmatrix} = \begin{pmatrix} -i\omega & \omega_H + (N_y - N_z)\omega_M - i\alpha\omega \\ \omega_H + (N_x - N_z)\omega_M - i\alpha\omega & \end{pmatrix} \begin{pmatrix} m_x \\ m_y \end{pmatrix}$$

[4] In the FMR experiments conducted in this thesis the applied static magnetic field is in the 100mT

Through matrix inversion a more useful form of the stated set of equations is obtained in the form of the dynamic susceptibility tensor $\hat{\boldsymbol{\chi}}$ which describes the amplitude and phase of the induced magnetic precession for a given applied RF field; $\mathbf{m} = \hat{\boldsymbol{\chi}}\mathbf{h_{rf}}$:

$$\hat{\boldsymbol{\chi}} = \begin{pmatrix} \chi_{xx} & i\chi_{xy} & 0 \\ -i\chi_{yx} & \chi_{yy} & 0 \\ 0 & 0 & 0 \end{pmatrix} \tag{2.33}$$

As the obtained susceptibility indicates, the induced precession in magnetization is at right angles to the magnetization direction when only considering weak magnetic pumping fields. The individual components of (2.33) are given by [11]

$$\chi_{xx} = \frac{\omega_M(\omega_H + (N_x - N_y)\omega_M - i\alpha\omega)}{\omega_r^2 - (1+\alpha^2)\omega^2 - i\alpha\omega(2\omega_H + (N_x + N_z - 2N_y)\omega_M)} \tag{2.34}$$

$$\chi_{yy} = \frac{\omega_M(\omega_H + (N_z - N_y)\omega_M - i\alpha\omega)}{\omega_r^2 - (1+\alpha^2)\omega^2 - i\alpha\omega(2\omega_H + (N_x + N_z - 2N_y)\omega_M)} \tag{2.35}$$

$$\chi_{xy/yx} = \frac{\omega\omega_M}{\omega_r^2 - (1+\alpha^2)\omega^2 - i\alpha\omega(2\omega_H + (N_x + N_z - 2N_y)\omega_M)} \tag{2.36}$$

Where ω_r is the resonance frequency first derived by Kittel [18] [19]:

$$\omega_r = \sqrt{(\omega_H + (N_x - N_y)\omega_M)(\omega_H + (N_z - N_y)\omega_M)} \tag{2.37}$$

For a ferromagnetic thin film oriented as in Figure 2.5 the demagnetization tensor assumes the values $N_{y/z} = 0$, $N_x = 1$, as noted in section 2.3.2. When also assuming a weak magnetic damping ($\alpha^2 \ll 1$), which is the case for Permalloy thin films[5] [20], the dynamic susceptibility terms reduce to

$$\chi_{xx} = \frac{\omega_M(\omega_B - i\alpha\omega)}{(\omega_r^2 - \omega^2) - i\alpha\omega(\omega_H + \omega_B)} \tag{2.38}$$

$$\chi_{yy} = \frac{\omega_M(\omega_H - i\alpha\omega)}{(\omega_r^2 - \omega^2) - i\alpha\omega(\omega_H + \omega_B)} \tag{2.39}$$

$$\chi_{xy/yx} = \frac{\omega\omega_M}{(\omega_r^2 - \omega^2) - i\alpha\omega(\omega_H + \omega_B)} \tag{2.40}$$

$$\omega_r = \sqrt{\omega_H(\omega_H + \omega_M)} = \sqrt{\omega_H\omega_B} \tag{2.41}$$

[5] Gilbert damping parameters of the 0.006 have been reported for Permalloy in the literature. For Permalloy films fabricated in this project the Gilbert damping parameter was approximated to 0.007, thus justifying the stated assumption

Table 2.1: Real and imaginary susceptibility terms for a thin film with a plane normal oriented along the x-axis of a Cartesian coordinate system when assuming weak magnetic damping

χ_{ij}	χ'_{ij}	χ''_{ij}
χ_{xx}	$\frac{\omega_M\omega_B(\omega_r^2-\omega^2)}{(\omega_r^2-\omega^2)^2+\alpha^2\omega^2(\omega_H+\omega_B)^2}$	$\frac{\alpha\omega\omega_M(\omega_B^2+\omega^2)}{(\omega_r^2-\omega^2)^2+\alpha^2\omega^2(\omega_H+\omega_B)^2}$
χ_{yy}	$\frac{\omega_M\omega_H(\omega_r^2-\omega^2)}{(\omega_r^2-\omega^2)^2+\alpha^2\omega^2(\omega_H+\omega_B)^2}$	$\frac{\alpha\omega\omega_M(\omega_H^2+\omega^2)}{(\omega_r^2-\omega^2)^2+\alpha^2\omega^2(\omega_H+\omega_B)^2}$
$\chi_{xy/yx}$	$\frac{\omega_M\omega(\omega_r^2-\omega^2)}{(\omega_r^2-\omega^2)^2+\alpha^2\omega^2(\omega_H+\omega_B)^2}$	$\frac{\alpha\omega_M\omega^2(\omega_B+\omega_H)}{(\omega_r^2-\omega^2)^2+\alpha^2\omega^2(\omega_H+\omega_B)^2}$

where the abbreviation $\omega_B = \omega_H + \omega_M$ has been used. The obtained dynamic susceptibilities are as shown complex quantities and may thus be separated in terms of their real and imaginary components $\chi = \chi' + i\chi''$, as presented in table 2.1. The real component of the susceptibility is related to dispersion or energy storage in the system, whereas the imaginary component relates to energy dissipation and loss due to Gilbert damping. Figure 2.6 plots the real and imaginary component of χ_{xx}. As illustrated the real, dispersive, component shows an asymmetric dependence in the applied field strength, whereas the dissipative, imaginary, term is described by a symmetric Lorentzian lineshape.

In FMR experiments the magnetic state of a material is probed by measuring the power loss in the RF field when subjecting the sample to a similar field configuration as described in this section. The measured power loss will for the chosen geometry be(see section 3.2)

$$P = \frac{1}{2}\omega\mu_0 h_{rf}^2 \chi''_{xx} \tag{2.42}$$

In these experiments the shape of the susceptibility is probed by varying either the RF field frequency or the static field magnitude while keeping the other constant. As FMR experiments conducted in this report were performed by varying the magnitude of the magnetic field, susceptibilities expressed in terms of the applied field strength are more convenient when analyzing extracted FMR absorption curves. While this may be achieved by direct substitution of equations (2.31) and (2.32) into the expressions of Table 2.1, the resulting susceptibilities become rather complex due to the resonance field being nonlinear in H_0 and M_S. For curve fitting purposes it is therefore more convenient to apply approximate equations in place of exact susceptibility terms. By assuming the saturation magnetization to be much greater than the applied field strength, $\omega_M \gg \omega_H$, the following simplifications

may be made;

$$\omega_B = \omega_M + \omega_H \approx \mu_0|\gamma|M_S \tag{2.43}$$

$$\begin{aligned}\omega_r^2 - \omega^2 &= \mu_0^2|\gamma|^2[H_0(H_0 + M_S) - H_r(H_r + M_S)] \\ &\approx \mu_0^2|\gamma|^2 M_S(H_0 - H_r)\end{aligned} \tag{2.44}$$

Furthermore, it is assumed that the linewidth of the absorption curve is small compared to the resonance frequency, that one need not stray far from resonance in order to observe the shape of the curve, such that

$$\omega_r^2 + \omega^2 \approx 2\mu_0^2|\gamma|^2 M_S H_0 \tag{2.45}$$

By applying the listed approximations to the equations of Table 2.1 the real and imaginary susceptibilities components reduce to

$$\chi'_{xx/xy} = \eta_{xx/xy} M_S \Delta H \frac{(H_0 - H_r)/\Delta H}{(H_0 - H_r)^2 + (\Delta H/2)^2} \tag{2.46}$$

$$\chi''_{xx/xy} = \frac{1}{2}\eta_{xx/xy} M_S \Delta H \frac{1}{(H_0 - H_r)^2 + (\Delta H/2)^2} \tag{2.47}$$

where $\Delta H = 2\alpha\omega/\mu_0|\gamma|$ has been introduced as a measure of the absorption curve linewidth. As this parameter is proportional in α it is generally used as a measure of the magnetic relaxation rate in a system. $\eta_{xx/xy} = 0.917/3.35$ is here introduced to compensate for differences in estimated and exact susceptibility amplitudes[6]. By approximating the susceptibilities using equations (2.46) and (2.47) was estimated to introduce a maximum error of 0.1% when assuming a resonance field frequency and saturation magnetization on the same order as those measured for the studied Permalloy samples.

[6]The magnitude of $\eta_{xx/xy}$ depends on the validity of the stated assumptions. In the studied Permalloy thin films resonance was achieved at a field strength of approximately $\mu_0 H_0 \approx 0.1$T, whereas the saturation magnetization was estimated to approximately $\mu_0 M_S \approx 1$T. The assumption of the saturation magnetization being much greater than the resonance field is therefore only partially valid, thus yielding $\eta_{xx/xy}$ values different from unity

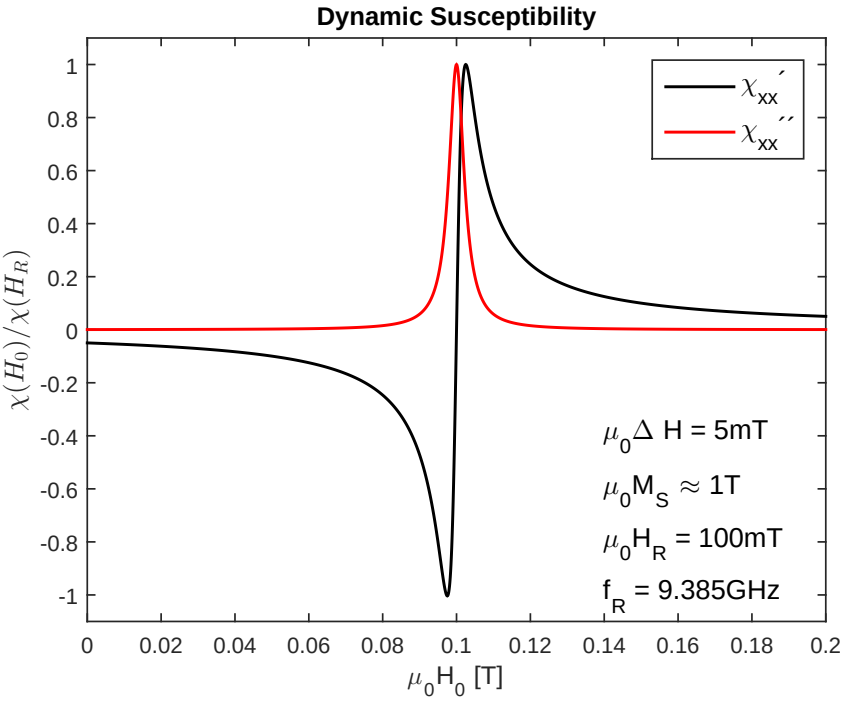

Figure 2.6: Field dependence of the real and imaginary components of the dynamic susceptibility

2.5 Electromagnetic Induction and Eddy Currents

The following sections provides a brief review of electromagnetic induction, the induction of eddy currents in conductors and the magnetic fields arising from these currents.

2.5.1 Electromagnetic Induction

Electromagnetic induction follows directly from the Maxwell-Faraday equation

$$\nabla \times \mathbf{E}(\mathbf{r}, \mathbf{t}) = -\frac{\partial \mathbf{B}(\mathbf{r}, \mathbf{t})}{\partial t} \tag{2.48}$$

which states that a time varying magnetic field is always accompanied by a circulating electric field, and vice versa. When a conductive loop defined by the curve C is exposed to a time varying magnetic flux density $\mathbf{B}(\mathbf{t})$ equation (2.48) describe the induced current flow in the loop;

$$\int_S \nabla \times \mathbf{E} \cdot d\mathbf{S} = \oint_C \mathbf{E} \cdot d\mathbf{l} = \epsilon = -\frac{\partial}{\partial t} \int_S \mathbf{B} \cdot d\mathbf{S} = -\frac{\partial \Phi}{\partial t} \tag{2.49}$$

S being an arbitrary surface bounded by C, ϵ the electromotive force induced in the current loop and Φ the magnetic flux passing through S. The Maxwell-Faraday equation thus describes the induction of a current in a conductor ($I = \epsilon/R$ from Ohm's law) when exposing it to a time varying magnetic flux. This current will in turn give rise to a secondary inhomogeneous magnetic flux density as discussed in the following.

2.5.2 Magnetic Flux Density From a Circular Current Loop

For a circular loop carrying a current I the induced magnetic field at any point in space may be obtained by finding the magnetic vector potential [16]

$$\mathbf{A} = \frac{\mu_0 I}{4\pi} \oint \frac{d\mathbf{l}}{s} \tag{2.50}$$

s here being the distance from a point in space, P, to the line element $d\mathbf{l}$, as figure 2.7 illustrates. As the derivation required to obtain the general solution of (2.50) for the stated constraints is rather extensive the interested reader is directed to the literature for a complete treatment [16]. The solution to equation (2.50) yields the vector potential

$$\mathbf{A} = A_\phi \hat{\boldsymbol{\phi}} = \frac{\mu_0 I}{2\pi} [2k^{-1} r^{-/2} (K(k) - E(k)) - k r^{-1/2} K(k)] \hat{\boldsymbol{\phi}} \tag{2.51}$$

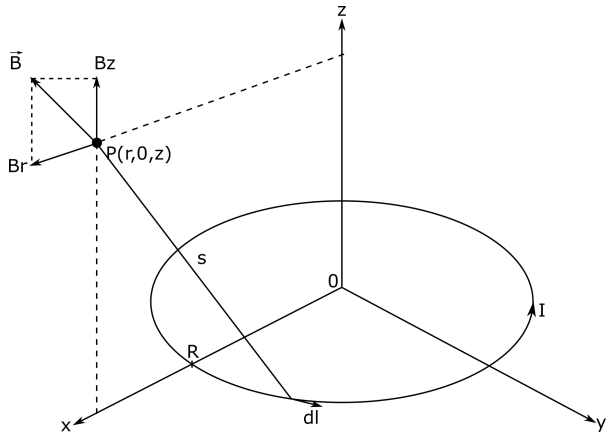

Figure 2.7: Illustration of magnetic field components arising from the a current carrying loop.

from which the magnetic flux density may be calculated ($\mathbf{B} = \nabla \times \mathbf{A}$):

$$B_z(r,z) = \frac{\mu_0 I}{2\pi\sqrt{z^2+(R+r)^2}}\left(\frac{R^2-z^2-r^2}{z^2+(r-R)^2}E(k)+K(k)\right) \tag{2.52}$$

$$B_r(r,z) = \frac{\mu_0 I z}{2\pi r\sqrt{z^2+(R+r)^2}}\left(\frac{R^2+z^2+r^2}{z^2+(r-R)^2}E(k)-K(k)\right) \tag{2.53}$$

Here K and E respectively represent complete elliptical integrals of the first and second kind while

$$k = \sqrt{\frac{4rR}{z^2+(R+r)^2}} \tag{2.54}$$

As indicated by (2.52) and (2.53) a current carrying circular loop will give rise to an inhomogeneous magnetic field of axial symmetry. This field will in turn affect the magnetic flux acting on the loop

$$\Phi' = -\frac{\partial I(t)}{\partial t}\int_S B_z(r,0)dS \tag{2.55}$$

thus affecting the electromotive force driving the current.

2.5.3 Self Inductance and Phase Shifts

Consider now a time harmonic magnetic flux density $\mathbf{B}e^{i\omega t}$ applied to a conductive loop. When first only considering this contribution to the magnetic flux, the resulting current in the loop follows from equation (2.49):

$$I = -i\int_S \mathbf{B}e^{i\omega t}\cdot d\mathbf{S}/R = \int_S \mathbf{B}e^{i\omega t}\cdot d\mathbf{S}e^{-i\pi/2}/R \tag{2.56}$$

As indicated the induced current will be phase shifted relative to the applied pumping field by $\phi = -\pi/2$. This current will in turn give rise to a secondary inhomogeneous phase shifted magnetic field which will also act on the current loop. The resulting secondary electromotive force will in turn induce a secondary current component which gives rise to yet another field contribution to the magnetic flux. This recursive effect is referred to as self inductance and is characterized by the self inductance constant $L = \Phi/I$ which is determined by the geometry of the conductor. For a conductive thin film loop the phase of induced currents and associated inhomogeneous magnetic fields will be related to the inductance through [10]

$$\phi = -\left[90 + arctan(\frac{\omega L}{R}) + d/\delta\right] \tag{2.57}$$

ω being the angular frequency of the applied magnetic flux density, L the inductance of the loop, R its resistance, d its thickness and δ the microwave skin depth ($\delta \sim$ 800nmfor Au at 10GHz [10]). For the thin film Au loops fabricated in this project the thin film thickness was 10nm, this allowing one to neglect the third term of 2.57. As such the phase of induced magnetic fields is expected to lie in the $\phi \subset [-\pi, -\pi/2]$ range.

2.5.4 Eddy Current Induction in a NM Thin Film Plane

When a time varying magnetic flux density is applied perpendicular to a conductive thin film the Maxwell-Faraday equation predicts the excitation of circulating currents in the thin film plane due the associated circulating electric field. These currents, commonly referred to as eddy currents, will give rise to secondary phase shifted inhomogeneous magnetic fields in close proximity the conductor. While a numerical approach is generally needed to calculate the distribution of induced currents and associated magnetic fields a closed form solution for the induced current density is obtainable for a circular metallic thin film plate of a thickness much less than the electromagnetic skin depth. This section will discuss results obtained from this solution as it gives some insight into the expected distribution of eddy current induced magnetic fields.

For a thin non-magnetic circular metallic plate subject to a spatially homogeneous time harmonic magnetic flux density $\mathbf{B}e^{i\omega t}$ directed along the thin film normal, the induced current density in the thin film plane has been found to obey [21]

$$J_\theta(r) = -\frac{k|\mathbf{B}|}{\mu_0}\frac{I_1(kr)}{I_0(ka)} \tag{2.58}$$

where

$$k = \sqrt{\omega\mu_0\sigma}e^{i\pi/4} \tag{2.59}$$

a being the radius of the plate, μ_0 the permeability of vacuum, σ the plate conductivity and $I_n(\alpha)$ the modified Bessel function of the first kind and order n. Figure 2.8 plots the calculated absolute value and phase of equation (2.58) along the edge

of a circular Au plate (note the cropped x-axis). As shown the current density is expected to be localized primarily along the the sample edge. Furthermore, the radial phase distribution of induced currents is shown to rapidly fluctuate with the radius, it being close to $\phi = -\pi$ along the edge where the current distribution is largest. The magnetic field distribution arising from eddy current excitations in the circular Au thin films considered in this report can thus to first order be visualized as in Figure 3.1, where the induced field is assumed to originate from a circular current loop localized along the sample edge.

While equation (2.58) does provide some insight into the expected current distribution for an isolated non-magnetic thin film plate it does not necessarily provide an accurate description of the induced distribution in FM/NM bilayer structures. In these structures the excitation of eddy currents or FMR modes in the FM layer may result in the NM no longer experiencing a homogeneous pumping field, thus invalidating assumptions made in the derivation of equation (2.58). FMR dissipation of the magnetic fields induced by eddy currents in the NM will also affect the magnetic flux acting on the NM, thus perturbing the resulting current distribution. To accurately determine the induced current density a simultaneous numerical solution of the Maxwell boundary problem and the LLG equation is necessary. As this was well beyond the scope of this study, equation (2.58) will be assumed to provide a sufficiently accurate description.

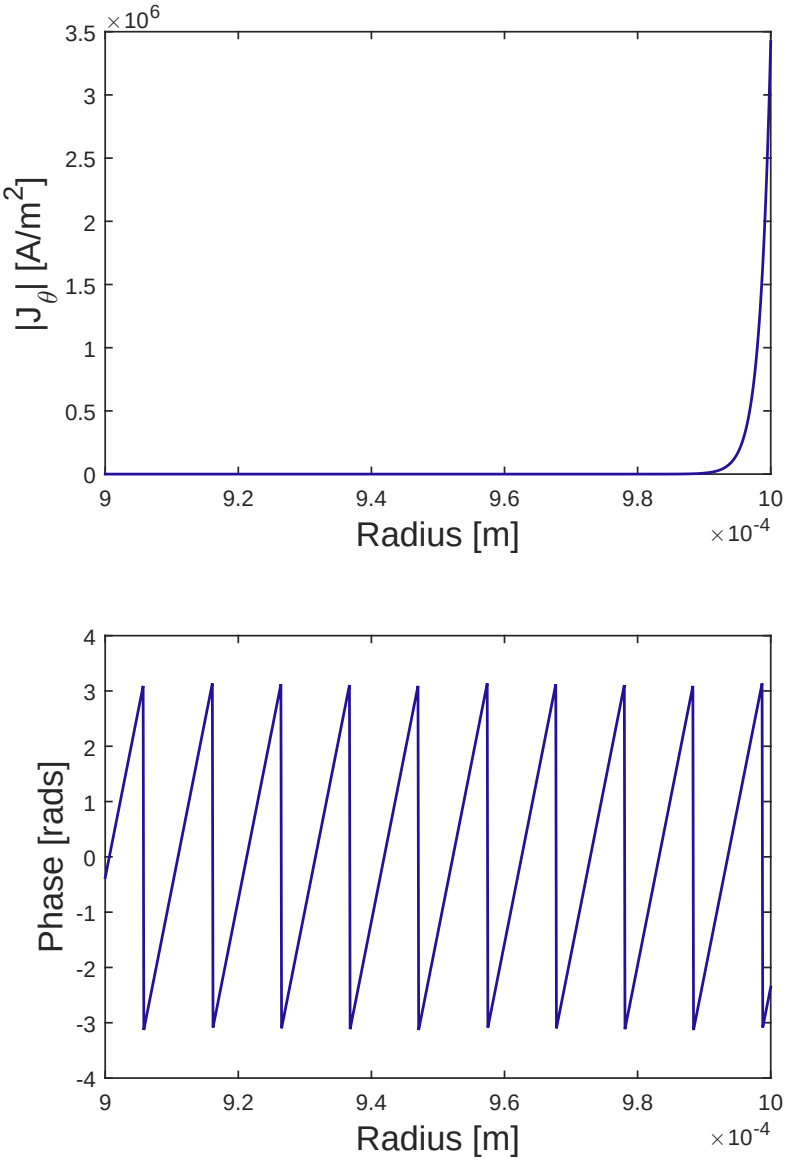

Figure 2.8: Calculated absolute radial current density and phase distribution along the edge of a circular Au plate. Only a portion of the radial distribution has been included to highlight current variations along the sample edge. The following parameters were assumed: $a = 10^{-3}$m, $\sigma = 10^{7}\Omega^{-1}\,\mathrm{m}^{-1}$, $\omega = 2\pi \cdot 9.38$GHz

Chapter 3

Eddy Current Field Perturbations in FMR Lineshapes

To describe the asymmetric lineshapes obtained in the FMR analysis of FM/NM thin film structures a theoretical model was established by considering the relevant electromagnetic loss terms present in the FMR microwave cavity. The following section presents this model along with the assumptions made in its derivation. As shown the obtained model corresponds to a functionally similar expression as the one used in Flovik et.al.s [10] initial study of FMR lineshape perturbations in FM/NM thin film structures. The presently applied model does, however, more directly link experimentally extracted parameters to physical entities, thereby potentially simplifying the analysis of obtained FMR data.

The following sections will first give a brief account of the experimental setup and the magnetic fields encountered in these experiments. Next the various loss terms present in the system are discussed before deriving the model used to analyze the data obtained in this thesis.

3.1 Experimental Setup

To study the effects of eddy currents on ferromagnetic resonance in FM/NM structures a cavity based FMR spectroscopy setup was employed. As will be discussed in section 4.4.2 this setup probes the magnetic state of a sample by measuring the induced dissipation of microwave energy when applying a variable static magnetic field in conjunction with an orthogonal RF magnetic field. The RF component of the magnetic field was applied by lowering the sample into a microwave resonator cavity coupled to a radiation source and the static field generated by a variable electromagnet. Figure 3.1 illustrates the orientation of applied fields with respect

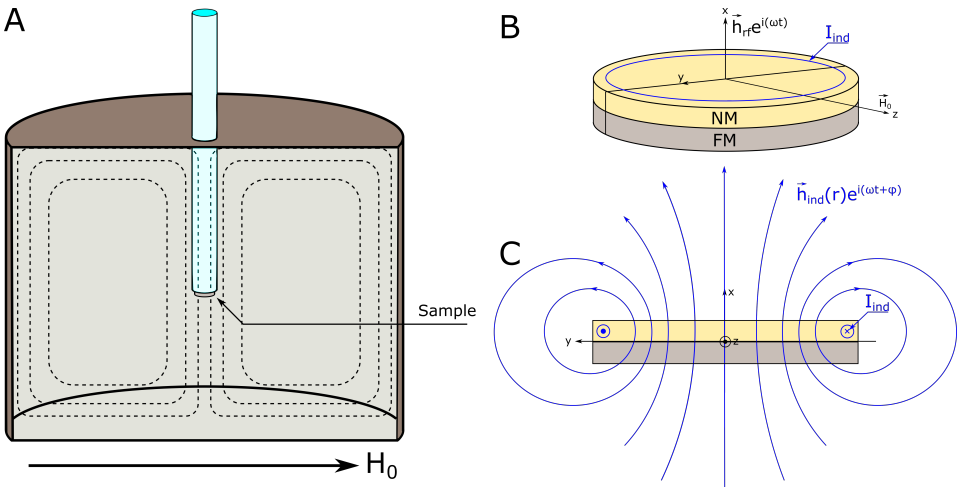

Figure 3.1: A) Illustration of the used cavity based FMR setup. Dashed curves illustrate field lines for the applied magnetic RF field. B) illustrates the field orientation with respect to the sample geometry. The currents induced in the NM layer of the structure gives rise to a spatially inhomogeneous field, phase shifted relative to the applied RF field, as sketched in C).

to the sample geometry. As shown the RF field component $\mathbf{h_{rf}}$, here assumed to be spatially homogeneous, is applied along the sample plane normal whereas the static component $\mathbf{H_0}$ is directed in the plane of the specimen. In this field configuration the RF component will generate a magnetic flux through the NM layer of thin film structures, thus facilitating the excitation of eddy currents. These currents will in turn give rise to secondary inhomogeneous field components, $\mathbf{h_{ind}}(\mathbf{r})$, phase shifted relative to the applied RF field. By defining the x-axis of a Cartesian coordinate system to lie along the thin film normal and the z-axis in the static field direction as Figure 3.1 B illustrates, relevant field quantities may be represented by

$$\mathbf{H}(\mathbf{r},t) = H_0\hat{\mathbf{z}} + \mathbf{h_{tot}}(\mathbf{r}) \cdot e^{i\omega t} \tag{3.1}$$

$$\mathbf{M}(\mathbf{r},t) = M_0\hat{\mathbf{z}} + \mathbf{m}(\mathbf{r}) \cdot e^{i\omega t} \tag{3.2}$$

where $\mathbf{h_{tot}}(\mathbf{r})$ is the sum of the applied RF field and the inhomogeneous phase shifted eddy current field, $M_0 \approx M_S$ the magnetization induced by $\mathbf{H_0}$ and $\mathbf{m}(\mathbf{r})$ the magnetic perturbation due to $\mathbf{h_{tot}}$. The following sections will discuss how the presence of a non-magnetic metal layer and associated eddy current fields affect the shape and magnitude of recorded FMR absorption curves.

3.2 Electromagnetic Loss and FMR

In the used FMR setup the detector signal is a linear function of the first derivative in power dissipation with respect to applied field strength (see section 4.4.2);

$$\text{Signal} = \kappa \frac{\partial P}{\partial H_0} \tag{3.3}$$

P here being the time averaged power dissipation within the microwave cavity and κ a proportionality constant. As such, a discussion regarding relevant sources of energy loss is in order.

For an electromagnetic wave the average power dissipation within a volume V is described by the time averaged Poynting vector, which as shown in appendix A can be written on the form

$$P = -\oint_s \langle \mathbf{S} \rangle \cdot d\mathbf{s} = \int_V \underbrace{\frac{1}{2}\Re\{\mathbf{H}^* \cdot \frac{\partial \mathbf{B}}{\partial t}\}}_{\bar{\rho}_M} + \underbrace{\frac{1}{2}\Re\{\mathbf{E} \cdot \frac{\partial \mathbf{D}^*}{\partial t}\}}_{\bar{\rho}_D} + \underbrace{\frac{1}{2}\Re\{\mathbf{E} \cdot \mathbf{J}^*\}}_{\bar{\rho}_J} dV \tag{3.4}$$

The terms on the right hand side of equation 3.4, denoted by $\bar{\rho}_M$, $\bar{\rho}_D$ and $\bar{\rho}_J$, represent the time averaged power per volume dissipated through magnetic, dielectric and joule loss respectively. The respective contributions to the FMR detector signal will be considered in the following

3.2.1 Dielectric Loss

As all electric field quantities within the cavity show a harmonic time dependence the dielectric signal contribution is by substitution

$$\frac{\kappa}{2}\frac{\partial}{\partial H_0}\int_V \Re\{i\omega\epsilon|\mathbf{E}|^2\}dV = -\frac{\kappa\omega}{2}\frac{\partial}{\partial H_0}\int_V \Im(\epsilon)|\mathbf{E}|^2 dV \tag{3.5}$$

Even though some power dissipation may result from dielectric loss in the silicon support and quartz rod, this contribution to the detector signal can be neglected as it is assumed that the imaginary electric permittivity is independent of the magnetic strength.

3.2.2 Joule Loss

The signal contribution associated with electric heating is expressed by

$$\frac{\kappa}{2\sigma_{Py}}\int_{V_{FM}} \frac{\partial|\mathbf{J}|^2}{\partial H_0}dV + \frac{\kappa}{2\sigma_{Au}}\int_{V_{NM}} \frac{\partial|\mathbf{J}|^2}{\partial H_0}dV \tag{3.6}$$

where V_{FM} and V_{NM} constitute the volumes occupied by the FM and NM layers respectively, whereas σ_{Py} and σ_{Au} are the conductivities of Permalloy and Gold. As strong currents are expected to result in the NM layer by virtue of electromagnetic

induction significant joule loss will likely ensue. The induced current density is, however, expected to be independent of the static magnetic field as it does not directly influenced magnetic induction. The signal contribution from joule loss is therefore expected to be negligible to first order. Before proceeding it should be noted that the static magnetic field dependence in FMR could induce a second order dependence in joule loss as this resonance phenomena will perturb the RF magnetic field distribution in the vicinity of the ferromagnet. These second order effects are, however, well beyond the scope of the first order analytical model derived in this chapter.

3.2.3 Magnetic Loss

This leaves only contributions attributed to magnetic damping, the corresponding signal contribution being

$$\kappa\frac{\partial P_M}{\partial H_0} = \frac{\kappa}{2}\int_{V_{FM}} \Re\{\mathbf{H}^* \cdot \frac{\partial \mathbf{B}}{\partial t}\}dV \tag{3.7}$$

By substituting equations (3.1) and (3.2) into (3.7) the signal contribution from magnetic loss becomes:

$$\kappa\frac{\partial P_M}{\partial H_0} = \frac{\omega\mu_0\kappa}{2}\frac{\partial}{\partial H_0}\int_{V_{FM}} \Re\{i\mathbf{H}^*(\mathbf{r},t)\cdot[\mathbf{h_{tot}}(\mathbf{r},t)+\mathbf{m}(\mathbf{r},t)]\}dV \tag{3.8}$$

$$= \frac{\omega\mu_0\kappa}{2}\frac{\partial}{\partial H_0}\int_{V_{FM}} \Re\{i[H_0\hat{\mathbf{z}}\cdot\mathbf{h_{tot}}(\mathbf{r},t)+|\mathbf{h_{tot}}|^2 + H_0\hat{\mathbf{z}}\cdot\mathbf{m}(\mathbf{r},t)+\mathbf{h}^*_{\mathbf{tot}}(\mathbf{r},t)\cdot\mathbf{m}(\mathbf{r},t)]\}dV \tag{3.9}$$

The first term in the integrand of equation (3.9) is expected not to contribute to the detector signal as it will show an explicit time dependence, it being the vector product of only one time dependent variable. This term should therefore average to zero during detector sampling. The second term will also yield a contribution of zero as it is strictly real. The third term is as shown proportional to the magnetic perturbation in the static field direction. As shown in section 2.4.3 this component can be neglected when only considering weak harmonic components in the magnetic field as the corresponding precession in magnetization will be at right angles to the static field. In considered FMR experiments the static field strength is approximately 100mT at resonance while the harmonic component has an estimated amplitude of approximately 5µT in the sample position (see section 4.4.3). As the strength of induced magnetic field components are assumed to be in the same field range as the applied RF field this approximation should remain valid, thereby allowing one to neglect the contribution from this term. This leaves only the final term in equation (3.9) which may be written on the form

$$\kappa\frac{\partial P_M}{\partial H_0} = \frac{\omega\mu_0\kappa}{2}\frac{\partial}{\partial H_0}\int_{V_{FM}} \Re\{i\mathbf{h}^*_{\mathbf{rf}}(\mathbf{r})\cdot\mathbf{m}(\mathbf{r})+\Re\{i\mathbf{h}^*_{\mathbf{ind}}(\mathbf{r})\cdot\mathbf{m}(\mathbf{r})\}dV \tag{3.10}$$

The first term is here interpreted as the power dissipation in the applied RF field and the second term as the dissipation of fields attributed to eddy currents. As only loss in the electromagnetic radiation incident on the cavity is recorded in the used spectroscopy setup the first term in equation (3.10) constitutes the sole contributor to the detector signal when only considering dominant sources of loss:

$$\text{Signal} = \frac{\omega\mu_0\kappa}{2}\frac{\partial}{\partial H_0}\int_{V_{FM}} \Re\{i\mathbf{h}^*_{\mathbf{rf}}(\mathbf{r})\cdot\mathbf{m}(\mathbf{r})\}dV \tag{3.11}$$

3.3 Eddy Current Effects in FMR Lineshapes

In order to extend the discussion of eddy current interactions in FMR beyond equation (3.11) certain approximations need be made regarding $\mathbf{m}(\mathbf{r})$ and its relation to $\mathbf{h_{tot}}(\mathbf{r})$. In section 2.4.3 it was found that the induced magnetic precession could be described by the dynamic susceptibility tensor

$$\mathbf{m} = \hat{\boldsymbol{\chi}}\mathbf{h_{rf}} \tag{3.12}$$

when assuming all field quantities to be homogeneous. In the considered problem this is not the case due to inhomogeneous eddy current field components. The dynamic susceptibility tensor will, however, be applied to first order as an exact treatment requires the simultaneous numerical solution of the LLG equation and Maxwell boundary conditions, a problem well beyond the scope of this thesis. The following section presents the obtained analytical expression estimating the FMR detector response for FM/NM thin film structures when treating precession as done in the homogeneous case.

When defining the coordinate system as in Figure 3.1 time varying magnetic field components are given by

$$\mathbf{h_{rf}} = \begin{pmatrix} h_{rf} \\ 0 \\ 0 \end{pmatrix} \tag{3.13}$$

$$\mathbf{h_{ind}}(\mathbf{r}) = \begin{pmatrix} h^x_{ind}(\mathbf{r})\cdot e^{i\phi_x(\mathbf{r})} \\ h^y_{ind}(\mathbf{r})\cdot e^{i\phi_y(\mathbf{r})} \\ h^z_{ind}(\mathbf{r})\cdot e^{i\phi_z(\mathbf{r})} \end{pmatrix} \tag{3.14}$$

ϕ_i here being the phase shifts of eddy current field components relative to the applied pumping field. Phase shifts are here allowed to vary with respect to position and field direction. Now assuming that the magnetization is approximately

represented by equation (3.12) one may write:

$$\begin{aligned}
\mathbf{h_{rf}^*} \cdot \mathbf{m}(\mathbf{r}) &\approx \mathbf{h_{rf}^*} \cdot \hat{\boldsymbol{\chi}} \mathbf{h_{tot}}(\mathbf{r}) \\
&= \mathbf{h_{rf}} \cdot \hat{\boldsymbol{\chi}} (\mathbf{h_{rf}} + \mathbf{h_{ind}}(\mathbf{r})) \\
&= \begin{pmatrix} h_{rf} & 0 & 0 \end{pmatrix} \begin{pmatrix} \chi_{xx} & i\chi_{xy} & 0 \\ -i\chi_{yx} & \chi_{yy} & 0 \\ 0 & 0 & 0 \end{pmatrix} \begin{pmatrix} h_{rf} + h_{ind}^x(\mathbf{r}) \cdot e^{i\phi_x(\mathbf{r})} \\ h_{ind}^y(\mathbf{r}) \cdot e^{i\phi_y(\mathbf{r})} \\ h_{ind}^z(\mathbf{r}) \cdot e^{i\phi_z(\mathbf{r})} \end{pmatrix} \\
&= \chi_{xx} h_{rf}^2 + h_{rf}[\chi_{xx} h_{ind}^x(\mathbf{r}) \cdot e^{i\phi_x(\mathbf{r})} + i\chi_{xy} h_{ind}^y(\mathbf{r}) \cdot e^{i\phi_y(\mathbf{r})}]
\end{aligned}$$

To separate the stated expression in terms of its real and imaginary components Euler's formula may be applied ($e^{i\theta} = cos\theta + isin\theta$):

$$\begin{aligned}
\mathbf{h_{rf}^*} \cdot \mathbf{m}(\mathbf{r}) = h_{rf}[\chi_{xx} h_{rf} + \chi_{xx} h_{ind}^x(\mathbf{r}) cos(\phi_x(\mathbf{r})) - \chi_{xy} h_{ind}^y sin(\phi_y(\mathbf{r}))] \\
+ ih_{rf}[\chi_{xx} h_{ind}^x(\mathbf{r}) sin(\phi_x(\mathbf{r})) + \chi_{xy} h_{ind}^y(\mathbf{r}) cos(\phi_y(\mathbf{r}))] \quad (3.15)
\end{aligned}$$

Now using $\chi = \chi' + i\chi''$ in conjunction with equation (3.15) the integrand of equation (3.11) becomes

$$\begin{aligned}
\Re\{i\mathbf{h_{rf}^*} \cdot \mathbf{m}(\mathbf{r})\} = -h_{rf}[\chi''_{xx}[h_{rf} + h_{ind}^x(\mathbf{r}) cos(\phi_x(\mathbf{r}))] + \chi'_{xx} h_{ind}^x sin(\phi_x(\mathbf{r}))] \\
+ h_{rf} h_{ind}^y(\mathbf{r})[\chi''_{xy} sin(\phi_y(\mathbf{r})) - \chi'_{xy} cos(\phi_y(\mathbf{r}))] \quad (3.16)
\end{aligned}$$

which when substituted into equation (3.11) yields the following expression for the detector response

$$\begin{aligned}
\text{Signal} = -\frac{\omega\mu_0\kappa}{2} h_{rf} \int_{V_{FM}} \Bigg[\left[h_{rf} + h_{ind}^x(\mathbf{r}) cos(\phi_x(\mathbf{r}))\right] \frac{\partial \chi''_{xx}}{\partial H_0} + h_{ind}^x sin(\phi_x(\mathbf{r})) \frac{\partial \chi'_{xx}}{\partial H_0} \\
- h_{ind}^y sin(\phi_y(\mathbf{r})) \frac{\partial \chi''_{xy}}{\partial H_0} + h_{ind}^y cos(\phi_y(\mathbf{r})) \frac{\partial \chi'_{xy}}{\partial H_0} \Bigg] dV \quad (3.17)
\end{aligned}$$

As shown the presence of eddy current field components results in a mixing of dispersive and dissipative susceptibility terms in the recorded signal. If now the susceptibilities of equations (2.46) and (2.47) are substituted into equation (3.17)

the following expression for the detector response results;

$$\text{Signal} = \frac{\partial}{\partial H_0}\left[A\frac{1}{(H_R-H_0)^2+(\Delta H/2)^2} + B\frac{(H_R-H_0)/\Delta H}{(H_R-H_0)^2+(\Delta H/2)^2}\right] \tag{3.18}$$

$$= A\frac{2(H_R-H_0)}{[(H_R-H_0)^2+(\Delta H/2)^2]^2}$$

$$+ B\left[\frac{-1/\Delta H}{(H_R-H_0)^2+(\Delta H/2)^2} - \frac{2(H_R-H_0)^2/\Delta H}{[(H_R-H_0)^2+(\Delta H/2)^2]^2}\right] \tag{3.19}$$

where

$$A = \frac{1}{2}\omega\mu_0|\kappa|M_S\Delta H h_{rf}\Big[\eta_{xx}\big[h_{rf}V_{FM} + \int_{V_{FM}} h^x_{ind}(\mathbf{r})cos(\phi_x(\mathbf{r}))dV\big]$$

$$- \eta_{xy}\int_{V_{FM}} h^y_{ind}sin(\phi_y(\mathbf{r}))dV\Big] \tag{3.20}$$

$$B = \frac{1}{4}\omega\mu_0|\kappa|M_S\Delta H h_{rf}\Big[\int_{V_{FM}} \eta_{xx}h^x_{ind}(\mathbf{r})sin(\phi_x(\mathbf{r}))dV$$

$$+ \eta_{xy}\int_{V_{FM}} h^y_{ind}(\mathbf{r})cos(\phi_y(\mathbf{r}))dV\Big] \tag{3.21}$$

$$\tag{3.22}$$

As equation (3.19) indicates the obtained detector signal can be seen as the sum of two lineshape components of amplitude A and B. The respective lineshapes are illustrated in Figure 3.2, where the term of amplitude A corresponds to the symmetric absorption curve obtained in the absence of eddy current interactions and the second term to an asymmetric curve attributed to eddy current fields interacting with the ferromagnet. The mixing of dissipative and dispersive terms due to eddy current interactions in the sample thus introduces an asymmetry in recorded absorption curves. By parameterizing the asymmetry of an absorption curve, one may thus gain insight into the phase and magnitude of inductive fields interacting with the sample.

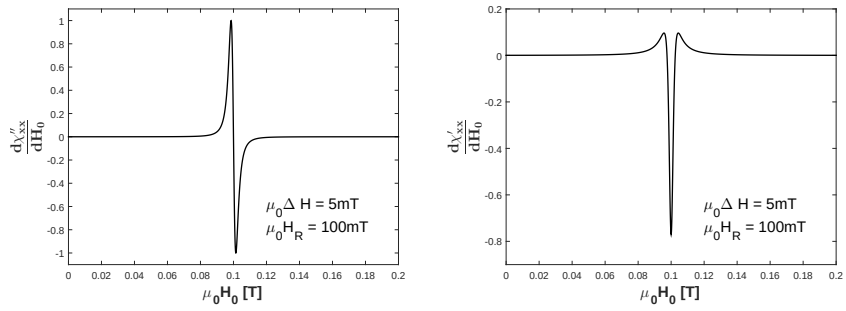

(a) (b)

Figure 3.2: (a) illustrates the normalized lineshape associated with the complex susceptibility term, whereas (b) corresponds to the lineshape associated with the real component. Both lineshapes were scaled by the same coefficient.

Chapter 4

Experimental Materials, Methods and Procedures

The following section serves to introduce the primary experimental techniques and procedures used to fabricate and characterize the thin film structures studied in this thesis. These structures correspond to thin film stacks of Permalloy covered by a normal metal layer (gold) with a thickness in the nanometer regime and lithographically defined lateral dimensions in the micron to millimeter range. An introduction to the primary fabrication techniques and procedures employed in this study is first presented before describing how the produced samples were characterized. The final section describes how the obtained experimental data was analyzed.

4.1 Overview

The Permalloy / gold thin film structures studied in this master thesis were prepared using a lift off process combining optical lithography, DC magnetron sputter deposition and electron beam evaporation. An overview of the primary fabrication steps is shown in figure 4.1: A thin layer of AZ5214E image reversal resist is first applied to a clean silicon support. To enhance the resolution of the lithographic pattern transfer, edge beads corresponding to resist thickness variations along the sample edge are removed before transferring the pattern from a photomask to the resist layer. Before loading the resist covered substrates into the PVD chamber a hard baking step was performed to reduce water content in the photoresist thereby increasing its etch resistance.

After loading the patterned substrate into the vacuum chamber an argon pre sputtering step was performed to remove contaminants from the sample surface, thus improving the quality of the final thin film. Permalloy was deposited using DC magnetron sputtering. The steps following Py despotion depended on the number of lithography steps used to define the final thin film structure. In the single mask

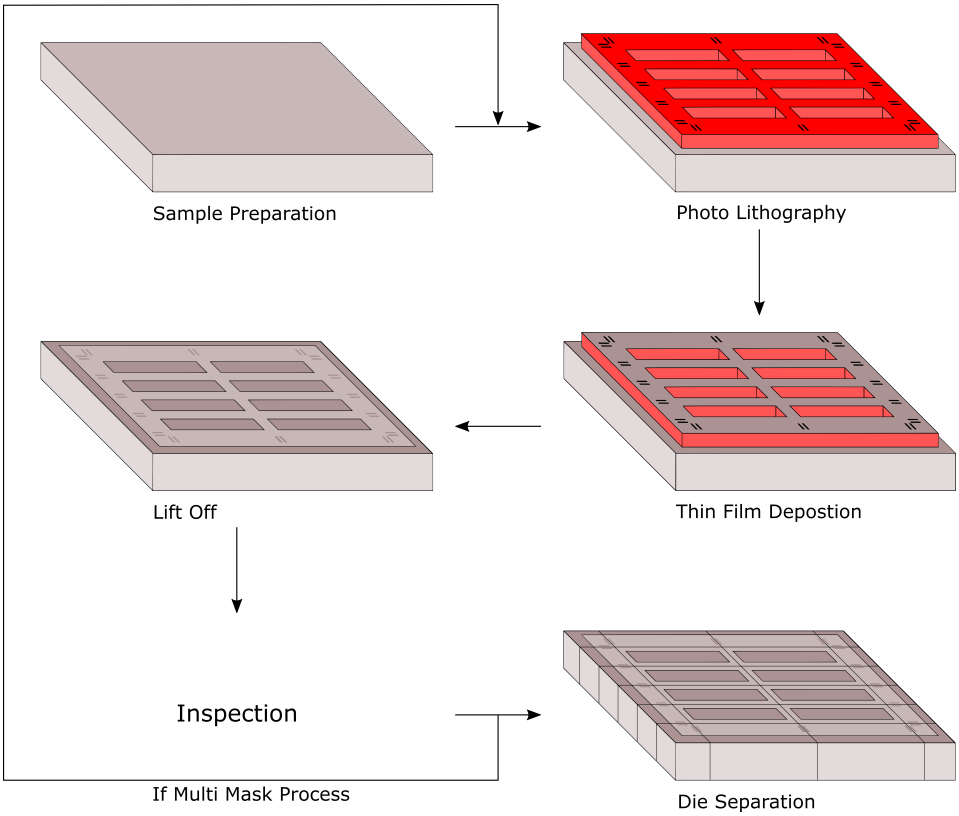

Figure 4.1: Illustration of the primary fabrication steps used to manufacture the studied Permalloy / Gold thin film structures.

process gold was deposited directly on top of Py by E-beam evaporation. A lift off process was then performed to dissolve the photoresist, leaving only the thin film stacks in direct contact with the substrate. In the multi mask process lift off was performed directly after Py deposition followed by a second lithography process transferring a secondary pattern to the substrate, thus allowing one to vary the geometry of the gold layer independently of the Py layer.

After completing the final lift off process all samples were inspected by optical microscopy to reveal defective samples. Individual samples produced on the same silicon support were then separated using an automated scriber and breaker and the samples sorted based on optical inspection data. AFM microscopy was used to measure the height of deposited thin films. FMR spectroscopy was used to study the magneto dynamical response of produced samples.

4.2 Fabrication Techniques

The following section describes the primary fabrication techniques used in the fabrication of studied thin film structures.

4.2.1 Photolithography

Photolithography is a micro-fabrication technique used to transfer a geometric pattern from a photomask to a photosensitive polymer (photoresist) [30]. The photomask corresponds to a UV transparent plate, usually quartz or soda lime glass, covered by a patterned UV absorbing film defining the transferred geometric features. By aligning the photomask to a resist covered substrate followed by a UV exposure through the mask, the resist areas not blocked by the mask pattern are exposed to the radiation. The physical properties of the exposed areas are then modified based on the type of resist. In positive resists the exposed areas show an increased solubility to a developer solution as the UV radiation activates photo acid generators decomposing the polymer chains in the resin. In negative resists exposed areas are less soluble as the UV radiation initiates cross linking in exposed regions. Negative resists typically yield resist sidewalls with an undercut, making it appropriate for lift off applications. Positive resists tend to yield straight sidewalls [30].

In this thesis the AZ5214E image-reversal resist was chosen to transfer the designed mask pattern. The primary feature of this resist is that its intrinsic positive properties can be changed to mimic that of a negative resist through a heat treatment step after exposing the resist to UV radiation [6]. Before this heat treatment the exposed resist becomes soluble due to the activation of photo acid generators. Upon development these areas are dissolved yielding relatively straight sidewall features. A heat treatment step following exposure, however, cross links the polymer chains in exposed regions making these areas inert to both the developer solution and further UV exposure. These traits can be exploited to produce lift off compatible T-shaped sidewall features. This is achieved by first selectively exposing the upper resist layer with a low exposure dose followed by a heat treatment step. This initiates cross linking making the top layer in regions not covered by the photomask inert to further processing steps. A subsequent flood exposure without a mask makes the remaining resist soluble to the developer. Upon development the flood exposed regions dissolve, leaving an undercut below the cross linked top layer. An illustration of the described process is shown in figure 4.2.

Another advantage of the tuneability associated with this resist is that it allows for the effective removal of edge beads. During spin coating viscous forces tend to result in an increased resist thickness, or bead formation, near the edges of the sample. These beads result in a poor contact between the mask and resist layer, thus affecting the resolution of the pattern transfer [30]. In the lithography process used in the fabrication of the studied Permalloy/Gold bilayer stacks these edge

beads were removed by selectively exposing the sample edge followed by a developer step. This edge bead removal step was executed before the patterning exposure. The AZ5214E IR resist is also thin (approximately 1.4µm) relative to the other standard resists provided by NTNU Nanolab, making it the preferred choice for lift off applications. Arguments against using this resist include a time consuming lithography process due to the need for more processing steps. The AZ5214E IR resist also proved to be difficult to optimize due to an increased number of process variables compared to conventional positive and negative resists.

4.2.2 Physical Vapor Deposition

Physical vapor deposition (PVD) constitutes one of the primary techniques employed in thin film deposition. In a PVD process a gaseous or atomic flux of the desired material is directed towards the substrate causing film growth upon adsorption. Parameters affecting thin film quality include substrate cleanliness, material adhesion to substrate, substrate temperature, deposition rate, energy of incident particles and mean free path of source atoms.

In this project the AJA Custom ACT-2200V PVD deposition system in NTNU Nanolab was used to deposit Permalloy, Gold and Titanium thin films. The primary components of this deposition system includes a load lock, a vacuum chamber capable of a base pressure in the 10^{-8}Torr regime, 5 magnetron sputtering heads and an electron beam evaporation system. The modes of operation used to produce the investigated Py/Au bilayers include:

Substrate Pre-sputtering

In the substrate pre-sputtering mode a bias is applied to the sample and an argon plasma used to sputter the surface. This allows for the removal of contaminants still present on the sample surface prior to thin film growth, thereby improving the quality of deposited films. User specified operating parameters included: Argon pressure, argon flow rate, plasma operating power and sputtering time.

DC Magnetron Sputter Deposition

In the magnetron sputtering deposition mode an argon plasma is used to dislodge atoms from a sputtering target, creating a flux of the sputtered material towards the sample [30]. The rate of deposition is controlled by the argon pressure/argon flow rate in the vacuum chamber and applied plasma power. The deposition rate for a given argon pressure and applied power is measured before each deposition using a quartz crystal micro-balance and the measured rate used to calculate the appropriate sputtering time needed to achieve a thin film of the desired thickness.

It should be noted that the AJA has its magnetron sputtering heads tilted at an angle of approximately 20° relative to the normal axis of the sample holder, thus necessitating a rotation of the sample stage during deposition.This tilt had an

impact on the choice of photoresist used to define the geometry of the bilayer structures as severely sloped or T-shaped photoresist sidewalls were necessary to prevent the sputtered material to cover the sidewalls of the resist, thereby complicating the lift off process.

Electron Beam Evaporation

The E-beam evaporation mode was utilized in the deposition of gold and titanium thin films. In this mode of operation an electron beam is scanned across a crucible containing the material to be deposited. This evaporates the source material producing a gaseous flux which precipitates into solid form on contact with surfaces in line of sight to the crucible. During deposition a quartz crystal micro-balance is used to measure the deposition rate in real time. After the desired thickness has been reached a shutter is used to cover the sample, thereby terminating the deposition. User specified input parameters included deposition rate and desired film thickness.

4.2.3 Die Separation

To separate samples produced on the same silicon support a Dynatex DX-III automated scriber and breaker was used. In the scribing process a diamond tip is used to accurately scratch the silicon surface in a user defined grid pattern. After scribing, a cushion is pushed against the top side of the sample while an impulse bar delivers an impact directly below the scribe lines, thereby breaking the wafer along the scratched lines. A side effect of this die separation procedure is the deposition of silicon dust particles on the surface of the samples.

4.3 Fabrication Procedure

The following sections present the experimental procedure used to fabricate the studied Permalloy/Gold thin film stacks. The processing steps involved in producing the studied structures are described and used process parameters presented.

4.3.1 Substrate Preparation

The silicon substrates used in the fabrication process were scribed from 4 inch highly resistive silicon wafers using a Dynatex DX-III automated scriber and breaker. The size of each silicon support was chosen based on the dimensions of the mask pattern used in the process to follow.

To remove dust particles and organic contaminants present on the silicon supports a 5 minute ultrasonic treatment in acetone was performed. Following sonication the samples were first immersed in an ethanol bath under gentle stirring to dilute the acetone wetting the sample surface followed by an immersion in isopropanol. After removing the samples from solution the supports were further rinsed in IPA before drying the samples using a nitrogen gun. Care was taken to prevent acetone from drying on the sample surface during chemical cleaning as this would result in a residue contaminating the silicon surface. This was achieved by never allowing the droplet wetting the sample surface to evaporate until after the final IPA rinse.

To remove any organic contaminants still present on the supports an oxygen plasma treatment was performed using the Diener Electronics Femto plasma cleaner in NTNU Nanolab. In addition to removing organic compounds this processing step also improves photoresist adhesion. Table 4.1 lists the process parameters used during oxygen plasma cleaning. To reduce the risk of surface contamination all subsequent processing steps were completed within a 12 hour time frame following substrate cleaning.

Table 4.1: Process parameters used during the oxygen plasma clean

O_2 flow [%]	Plasma power [%]	Etch time [min]
50	90	10

4.3.2 Photolithography

The presented AZ5214E recipe is an adaptation of a reciepe developed by Jonas M. Riibe [31], a concurrent PhD candidate at NTNU. As the minimum feature size on the photo mask used in this project was 5µm sub micron resolution was preferred. This was achieved by adding an edge bead removal step to the original recipe which improved the contact between the mask and photo resist, thereby enhancing pattern transfer resolution. A cross section illustration of all lithography steps is given in figure 4.2.

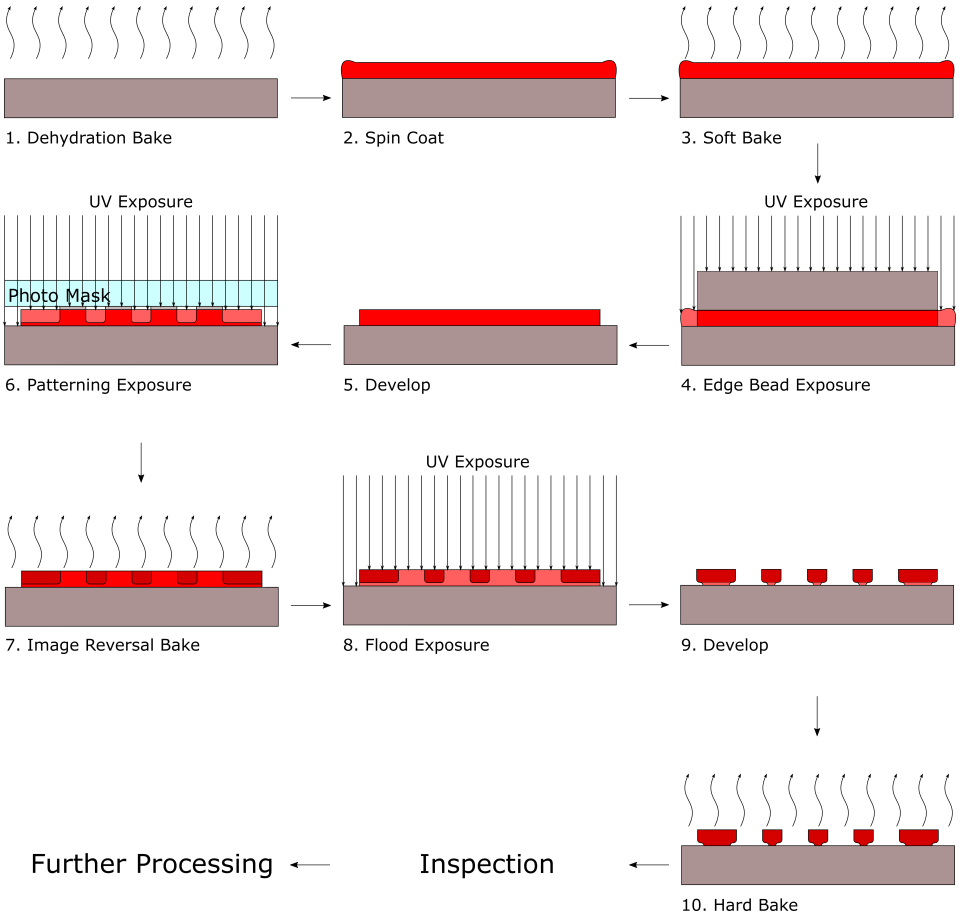

Figure 4.2: Step by step illustration of the used lithography process

1. Dehydration bake:
   To improve resist adhesion Si supports were baked on a hot plate for 5min at 150°C to drive out water from the substrate. Following the dehydration bake samples were left to cool in air for over 1min before the photo resist was applied.

2. Spin coating:
   The AZ5214E image reversal resist was applied to the Si supports in a spin coater. During spin coating a ramp rate of 4000 RPM was used and a spin speed of 4000 RPM maintained for 45s.

3. Soft bake:
   Samples were baked on a hot plate for 60s at 95°C to drive out excess solvents from the resist. SEM cross section microscopy revealed that this resulted in a resist thickness of approximately 1.3µm.

4. Edge Bead Removal:
   To remove edge beads from the resist covered samples a secondary piece of silicon, henceforth referred to as an EBR mask, was scribed such that its lateral dimensions were slightly smaller than that of the sample. These EBR masks were rinsed in an ultrasonic acetone bath followed by a bath in IPA between each use to remove any particles, organic contaminants or old resist adhering the surface.

   - The sample was placed in the MA6 mask aligner
   - The active area of the resist was covered by manually placing an EBR mask on top of the sample. This piece was aligned such that at least 1mm of all sample edges were exposed.
   - The sample was subjected to an i-line dose of 825mJ cm^{-2} thus exposing only the resist along the edges to the radiation.
   - The sample was developed in an AZ726 MIF developer solution under gentle stirring for approximately 10-15s until the silicon along the sample edges became visible. The development time was then extended to twice this period resulting in a 100 % over develop[1]
   - The sample was removed from the developer solution and rinsed under running DI water for 1min before moving the sample to a second running water bath for 1min. This step terminates the development process while also removing any dissolved resist from the sample surface. Samples were dried using a nitrogen gun following the DI rinse.

5. Alignment and Exposure:
   The sample was placed in the Suss MA6 mask aligner and the photo mask shown in appendix B aligned to the substrate. To simplify die separation

[1] The thickness of the edge beads was found to be approximately 3 times the thickness of the homogeneous resist layer. The EBR development time was left to a minimum as problems were encountered during the masters pre-project when developing for 45 seconds or more.

scribe marks in the first lithography layer were aligned with the crystallographic axes of the substrate. For samples produced using multiple lithography steps care was taken to accurately align the mask to alignment marks deposited during the initial process iteration. To ensure optimal resolution the MA6 hard contact mode was used during patterning exposures. Following alignment the sample was exposed to an i-line dose of $16\text{mJ}\,\text{cm}^{-2}$

6. Image Reversal Bake:
   The sample was placed on a hot plate for 120s at 110°C to cross link the exposed resist. Cross linking was terminated by moving the sample to a cold plate for approximately 1 minute.

7. Flood Exposure:
   To make the non-cross linked regions of the resist soluble to the developer solution the samples were placed in the Suss MA6 mask aligner and exposed to an i-line dose of $200\text{mJ}\,\text{cm}^{-2}$

8. Develop:
   Samples were developed in an AZ726 MIF developer solution under gentle stirring for 1min. The development process was terminated by submerging the sample in a running DI water bath for 1min before moving it to a second running water bath for 1min. A nitrogen gun was used for drying the samples.

9. Hard Bake:
   To enhance the etch resistance of the photo resist samples were baked on a hotplate for 50s at 120°C. This cross links the photo resist making it inert to further exposure, thus allowing optical inspection of the resist without deteriorating its structural properties.

10. Inspection:
    To ensure a defect free resist all samples were inspected by dark field optical microscopy prior to thin film deposition. If the resist showed defects in active regions the sample was stripped in acetone and the fabrication process started over.

The obtained photoresist undercut profile and lift off resolution of the described lithography process is depicted in Figure 4.3. As shown the obtained sidewall profile correspond to the desired T-shaped, thus providing lift off compatibility with the used sputter deposition technique. The lift off resolution also satisfied the requirement of sub micron replication of designed photomask features.

4.3.3 Photomask

To define relevant FM/NM thin film geometries a photomask was designed during the masters pre-project leading up to this thesis. This section will present the mask sections used in the current project. For a more complete description of designed features, mask layout and included supporting structures the reader is directed to Appendix B.

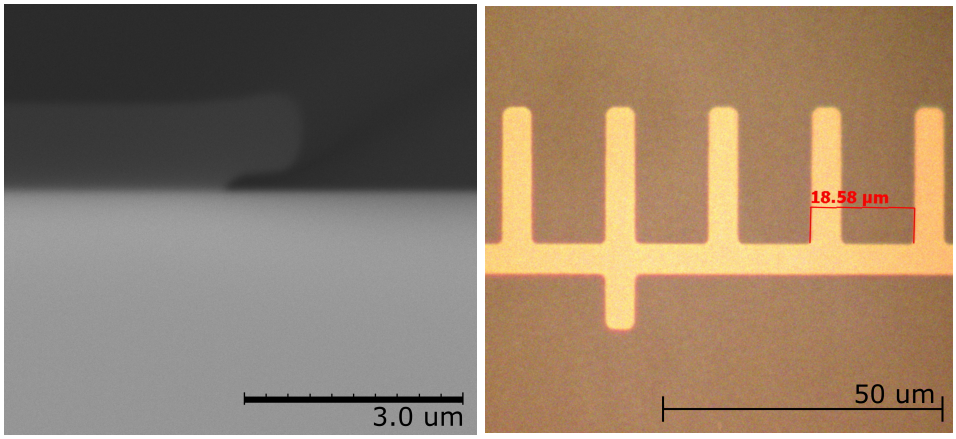

(a) Resist sidewall profile

(b) Lift off precision

Figure 4.3: (a) Cross section SEM image of obtained photoresist sidewall features when using the described lithography receipt. (b) Illustration of a portion of an alignment mark after completing the lift off procedure. The spacing between venier marks was as shown measured to 18.6µm using an optical microscope, whereas the corresponding feature on the photomask measured 18.5µm.

The designed mask pattern was realized by the Ångström micro-structure laboratory in the form of a soda lime glass mask with a chromium pattern. The resolution of the chromium patterning process was 1µm whereas the minimum feature size of the designed pattern was 5µm. The mask pattern is shown in Figure 4.4 where sectors containing different geometries have been labeled. FM/NM thin film structures corresponding to these geometries are illustrated in Figure 4.5.

4.3.4 Thin Film Deposition

All thin films grown in this project were deposited using the AJA ACT-2200V deposition system in NTNU Nanolab. After loading the sample into the vacuum chamber an ion gauge was used to record the chamber pressure. Operating pressures were found to vary between 10^{-7} and 10^{-8}Torr depending on previous user activity.

- Substrate Sputtering:
  Before depositing films in direct contact with the silicon surface (Py/Ti) a substrate sputtering step was performed to remove contaminants still present on the sample surface. After sample loading the argon flow rate was set to 67 ccm and the argon pressure to 30mTorr. The plasma was ignited at 50W in the substrate biasing mode, the argon pressure immediately reduced to 3mTorr and the reflected RF power tuned to zero. A sputtering time of 1min was maintained for all samples. Before proceeding with subsequent deposition

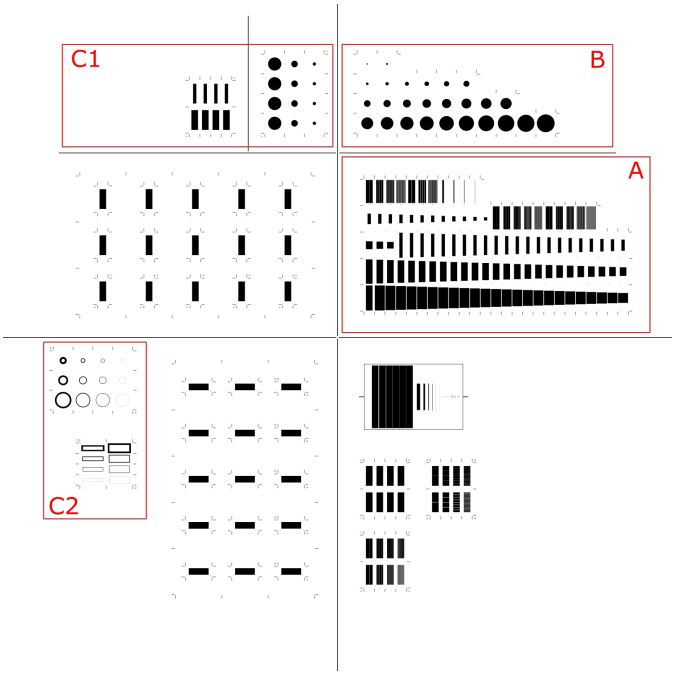

Figure 4.4: Photomask layout. Indicated sectors show samples produced on the same silicon support.

steps the argon flow rate was set to zero and the chamber vented for at least two minutes to allow the chamber to reach high vacuum.

- Permalloy deposition rate:
  To ensure accurate control over the thickness of produced thin films Permalloy rate checks were performed before each batch production of FM/NM samples. During Permalloy rate checks a quartz crystal micro-balance (QCM) was placed in the position of the sample holder and the Permalloy plasma head ignited using the same argon pressure/flow parameters as during actual Py deposition. After allowing the sputter rate to stabilize the QCM shutter was opened for exactly one minute to allow the deposition of Permalloy on the resonating quartz crystal. During Py deposition several key deposition parameters were recorded: Plasma power, bias voltage and DC current. As a change in these parameters indicates a change in deposition rate these values were used as a reference during actual Py deposition by ensuring that recorded values match those obtained during the previous rate check. After closing the QCM shutter the quartz crystal was allowed to cool for several minutes. Once the recorded thickness stabilized this value was used to calculate the current deposition rate for Permalloy. During the spring of 2015 little drift was observed in the deposition rate of Permalloy.

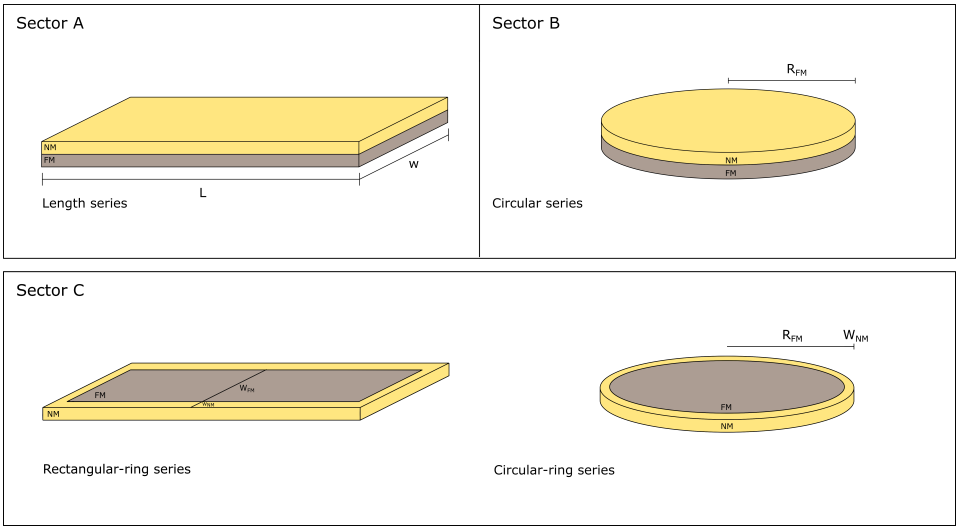

Figure 4.5: Thin film geometries within respective mask sectors. Labels indicate geometric features varied within each sample series. To best illustrate the intended geometry of produced FM/NM thin film structures the thickness of drawn samples has been exaggerated.

- Permalloy deposition:
  The sample shutter was disengaged and automatic rotation of the sample stage initiated. Argon pressure/flow was set to 30mTorr/67 ccm and the Permalloy sputtering head ignited at 50W. The argon pressure was reduced to 3mTorr and the sputtering head power ramped up to 100W at a ramp rate of $1\,\mathrm{W\,s^{-1}}$. After reaching the desired sputtering power the sputter head was left to pre sputter for 1min to remove the oxide layer covering the Permalloy target. To achieve a final film thickness of 10nm the source shutter was opened for a length of time depending on the previously recorded deposition rate. Sputtering output parameters were noted during deposition to verify that the used deposition rate corresponded to that found during the previous rate check.

- Electron Beam Evaporation:
  The electron beam evaporation mode was used during deposition of both Au and Ti thin films. This process was fully automated apart from the user having to manually change the crucible containing the material to be deposited. The target film thickness for gold and titanium was set to 10nm and 3nm respectively and the deposition rate to $5\,\mathrm{\AA\,s^{-1}}$ for both materials. Titanium was only used as an adhesive layer between silicon and gold as flaking due to poor adhesion was observed in its absence. Rotation of the sample stage was initiated during all depositions to ensure a homogeneous film.

4.3.5 Lift Off

After depositing the desired materials on top of the resist covered substrate lift off was performed by immersing the sample in acetone for up to several hours. This dissolves the photoresist causing the thin film covering the resist layer to float off, leaving only the deposited film in direct contact with the substrate. During lift off care was taken to prevent the acetone solution from drying, thus leaving an acetone residue on the samples. This was achieved by covering the beaker with a petri dish or aluminum foil. Following lift off the samples were cleaned in an ethanol bath followed by a subsequent bath in IPA, as done during sample cleaning. A nitrogen gun was used to dry the samples.

After completing the final lift off procedure produced samples were inspected using an optical microscope. Dark field microscopy was used to verify that produced thin films were free of point defects while bright field microscopy was used to verify that the lithography process replicated mask features with sufficient accuracy. The location of defective samples was noted and these discarded during die separation.

4.3.6 Die Separation

The Dynatex DX-III automated scriber and breaker was used to separate samples prepared on the same silicon wafer. After mounting the sample in the scriber the scribe axes were aligned according to scribe marks deposited during sample fabrication, these being aligned with the crystallographic axes of the silicon support. The following scribing parameters were found to successfully break the 500µm thick silicon wafer along the scribed lines (1.6x4mm pieces for rectangular thin film geometries and 3x3mm for circular geometries):

- Scribe force: 1700 cnts
- Scribe speed: $12\text{mm}\,\text{s}^{-1}$
- Break pressure: 60kPa

A milar cover was used to cover the sample during breaking to prevent contaminants on the sciber cushion from contaminating the sample surface. After completing the scribing program the milar cover was removed and a nitrogen gun used to remove large silicon particles released during breaking. Samples were subsequently sorted according to previous optical inspection notes.

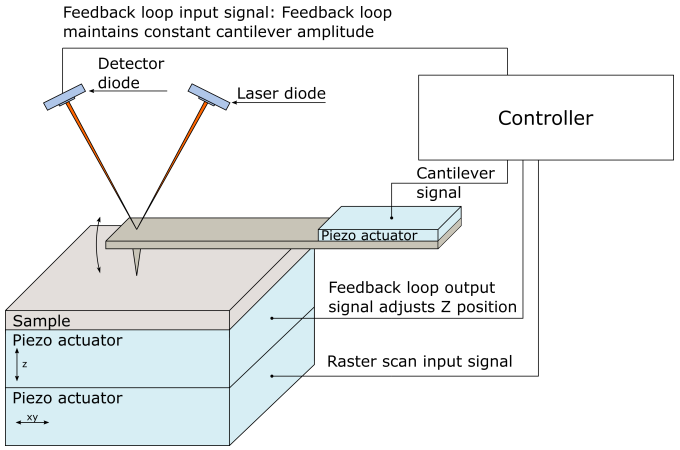

Figure 4.6: Schematic illustration of an AFM tapping mode setup

4.4 Characterization

The following section will introduce the primary characterization techniques used in this study, these being Atomic Force Microscopy (AFM) and Ferromagnetic Resonance (FMR) spectroscopy. A brief introduction to the respective techniques is first given before describing how the equipment was used.

4.4.1 Atomic Force Microscopy

Atomic Force Microscopy is a powerful characterization technique used to probe the surface properties of a sample in a fast, accurate and non-destructive manner. Since its conception [2] AFM has become one of the most widely applied surface characterization techniques due to its versatility regarding applicable sample types and the variety of surface properties it may examine. While properties such as magnetization, piezoresponse, electrostatic charge and mechanical characteristics are attainable with the appropriate AFM setup, only topological information was of interest in this project. The following introduction will therefore focus primarily on this aspect of AFM imaging.

The basic working principles in AFM imaging are illustrated in Figure 4.6. As shown a fine tip attached to a cantilever is scanned across the sample. As the tip interacts with topological features on the sample surface Van der Waals forces cause a deflection of the tip or modulation of the tips resonance frequency depending on the mode of operation. To detect changes in resonance frequency or cantilever deflection a laser is reflected off the back of the cantilever and the vertical and horizontal deflection in the reflected beam measured using a split photo diode detector. In tapping mode AFM, the mode of operation used in this project, the cantilever is driven to oscillate close to its resonance frequency by a piezoelectric

actuator. As the tip interacts with the surface the oscillation amplitude changes, thereby changing the RMS output of the photo detector. This output signal is fed to a feedback loop which adjust the vertical separation of the tip and sample by means of a piezoelectric actuator. A topological image of the sample is obtained by continuously adjusting and recording the tip separation to maintain a constant oscillation amplitude while rastering the tip across the sample surface. Even though tapping mode AFM is somewhat limited in terms of scan rates, scan size and lateral resolution, its out of plane resolution is in the sub nanometer regime making it applicable for step height measurements. Tapping mode AFM was in this thesis primarily used to validate that the thickness of deposited thin films matched the values predicted by deposition rate measurements. These measurements were performed using the Bruker AFM Veeco setup in NTNU Nanolab. The Bruker ScanAsyst software package was used during all measurements to automatically adjust critical scan parameters such as the tip setpoint, scan rates and feedback gain.

The following procedure was used during all AFM measurements: After mounting the ScanAsyst-Air tip the laser was tuned such that it both reflected off the tip of the cantilever, and such that the reflected spot was aimed at the center of the four point photo detector. Samples were then mounted on a magnetic pad using a double sided adhesive tape and placed within the AFM setup. To measure the height of the thin films the cantilever was guided to the edge of a step using the optics mounted on the AFM setup. The tip was then lowered in close proximity to the sample and the tip engaged to initiate the imaging process.

4.4.2 Ferromagnetic Resonance Spectroscopy

Ferromagnetic resonance spectroscopy constitutes one of the most widely applied experimental techniques in the study of ferromagnetic thin films. In an FMR experiment a static magnetic field is applied in conjunction with an orthogonal RF magnetic field. As previously discussed this excites the collective precession of electron spins provided that the frequency of the applied field coincides with the resonance frequency of the spin ensemble. The coupling between the induced precession and the applied pumping field can be tuned by varying either the applied magnetic field strength, thereby tuning the Lamour frequency, or by adjusting the frequency of the applied RF field. At resonance, when the two frequencies match, a maximum coupling is achieved resulting in an increased absorption of electromagnetic radiation. The corresponding dip in the microwave spectrum can be used to determine the resonance field/frequency which provides valuable insight for several physical parameters of interest, these not being limited to magnetic anisotropies, the gyromagnetic ratio, saturation magnetization and the Curie temperature [7,35]. The shape and linewidth of obtained absorption curves also provides information regarding the relaxation mechanisms related to magnetic damping [7]. FMR lineshapes have also been used in the study of spin pumping and inverse-spin-hall effects which are of significant interest in spinstronics applications [17, 28].

To measure the FMR response of produced FM/NM thin film structures a commercial Bruker Elexsys E500 EPR system was used. In this setup the studied sample is subjected to a homogeneous time varying magnetic field at a fixed frequency by means of a microwave resonator cavity coupled to a radiation source. Additionally, a static magnetic field is applied at right angles to the RF field and the field strength tuned until FMR is achieved. While sweeping the field the absorption of microwave energy is recorded as a function of applied field strength by measuring the microwave power reflected off a microwave cavity resonator in which the studied sample is mounted. A schematic illustration of the systems core components is depicted in Figure 4.7, these being:

- nA electromagnet with a field range of 0-7000 Gauss. This component subjects the sample to a static magnetic field, homogeneously magnetizing the studied sample while also tuning the ferromagnetic resonance frequency. During field sweeps a hall probe is used to accurately adjust the applied field according to set-point values.

- Field modulation coils were used to add a slow sinusoidally varying component to the static magnetic field. This functionality is used for lock-in detection purposes which greatly improves the sensitivity of absorption spectra as static noise components are filtered out.

- A microwave bridge housing a solid state radiation source used to generate microwaves, a microwave attenuator controlling the microwave power output, a circulator ensuring a directional dependence in transmission between waveguide ports, a Schottky barrier diode detector used to measure the reflected microwave power and a spectrometer used to identify the resonance frequency of the loaded cavity.

- A Bruker ER 4122 SHQ cylindrical cavity resonator ($Q_{unloaded}$=7500). This component serves to amplify and focus the magnetic component of an applied RF field in the sample position.

- A goniometer enabling sample rotation with respect to the static field.

In the used setup a radiation source is connected to a microwave cavity. To achieve maximum energy transfer between the cavity and source the impedance of the cavity is carefully matched to the impedance of external waveguide components. When critical impedance matching is achieved, all microwaves incident on the cavity are absorbed such that little radiation is reflected back towards the circulator and consequently the diode detector. The cavity resonator is constructed such that incident radiation of a frequency equaling the cavity resonance frequency is stored as standing waves within the resonator. In the used ER 4122 SHQ cavity the sample is positioned such that only the magnetic component of the standing microwave overlaps with the sample position, thus immersing the sample in an approximately homogeneous RF magnetic field as illustrated in Figure 4.8. The energy build up within the cavity and corresponding amplification in wave amplitude is dictated by

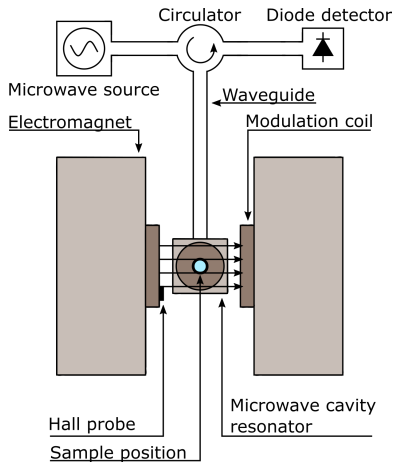

Figure 4.7: Schematic illustration of key FMR spectrometer components.

the quality factor of the cavity, defined by:

$$Q = 2\pi \frac{\text{Stored energy}}{\text{Energy dissipated per cycle}} \tag{4.1}$$

When sweeping the static magnetic field through the resonance condition of the studied sample an increased dissipation of energy is achieved by virtue of FMR, this drastically reducing the quality factor of the cavity. The corresponding change in the cavity impedance results in the cavity no longer being critically matched to external waveguide components, causing an increase in microwave reflection towards the diode detector. Absorption curves presented in later sections correspond to the detector signal as a function of the applied static field strength. FMR absoprtion curves were measured for different static field orientations by rotating the sample mounting rod in between field sweeps.

When modulation of the static field is used in conjunction with lock-in detection the recorded signal becomes a linear function of the first derivative in sample power absorption, P_S, with respect to H_0:

$$\text{Signal} = \kappa \frac{\partial P_S}{\partial H_0} \tag{4.2}$$

The proportionality constant κ here depends on the lock-in modulation amplitude, diode detector voltage, the loaded cavity quality factor and size of the cavity/waveguide coupling hole [36]. As both the coupling hole size may change slightly from sample to sample in the cavity tuning process care must be taken when comparing amplitude data from different samples.

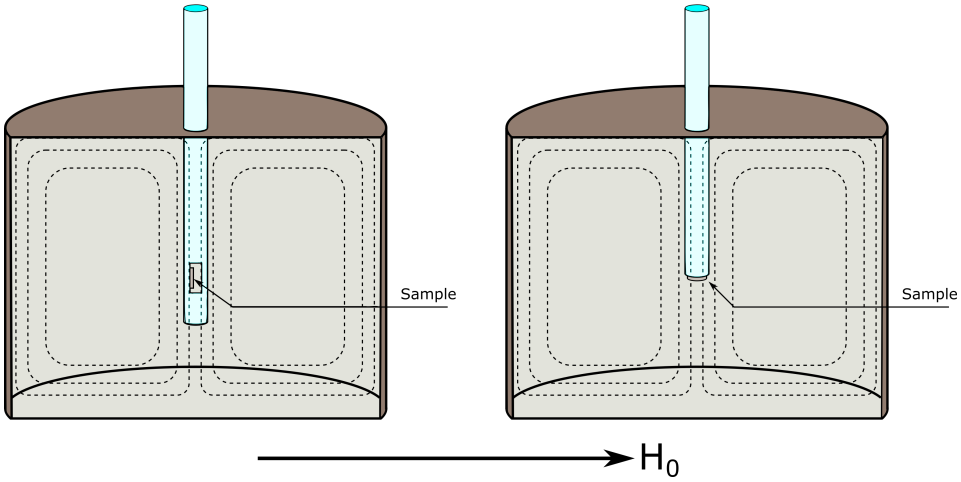

Figure 4.8: Schematic illustration of sample positioning with respect to the magnetic component of the standing wave. Dotted lines here indicate field lines associated with the magnetic component of the standing wave. The left image illustrates the sample positioning when using the horizontal mounting rod. As shown this provides an in plane orientation of the static field whereas the ac field component is directed along the sample plane normal. When using the vertical mounting rod as shown in the right image the RF field component is directed in the plane of the sample whereas the direction of the static field depends on the angular orientation of the mounting rod.

4.4.3 FMR Procedures

As the described FMR setup was used to measure trends in FMR lineshapes for varying sample geometries, care was taken to perform experiments in a repeatable fashion. The following sections describe the procedure used when loading and tuning the microwave cavity, as well as used experimental parameters.

Sample Loading

As shown in Figure 4.8 two different quartz mounting rod types were used to position the studied sample in the microwave cavity, depending on the desired orientation of the RF field. The horizontal mounting rod (left) was used for most studied samples as it provides an out of plane orientation of the RF field, thus facilitating the excitation of eddy currents in NM thin film structures. Samples were mounted by first applying a layer of grease to the end of the cylindrical quartz rod. The back side of the sample was then attached and centered at the end of the rod and lowered into the microwave cavity. To ensure that all samples were positioned at the same height within the cavity, thereby assuring equal field exposure, tape was wound around the quartz rod at the desired height to limit its vertical motion. Care was also taken to align samples with respect to the static

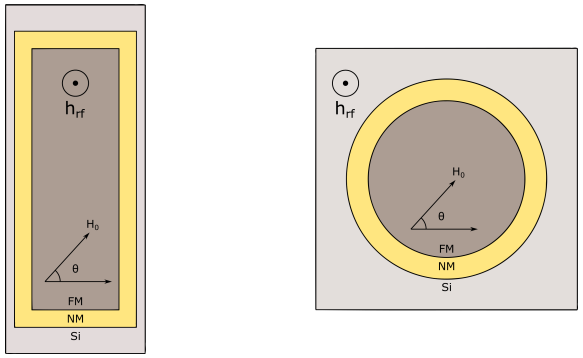

Figure 4.9: Top down illustration of rectangular and circular sample geometry positioning with respect to the applied magnetic fields in conducted FMR experiments

field direction. Figure 4.9 illustrates the position of rectangular and circular sample geometries with respect to the applied field when using the horizontal mounting rod. The illustrated angle corresponds to the goniometric rotation of the sample during FMR experiment. As indicated rectangular samples were mounted such that the static field was directed along the short axis of the sample during the initial field sweep. Circular samples were positioned with an arbitrary substrate axis in the field direction.

Cavity Tuning

As previously mentioned the cavity based FMR technique relies on impedance matching between the cavity and external waveguide components. To achieve this condition the sample was first lowered into the cavity and the microwave bridge spectrometer set to sweep across a range of frequencies. The resonance frequency of the loaded cavity was identified by locating the frequency yielding a minimum in power reflection from the cavity. The resonance frequency of the loaded cavity was for the studied samples 9.385GHz ±5MHz, where the frequency was found to vary slightly with the geometry of the sample. After locating the resonance frequency an iris screw was adjusted to tune the size of the cavity/waveguide coupling hole, thereby tuning the impedance of the cavity. Optimal impedance matching was achieved when the dip in the microwave spectrum was at a maximum, thereby indicating a minimum in the reflection of incident microwaves.

In the described FMR setup a Schottky barrier diode detector was used where the change in reflected microwave power was measured as a change in the diode current. For this component to function optimally the diode current must be biased such that induced changes in current occur around a setpoint in the linear region of the diode I-V curve. For the used diode detector the optimal biasing current was 200mA. This biasing level was achieved by further adjusting the iris screw, thereby intentionally introducing an offset in the impedance of the cavity with respect to

external waveguide components. This reduces the coupling between the source and cavity, thus causing a reflection of microwaves even in the off resonance condition. In the used FMR setup the appropriate biasing level was achieved by initiating the automatic fine tuning functionality provided by the Bruker Xepr control software.

The estimated amplitude of the confined standing wave for a given microwave power was according to the Bruker EPR manual

$$|\mathbf{h_{rf}}|[G] \cong C \cdot \sqrt{P[W]} \tag{4.3}$$

where C=2 when using the ER 4122 SHQ cavity.

Xepr Input Parameters

A list of the primary set of input parameters used during conducted FMR experiments is found in Table 4.2.

Table 4.2: List of Xepr parameters used for all conducted FMR experiments. Each experiment took approximately 1-2 hours depending on the used angular step size.

Parameter	**Value**
Resonance frequency	∼9.385GHz
Magnetic field range	600-2100G
Data points / field sweep	1024
Attenuation gain	25dB
Microwave power	0.6325mW
Approximate rf field amplitude	∼ 50mG / 5µT
Angle range	360°
Angle step size	2-4°
Temperature	296K
Receiver gain	40dB
Time constant	10.24 ms
Conversion time	20.48 ms

4.5 Data Analysis

To simplify the comparison of FMR spectroscopy data a parameterization of extracted absorption curves was performed using the expression derived in chapter 3. This was achieved by means of a MATLAB script in which individual absorption curves were fitted to function (4.4) using a linear least square error algorithm.

$$\begin{aligned}\text{Signal} = A\frac{8(H_R - H_0)}{[4(H_R - H_0)^2 + (\Delta H)^2]^2} \\ + B\left[\frac{-1/\Delta H}{4(H_R - H_0)^2 + (\Delta H)^2} - \frac{8(H_R - H_0)^2/\Delta H}{[4(H_R - H_0)^2 + (\Delta H)^2]^2}\right] \\ + \alpha_1 H_0 + \alpha_0 \end{aligned} \tag{4.4}$$

This enabled the extraction of the following parameters:

- A [A.U.][2] - Amplitude of the symmetric lineshape component associated with dissipative susceptibility terms, as depicted in Figure 3.2 (a)
- B [A.U.] - Amplitude of the asymmetric lineshape component associated with dispersive susceptibility terms, as depicted in Figure 3.2 (b)
- H_R [Gauss] - Applied magnetic field strength yielding resonant absorption of radiation in the sample.
- ΔH [Gauss]- Measure of the absorption curve linewidth, as described in section 2.4.3.
- $\beta = B/A$ - The shape of recorded absorption curves was characterized primarily by the parameter β, which describes the ratio between the symmetric and antisymmetric lineshape amplitudes.
- α_1/α_0 [A.U.] - To account for offsets in the detecor signal a linear term was added to equation (4.4). α_0 accounts for the offset biasing of the detector diode. α_1 was included to account for linear variations in the detector signal unrelated to FMR.

Figure 4.10 (a) illustrates the extracted absorption curve and corresponding curve fit for a circular 10nm Py thin film when directing the static field in the sample plane. As Figures 4.10 (c-f) illustrate, the used curve fitting procedure allows one to more easily visualize trends in the shape of FMR absorption curves when varying the static field direction.

For most investigated sample geometries, the only exception being the rectangular

[2]The units of A and B correspond to that of the detector output, which in the context of this report was considered to be arbitrary for all intents and purpouses

FM/NM thin film stacks, Figures 4.10 (c-f) provide an accurate representation of the angular dependence in lineshape paremeters. As such one may note that both the amplitude A and asymmetry parameter β display a negligible dependence on static field orientation, thus justifying the averaging of these parameters to gain a single parameter representing the sample. Despite the clear angular dependence is seen in both the resonance field H_R and linewidth ΔH these parameters were also averaged as the amplitude in these variations were in range of a few percent.

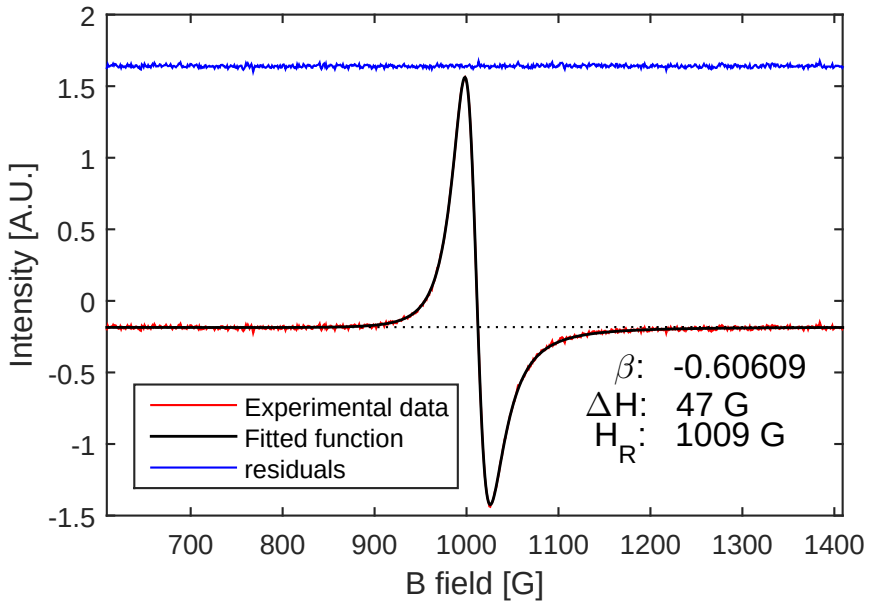

(a) FMR absorption curve

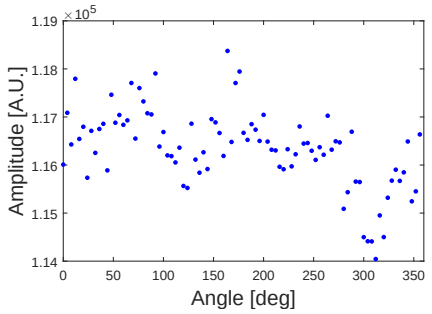

(b) Signal amplitude

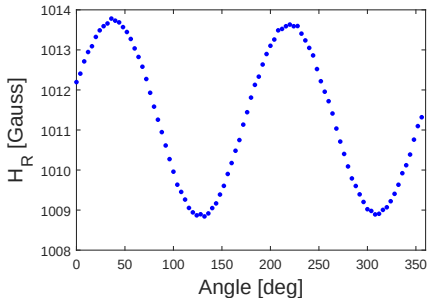

(c) Resonance field position

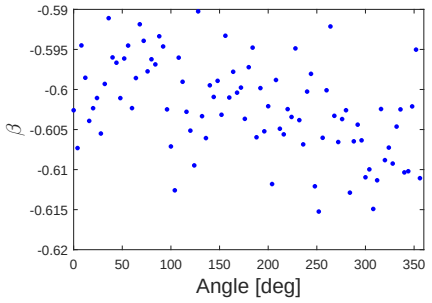

(d) Asymmetry parameter $\boldsymbol{\beta}$

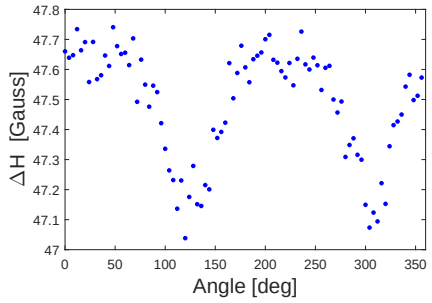

(e) Linewidth

Figure 4.10: Extracted FMR lineshape parameters for a 11nm thick Permalloy disk of radius 0.75mm when rotating the static field in the thin film plane.

Chapter 5

Results and Discussion

To study the eddy current field interaction in FM/NM thin film structures and its impact on FMR several thin film systems of varying geometry were prepared using the previously described fabrication process, each system intending to highlight different aspects of the eddy current field interaction. The following section will first present the chosen thin film geometries along with a discussion regarding their purpose. Topological defects introduced by the used deposition technique will also be discussed.

The second half of this chapter is devoted to the presentation and discussion of FMR spectroscopy results obtained from the analysis of produced thin film samples. Presented results were obtained using the FMR spectroscopy setup described in chapter 4 and the FMR absorption data processed using the curve fitting algorithm of section 4.5. The eddy current field interaction was in this study probed indirectly by mapping the induced change in extracted FMR lineshape parameters when varying the sample geometry and its orientation with respect to applied magnetic fields.

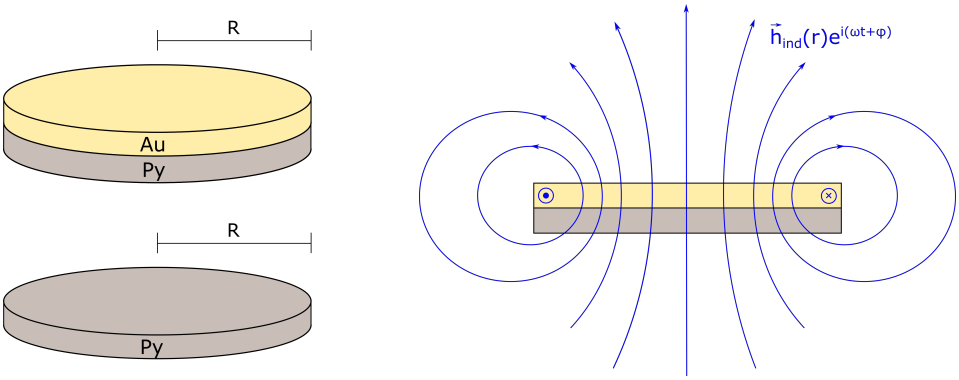

Figure 5.1: (Left) Illustration of circular Au/Py and Py thin film disk structures where varied geometric features have been labeled. The thickness of the structure has here been greatly exaggerated to best illustrate the sample geometry. (Right) Sketch of induced field distribution when assuming an induced current distribution localized primarily along the edge of the sample.

5.1 Sample Fabrication

The primary purpose of produced FM/NM samples was to provide a geometrically well defined system in which eddy current effects could be studied. This section will introduce the sample geometries chosen for this study and their intended purpose. The quality of produced samples will also be addressed.

The target thickness of thin films incorporated in fabricated structures was chosen based on results both obtained in the masters pre-project leading up to this thesis, and on results presented in Flovik et.al's initial work on this topic [10]. In the masters pre-project it was found that the FMR absorption curve linewidth decreased for increasing Py film thicknesses before stabilizing above 10nm. As a narrow linewidth was assumed in the curve fitting procedure a thickness of 10nm was chosen for all fabricated structures, this minimizing both film thickness and FMR linewidth. In Flovik et.al's study of eddy current effects in rectangular FM/NM thin film structures a maximum perturbation in FMR lineshapes was observed for an Au thickness of 10nm [10]. This thickness was therefore chosen for all deposited gold layers.

5.1.1 Circular Disk Structures

To provide a rotationally symmetric system for studying the eddy current field effect the circular photomask geometries of sector B were used to pattern thin films of Py and thin film stacks of Py/Au. As shown in Figure 5.1, resulting sample geometries correspond to circular disks of varying radius.

Table 5.1: Sample information for fabricated circular thin film structures. Listed thicknesses are based on the AFM measurements shown in Appendix D.1

Materials	Measured Thickness	Fabrication Date	Process Parameters
Py / Au	22nm	Nov. 2014	Table C.2
Py / Au	20nm	11.03.2015	Table C.6
Py	11nm	11.03.2015	Table C.5

The purpose of produced circular Permalloy structures was to provide a rotationally invariant system for measuring the baseline FMR response of deposited Py films. This simplified the characterization of Py thin film properties while also providing a reference for circular Py structures capped by Au or enveloped by Au rings. Circular Py/Au structures were chosen to investigate the eddy current field coupling as the axial symmetry of the system removes the angular degree of freedom from induced currents and associated induced magnetic fields, this potentially simplifying the verification of results through numerical simulation.

As the strength of induced eddy currents and the associated phase shifted field are expected to scale with the area of the conductor, trends in FMR lineshape parameters for varying sample area might provide valuable insights. The radius of produced circular samples was therefore varied from $R = 0.1$mm to $R = 1.25$mm at a step size of $\Delta R = 0.05$mm. All circular thin film samples were supported by identical 3x3mm silicon dies as defined by the photo mask scribing grid. During the course of this thesis three circular sample series were analyzed by FMR spectroscopy. Table 5.1 lists relevant sample information for these samples.

5.1.2 Ring Structures

To reduce the complexity of the studied system the ring structures of Figure 5.2 were employed. These structures correspond to circular or rectangular sheets of Py enveloped by a thin film Au ring. The primary purpose of these structures was to confine the current paths of induced currents, thus allowing one to approximate the magnitude of induced currents and associated magnetic fields using closed form analytical expressions. The confinement of induced currents to the plane of the Py thin film also simplifies the analysis of obtained FMR data as only out of plane components of the induced fields is expected to affect FMR.

Rectangular and circular ring structures were fabricated on the same silicon support by performing two consecutive lift off procedures. The lateral geometry of the Py thin film was first defined by transferring the mask pattern of sector C1 to the substrate, followed by sputter deposition of Permalloy. Following lift off a second lithographic pattern transfer was performed, where the pattern of sector C2 was aligned to deposited Py features. Due to poor adhesion between silicon and gold a 3nm Ti thin film was deposited as an adhesive layer before Au evaporation. Table 5.2 lists relevant sample information for the produced ring structures whereas Fig-

Table 5.2: Sample information for fabricated ring structures. Listed thicknesses are based on the AFM measurements shown in Appendix D.1

Materials	Measured Thickness	Fabrication Date	Process Parameters
Py / Au	11nm / 10nm	18-20.04.2015	Table C.7-C.8

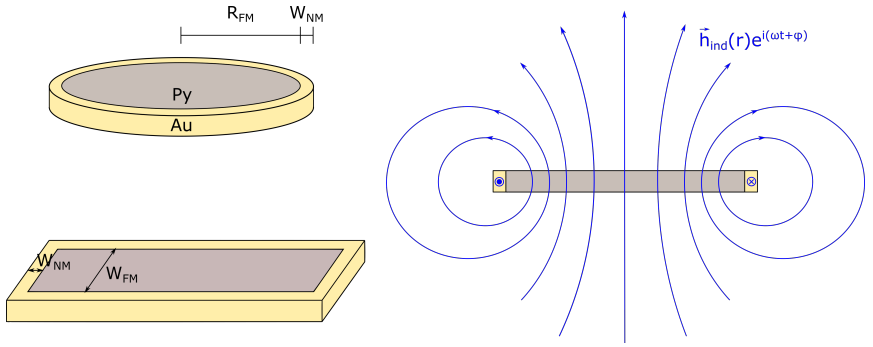

Figure 5.2: (Left) Illustration of circular ring structure where varied geometric features have been labeled. The thickness of the structure has here been greatly exaggerated to best illustrate the sample geometry. (Right) Sketch of induced field distribution when directing a time varying magnetic flux along the ring structure plane normal. As shown the induced field is assumed to produces a phase shifted field parallel to the plane normal.

ure 5.2 shows optical microscopy photos of the produced samples. An alignment error less than 1µm was achieved for analyzed ring structures, as indicated by depicted alignment marks.

To investigate how increasing the magnetic flux passing through the metal rings, thus enhancing the magnitude of induced eddy currents, affects FMR in adjacent FM thin films the lateral dimensions of both interior Py geometries end exterior Au ring structures was varied. For circular ring structures the inner Py disk diameter was varied as $R_{FM} = 250, 500, 1000$µm whereas inner rectangular Py sheets measured 1x3mm and 0.5x3mm. The width of the outer Au ring surrounding both sample types was varied as $W_{NM} = 10, 50, 100, 250$µm. Circular and rectangular ring structures were supported by 3x3mm and 1.6x4mm silicon dies respectively.

5.1.3 Rectangular Samples

As Flovik et.al's [10] previous research on this topic dealt with eddy current effects in rectangular FM/NM bilayer structures, rectangular samples of varying dimensions were fabricated using the mask features of sector A, this enabling the comparison of results. The lateral dimensions of fabricated rectangular thin film stacks are listed in Tables B.1-B.2 whereas relevant information for produced rectangular sample series is found in Table 5.3.

Table 5.3: Sample information for fabricated rectangular thin film structures. Listed thicknesses are based on the AFM measurements shown in Appendix D.1

Materials	Measured Thickness	Fabrication Date	Process Parameters
Py / Au	19nm	Nov. 2014	Table C.1
Py / Au	22nm	10.03.2015	Table C.4
Py	13nm	10.03.2015	Table C.3

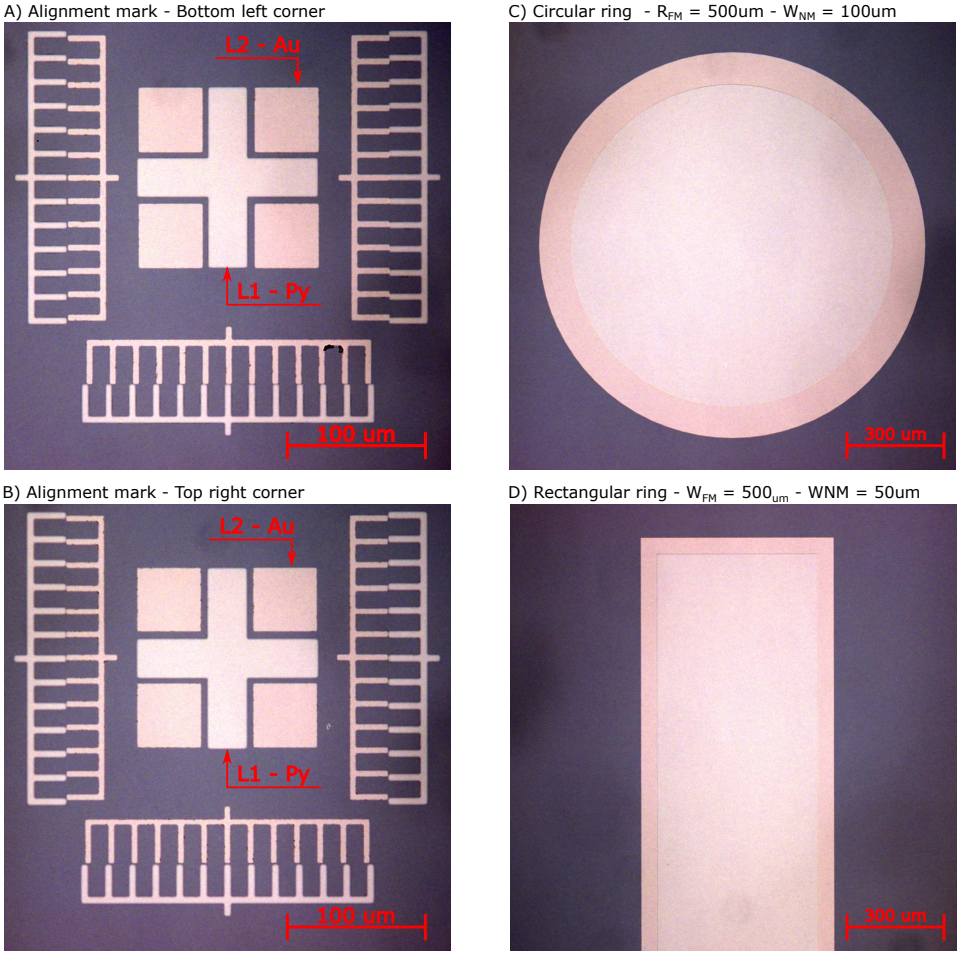

Figure 5.3: Optical microscopy photos of produced ring samples. Figure A) shows mask alignment at the bottom left corner of the photomask, whereas B) shows the alignment at the top right corner. Figures C) and D) show produced circular and rectangular ring structures

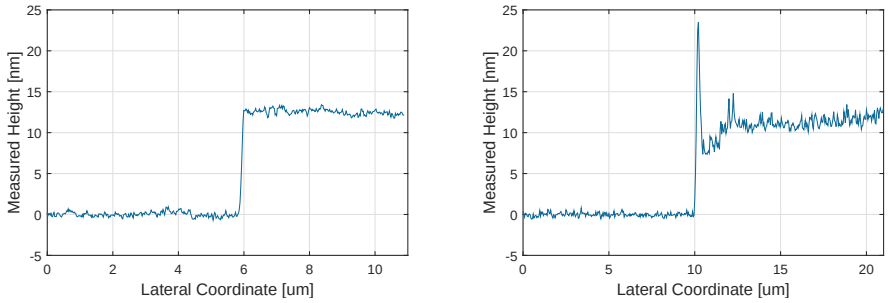

(a) AFM thickness profile - Au

(b) AFM thickness profile - Py

Figure 5.4: Measured AFM topography for (a) Au and (b) Py thin film structures fabricated using the lift off described in chapter 4. The target thickness of both films was 10nm.

5.1.4 AFM Characterization Results

The height and topology of deposited thin films was measured using the AFM technique described in section 4.4.1. For each sample series a single sample[1] was selected and analyzed by AFM and the obtained data used to produce the thickness profiles shown in Appendix D.1. These profiles formed the basis for the thickness estimates listed in Tables 5.1-5.3.

Figure 5.4 illustrates the measured thickness profiles of Au- and Py thin films patterned using the previously described lift off process. As shown the patterned Au structure displays a sharp transition between silicon and Au whereas spikes are seen along the edge of the patterned Py film. The observed Py stringers were likely caused by the tilted orientation of the magnetron sputtering head with respect to the sample stage, as described in section 4.2.2. This yields a line of sight between the Py target and resist sidewall, thus enabling the deposition of Py beneath the overhanging sidewalls. These edge imperfections were, however, deemed to be of little consequence in regards to the FMR response of produced FM/NM structures. As shown in Appendix 5.4 the Py stringers do not overlap with deposited Au thin films as they are located below the overhanging resist sidewall. The stringers should therefore not affect the induction of eddy currents in the Au layer as current paths are not disrupted. Furthermore, Py stringers are not expected to significantly affect the total FMR signal of a sample as their volume can be neglected compared to the total ferromagnetic volume of deposited thin film structures. In future experiments these edge defects could be eliminated by employing a hemispherical deposition technique or by replacing the lift off process with an etching scheme.

[1]Since the uniformity of the AJA sputtering system was $\pm 0.5\%$ over a 4" wafer, as indicated in the Norfab userguide, a single sample was deemed sufficient for estimating deposited thicknesses in each sample series

5.2 Ferromagnetic Resonance Results

To study the effects of eddy current induced magnetic fields on the FMR response of FM/NM thin films structures four thin film systems of varying geometry and composition were studied by FMR spectroscopy. In the following, obtained results from each system will be presented and discussed in order.

The FMR response of deposited Py thin films will first be discussed by considering results obtained from circular Py thin film structures of varying radius. Next, the FMR response of fabricated ring samples will be considered as the geometry of these samples allows one to neglect the effects of in-plane eddy current field components. Presented results also illustrates how the eddy current field interaction may be manipulated by varying the NM thin film geometry. The following topic of discussion is the effect of in-plane eddy current field components on the FMR response of FM/NM bilayer structures. This in-plane field interaction is first considered in a rectangular system before presenting results obtained for a circular bilayers.

Throughout the following discussion, perturbations in FMR lineshapes will be used as the primary measure of eddy current field interactions. As discussed in section 4.5 extracted FMR absorption curves were curve fitted to an expression on the form

$$\text{Signal} = A\frac{\partial\chi''}{\partial H_0} + B\frac{\partial\chi'}{\partial H_0} = A\left[\frac{\partial\chi''}{\partial H_0} + \beta\frac{\partial\chi'}{\partial H_0}\right] \tag{5.1}$$

The first term of equation (5.1) here corresponding to the normal FMR lineshape and the second term of amplitude B to a secondary lineshape component introduced by eddy current field interactions in the sample. To better characterize the shape of extracted FMR absorption curves the lineshape asymmetry parameter $\beta = B/A$ was introduced. Observed trends in extracted A and β will be interpreted according to the model presented in chapter 3.

5.2.1 Circular Permalloy Samples

To establish the baseline response of deposited Permalloy thin films FMR experiments were conducted for the circular Permalloy structures described in section 5.1.1. In these experiments the samples were mounted at the end of the horizontal mounting rod depicted in Figure 4.8 such that the magnetic RF field was directed along the thin film plane normal, this to mimic the field orientation used in the analysis of FM/NM structures. The obtained experimental data was analyzed using the procedures of section 4.5.

Figure 5.5 illustrates the observed trends in extracted FMR lineshapes for circular Py samples. The first thing to note is that the resonance field position H_R remains approximately constant for varying sample sizes, this implying that the resonance frequency ω can be assumed to stay unchanged for all investigated Py

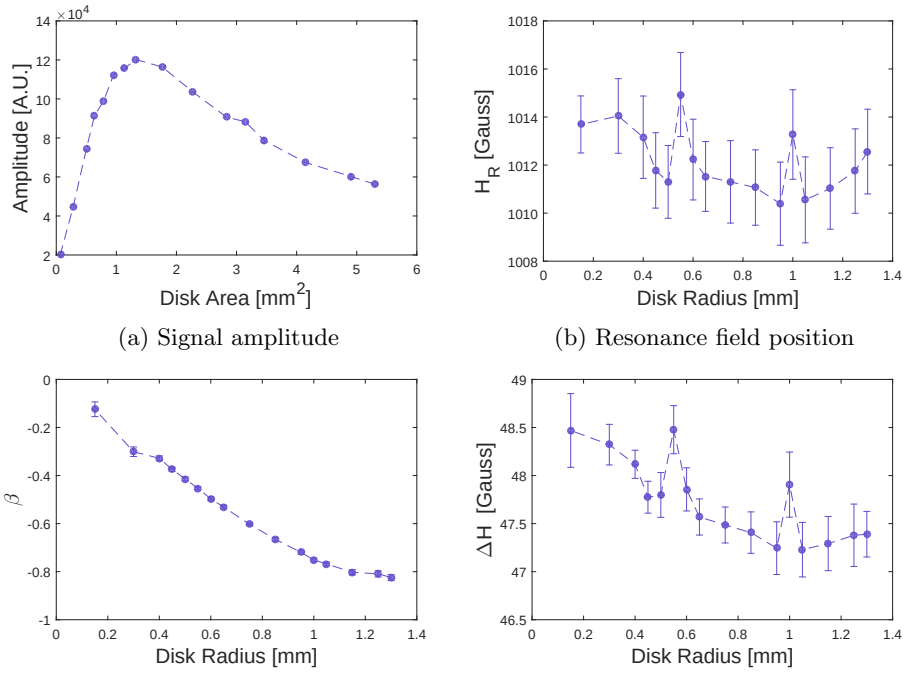

(a) Signal amplitude

(b) Resonance field position

(c) Asymmetry parameter β

(d) Linewidth

Figure 5.5: Averaged FMR lineshape parameters for circular Permalloy samples of varying radius. (a) illustrates trends in lineshape amplitude, (b) variations in resonance field position, (c) the radial dependence in the lineshape asymmetry parameter and (d) variations in linewidth. Error bars of one standard deviation have been included to illustrate the spread in extracted FMR parameters for each sample.

structures. The Py linewidth is also seen to be largely unaffected by variations in sample radius, as illustrated in Figure 5.5 (d). This observed radial invariance in linewidth and resonance frequency simplifies the comparison of signal amplitudes as A is proportional in both ω and ΔH(see equation (3.20)).

While H_R and ΔH show insignificant variations for varying sample radii, a definite radial dependence is seen in both signal amplitude and lineshape asymmetry (β). As shown in Figure 5.5 (a) the signal amplitude initially displays a linear dependence in area up to a sample radius of approximately 0.5mm. When further increasing the Py radius beyond this threshold an intermediate maximum is observed at a radius around 0.65mm followed by a subsequent decline. These trends do not correspond to the ideal FMR response of section 2.4.3 in which a linear amplitude dependence in volume ensued. Furthermore, Figure 5.5 (c) illustrates an increase in lineshape asymmetry, as characterized by β, for increasing sample radii. This also deviates from the perfectly symmetric absorption curves described

in section 2.4.3.

One possible explanation for the nonzero lineshape asymmetry and nonlinear trend in amplitude A is the induction of eddy currents in the Py thin film itself. As Py exhibits metallic properties, though with inferior conductivity as compared to Au [29, 38], the magnetic flux directed along the thin film normal may induce eddy currents of appreciable magnitude. Resulting inhomogeneous phase shifted magnetic fields would in this case be directed solely along the thin film normal ($h^y_{ind} = 0$) due to the in-plane confinement of induced currents. By invoking this field condition the model derived in chapter 3 yields the following expressions for signal amplitude and β;

$$A \propto \omega \Delta H |\kappa| h_{rf} \left[h_{rf} V_{FM} + \int_{V_{FM}} h^x_{ind}(\mathbf{r}) cos(\phi_x(\mathbf{r})) dV \right] \tag{5.2}$$

$$\beta \propto \frac{\int_{V_{FM}} h^x_{ind}(\mathbf{r}) sin(\phi_x(\mathbf{r})) dV}{h_{rf} V_{FM} + \int_{V_{FM}} h^x_{ind}(\mathbf{r}) cos(\phi_x(\mathbf{r})) dV} \tag{5.3}$$

$V_{FM} = \pi R^2_{Py} \tau$ being the sample volume, R_{Py} the radius of the Py film and τ its thickness. The first term of equation (5.2) here describes the linear area dependence of the lineshape amplitude seen in the ideal case whereas the second term accounts for amplitude perturbations caused by eddy current field interactions in the sample.

In section 2.5 the phase of eddy currents induced in a circular Au thin film was approximated to $\phi \sim -\pi$ when considering similar experimental conditions as those employed in this work. Since a similar current and phase distribution was found when repeating the calculations of Figure 2.8 with the material parameters of Py, the phase of induced magnetic fields will also be assumed to lie in the $\phi \sim -\pi$ range for the considered Py samples. As this implies a negative sign for the second term in equation 5.2 one expects the amplitude A to diminish for increasing eddy current field strengths. These predictions correspond well with the amplitude trends seen in Figure 5.5 (a): For small sample area the magnetic flux acting on the sample will be small, this resulting in weak eddy current excitations and correspondingly weak eddy current field interactions in the sample. Small samples are thus expected to display an approximately linear dependence on sample area due to weak secondary field interactions in the Py film. For larger samples the corresponding increase in magnetic flux will increase the magnitude of induced eddy currents and associated fields. When increasing the sample size beyond a certain threshold these fields will become comparable to that of the applied driving field, thus resulting in a reduction in signal amplitude.

Increasing eddy current field strengths for increasing sample area would also qualitatively explain the observed trends in the lineshape asymmetry parameter β, provided that the model presented in chapter 3 provides a reasonable physical description of the system. For increasing $h^x_{ind}(\mathbf{r})$ the denominator of equation 5.3

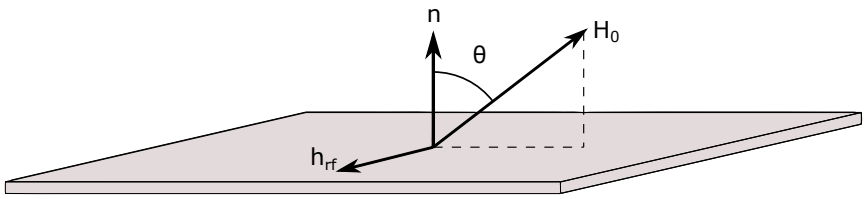

Figure 5.6: Field configuration with respect to the thin film plane when using the vertical mounting rod. As indicated, the angle enclosed between the static field and the thin film normal is varied between field sweeps.

is expected to diminish whereas the numerator is expected to grow increasingly negative. These predictions are in agreement with the trends seen in Figure 5.5 (c), in which the β parameter is seen to grow increasingly negative for increasing sample area.

To investigate whether the observed trends in asymmetry and amplitude could be a result of eddy current excitations in the Py sheets, secondary FMR experiments were conducted using the vertical mounting rod depicted in Figure 4.8. In these experiments the RF field is applied in the plane of the sample while the static field is rotated around the RF field axis. As Figure 5.6 illustrates, this field configuration directs the time varying magnetic flux in the sample plane rather than along the thin film normal, thus eliminating the possibility of eddy current excitations. To compare results obtained in these experiments with those obtained for a horizontal positioning of the sample, absorption curves corresponding to an in plane orientation of $\mathbf{H_0}$ were isolated such that the RF field orientation was the only varied quantity.

Figure 5.7 (a) illustrates the obtained absorption curve data for a single Py disk when rotating the sample plane with respect to the static field direction. As shown, the resonance field position, here located in the transition between blue and red regions, displays a significant angular dependence as explained by the demagnetization energy term of section 2.3. To isolate the absorption curves corresponding to an in plane orientation of both field components this angular dependence was exploited as the desired field configuration will yield a minimum in resonance field position. By localizing and curve fitting the corresponding absorption curves the data presented in Figure 5.7 was obtained. Included error bars indicate the spread in extracted parameters from the two in plane field orientations.

A comparison of extracted FMR lineshape parameters for the two RF field orientations is given in Figure 5.6 (b-e). As Figure 5.6 (b) illustrates, a linear amplitude dependence on sample area is seen for an in plane orientation of the driving field, the expected trend when neglecting eddy current field interactions. Furthermore, eliminating the possibility of eddy current excitations led to purely symmetric lineshapes, this indicated by the near zero values of β seen in 5.7 (d).

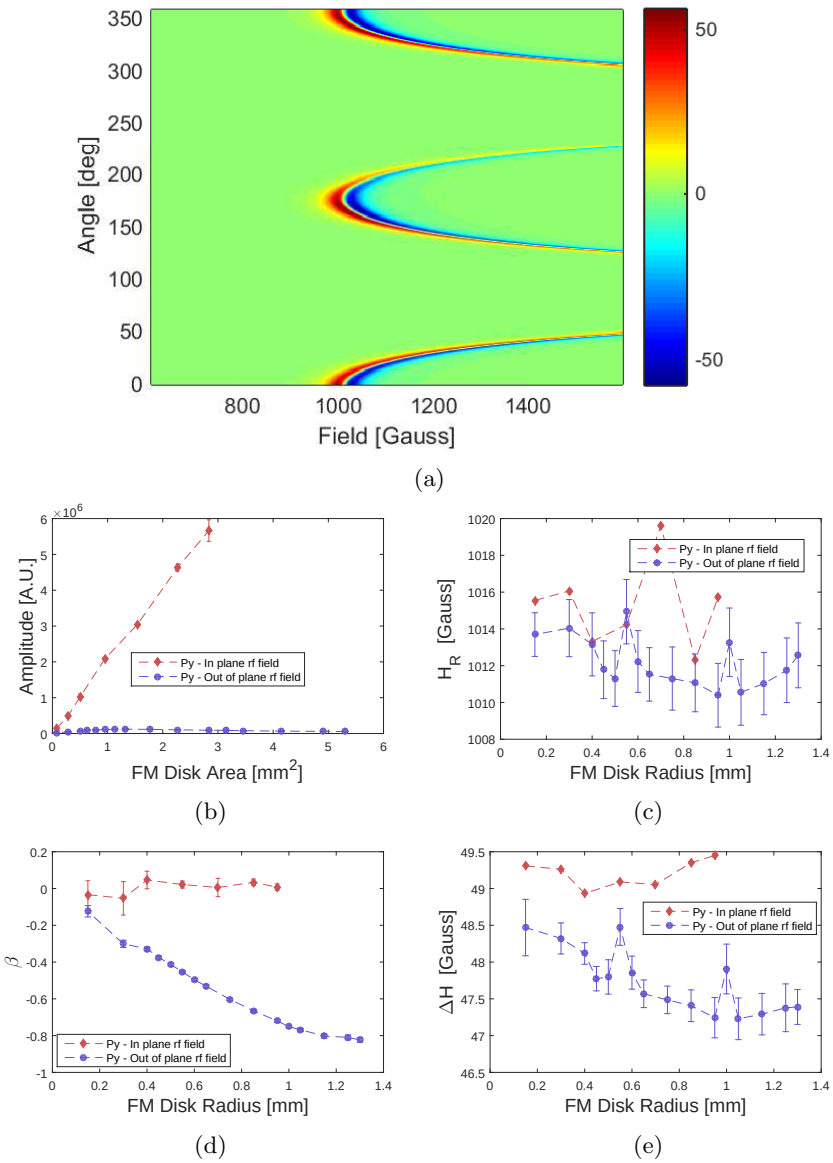

Figure 5.7: (a) Surface plot of FMR signal intensity for an RF field orientation in the sample plane. The indicated angle here corresponds to the angle enclosed by the static field and thin film normal. Angle = 0 corresponds to a static field orientation in the plane of the sample.(b-e) Extracted FMR parameters for an in plane orientation of both the static and RF field components plotted again the data of Figure 5.5. Error bars of one standard deviation have been included to illustrate the spread in extracted FMR parameters.

While these trends present strong evidence for a significant coupling between eddy currents and ferromagnetic resonance in Py alone, care should be taken in assessing the strength of associated magnetic fields. As Figure 5.7 (b) illustrates, the in plane orientation of the RF field results in a drastic increase in signal amplitudes as compared to samples analyzed using an out of plane field orientation. While this could be interpreted as an almost complete compensation of the RF field by virtue of eddy current excitations, an alternate explanation involves differences in the detector coupling coefficient κ for the two sample orientations. In the two sample positioning schemes the following experimental conditions differ; vertical sample position within the microwave cavity, shape of the mounting rod and sample orientation with respect to the confined magnetic mode. These differences will likely influence the quality factor of the cavity, thus introducing different detector coupling coefficients for the two experimental setups. Since the recorded amplitude is proportional in κ this difference would introduce a scaling offset in signal amplitudes, thus explaining the large difference. As such, a direct comparison of amplitude data does not provide a reliable measure of induced field strengths in the Py thin films.

Even though the strength of induced eddy current fields in Permalloy remains unknown eddy current effects are observed to significantly perturb the baseline FMR response of the system. These effects were not anticipated when designing the conducted experiment as eddy current effects are normally neglected even for highly conductive metals such as Au when considering thin film thicknesses below the EM skin depth. While this result is interesting in itself, it does complicate the study of eddy current interactions in FM/NM structures as it prevents the isolation of the NM-FM field interaction. Induced magnetic fields attributed to eddy currents in the Permalloy sheet will also complicate current calculations in the simple circular ring structures due to the inductive coupling between the Py sheet and Au loop, this making the application of simple closed form equations inaccurate.

As intrinsic eddy current effects in Permalloy complicates the study of eddy current interactions in FM/NM structures, Py would ideally have been replaced by a ferromagnetic insulator as this would prevent eddy current excitations in the FM itself. This was, however, well beyond the scope of this thesis as the deposition of ferromagnetic oxides typically requires novel fabrication techniques. A second approach for dealing with these intrinsic field effects is to compare experimental results with those obtained from a numerical model of the system. Efforts were made to develop a COMSOL Multiphysics model capable of simulating the induction of eddy currents and the resulting magnetic fields for the thin film geometries considered in this thesis. As these attempts proved unsuccessful the remaining discussion of experimental results will be qualitative in nature.

5.2.2 Circular Ring Structures

To study eddy current effects in a simple FM/NM system the circular ring samples described in section 5.1.2 were employed. As for the circular Py samples these ring structures were positioned in the microwave cavity using the horizontal mounting rod, thus facilitating the induction of eddy currents in the Au ring. The strength of these currents, and consequently the magnitude of associated magnetic fields, was in this sample geometry varied by adjusting the radius of the Py core or by changing the width of the Au loop enveloping the Py sheet, thus tuning the area of the sample and consequently magnetic flux acting on the loop.

Figure 5.8 illustrates the observed trends in extracted FMR parameters when varying the interior Py radius or exterior Au ring width of investigated ring structures. The first thing to note is the observed reduction in signal amplitude when increasing the Au ring width. As figure Figure 5.8 (a) illustrates, the recorded linewidth amplitude of FM/NM ring structures follows the same Py area trend as that of isolated circular Py structures when only considering a narrow Au ring. When the width of the exterior NM loop is widened a progressive decline in amplitude is observed, an indication of progressively stronger eddy current field interactions. This trend is further illustrated in Figure 5.8 (b) where the lineshape amplitude is plotted against Au ring width. As shown the amplitude drops for increasing loop widths. The rate at which the amplitude is diminished is also seen to increase with the radius of the Py core.

The observed trends in signal amplitude may be explained in a qualitative manner by similar arguments as those presented in the previous section. In the considered geometry the Py sheet is located in the same plane as the Au loop. As such, eddy current excitations in the Au loop will result in inhomogeneous magnetic fields directed along the thin film normal of the inner Py disk, this enabling the application of equations (5.2) and (5.3). When increasing the Au loop width the magnetic flux and consequently the electromotive force acting on the loop is enhanced. The current path of induced eddy currents will also be widened, this reducing the resistance of the loop. Both these trends should enhance the magnitude of induced eddy currents and associated phase shifted magnetic fields, thus reducing the signal amplitude according to equation (5.2).

As shown in Figure 5.8 (c-d) the tuning of either R_{Py} or W_{Au} also had an impact on the shape of recorded FMR absorption curves. These figures plot the extracted asymmetry parameter β for ring samples of $W_{Au} < 250$µm. As indicated, an increase in lineshape asymmetry is observed when increasing either R_{Py} or W_{Au}. These trends may be understood qualitatively by considering equation (5.3), as done in the previous section:

$$\beta \propto \frac{\int_{V_{FM}} h^x_{ind}(\mathbf{r}) sin(\phi_x(\mathbf{r}))dV}{h_{rf}V_{FM} + \int_{V_{FM}} h^x_{ind}(\mathbf{r}) cos(\phi_x(\mathbf{r}))dV}$$

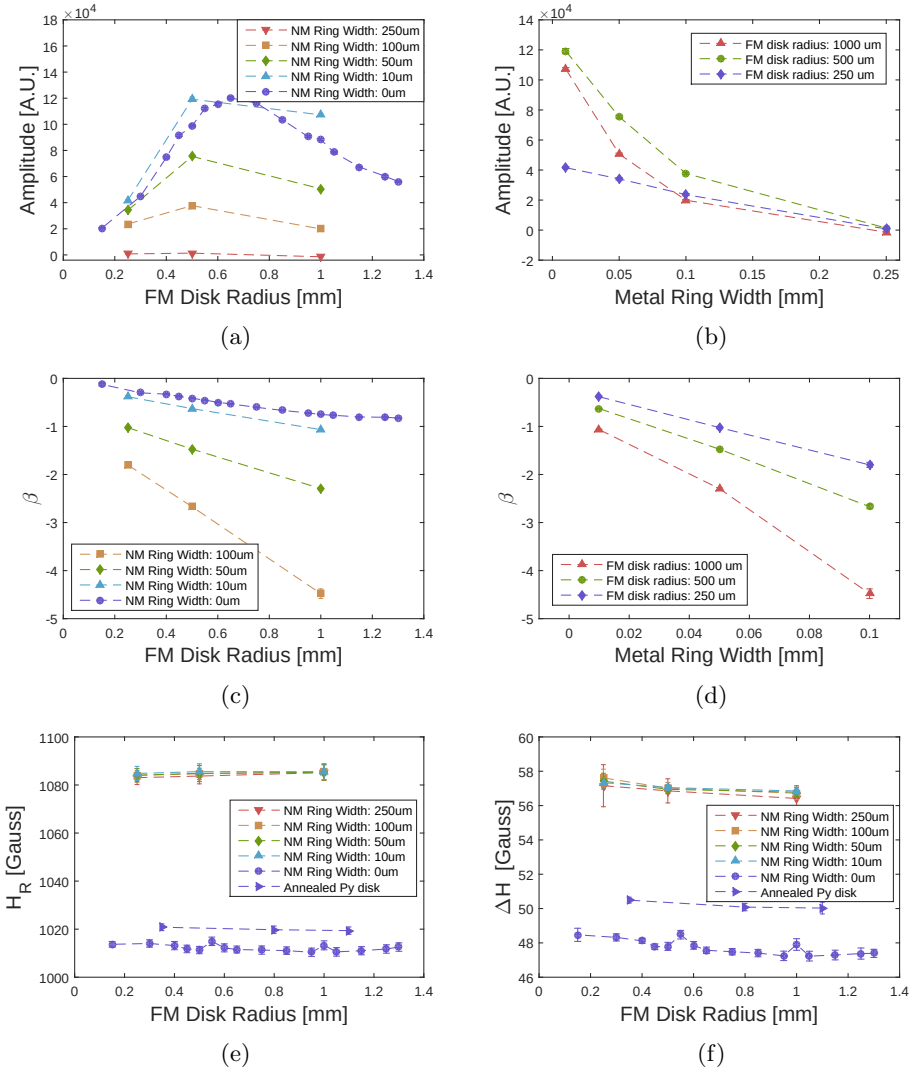

Figure 5.8: Averaged FMR lineshape parameters for circular Py disk structures enveloped by a Ti/Au ring compared to the circular Py reference samples (NM Ring Width : 0µm)

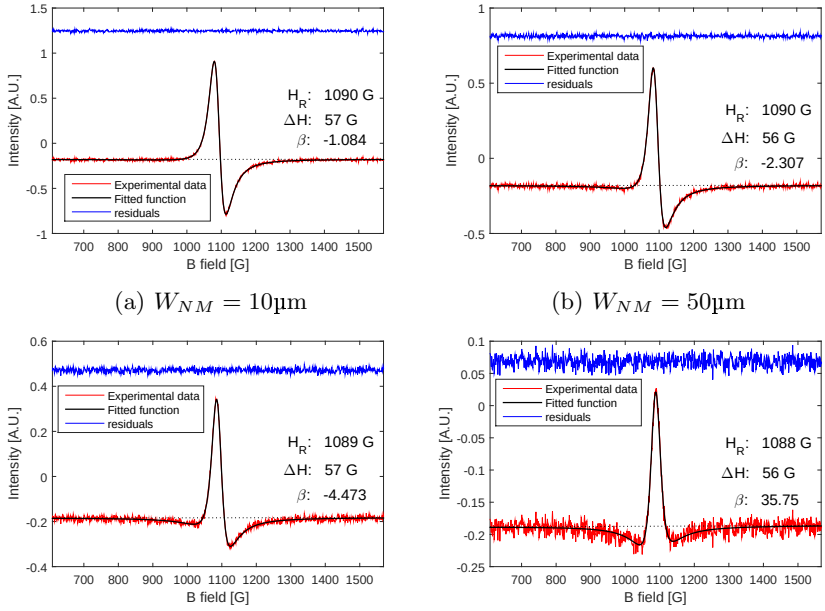

(a) $W_{NM} = 10\mu m$

(b) $W_{NM} = 50\mu m$

(c) $W_{NM} = 100\mu m$

(d) $W_{NM} = 250\mu m$

Figure 5.9: Extracted lineshapes for circular ring structures. The radius of the interior Permalloy disk is 1000µm

As discussed in section 2.5 the phase of currents induced in a metallic loop are expected to lie in the $\phi \subset [-\pi/2, -\pi]$ range. The denominator of equation (5.3) will therefore shrink in magnitude for increasing eddy current field strengths, whereas the numerator is expected to become increasingly negative. This is in agreement with the results presented in Figures 5.8 (c-d) as β becomes increasingly negative when increasing either R_{Py} or W_{Au}.

For ring structures of $W_{Au} = 250\mu m$ the amplitude A was observed to approach zero, this indicating a negligible signal contribution from the dissipative susceptibility term. This caused divergent values in the lineshape asymmetry parameter $\beta = B/A$, thus indicating that the dispersive component of the dynamic susceptibility dominates the FMR signal. This dominance is illustrated in Figure 5.9 where FMR absorption curves for varying Au widths are plotted. As shown, an increase in the exterior Au loop width results in a reduction in signal amplitude and a progressive distortion of FMR lineshapes. For a ring width of $W_{NM} = 250\mu m$ the lineshape is observed to be completely dominated by the real, dispersive susceptibility component depicted in Figure 3.2 (b).

In addition to the noted variations in lineshape amplitude and asymmetry Figure 5.8 (e-f) also indicate a significant shift in both resonance field position and

linewidth for studied FM/NM ring structures, as compared to the previously discussed circular Py samples. These discrepancies may be explained by considering the differences in fabrication procedures for circular Py samples and Py/Ay ring samples. As discussed in section 5.1, studied FM/NM ring samples were produced by performing two consecutive lift off procedures, whereas a single lift off iteration was used in preparing the circular Py structures. Consequently, the Py thin films incorporated in the ring systems will have been exposed to the substrate baking steps included in the lithography receipt which could have promoted further oxidation of the Py surface [9]. To investigate weather this was the case a few circular Py reference samples were exposed to the dehydration baking step. As shown in Figure 5.8 this promoted a small shift in both resonance field position and FMR linewidth. The observed shift was, however, not as large as the shift observed in fabricated ring samples. This difference could be a result of heat treated reference samples not being exposed to the remaining processing steps.

5.2.3 Rectangular Py/Au Bilayer Structures

In Flovik et.al's [10] initial study of eddy current effects in FMR, investigated thin film samples were prepared by scribing 10nmPy/10nmAu and 10nmPy/10nmCu multilayers into rectangular geometries of dimensions 1xLmm, where L was varied [10]. As a significant rotationally dependent distortion of extracted FMR absorption curves was reported, similar geometries were included in this study to further investigate the system. It should be noted that the FMR data presented in this section originates from samples produced during the pre-project leading up to this masters thesis. All FMR experiments were, however, conducted during the course of this thesis. The horizontal mounting rod was used in all experiments to facilitate the excitation of eddy currents in the Au thin film.

Before considering how the sample area affects the shape and magnitude of extracted absorption curves the FMR response of a single rectangular bilayer must be addressed. Figure 5.10 (a) depicts the FMR signal intensity of a 0.5x2.4mm rectangular bilayer when rotating the static magnetic field in the sample plane. In contrast to the rotational symmetry seen in circular geometries, the shape and magnitude of FMR absorption curves is observed to show a dependence on the in plane static field orientation. This angular dependence is further illustrated in Figures 5.10 (b-e) where extracted lineshape parameters are plotted against the angle enclosed by the static field vector and the short axis of the sample[2]. As shown in Figure 5.10 (b) the lineshape amplitude A is seen to oscillate during the full 360° rotation of the static field, it reaching its maximum value for field orientations parallel to the sample short axis. It should also be emphasized that the lineshape amplitude changes sign at multiple field orientations during rotation. At corresponding angles the lineshape asymmetry $\beta = B/A$ is seen to diverge, this indicating that the dispersive component of the dynamic susceptibility dominates the FMR signal. This point is further emphasized in Figures 5.11 where FMR absorption curves for multiple static field orientations are shown. As illustrated, a weak asymmetry is observed when directing the static field along the short sample axis (Angle=12°), this indicating only weak eddy current field interactions. When rotating the sample with respect to the static field an increase in lineshape distortion is observed due to the mixing of dispersive and dissipative dynamic susceptibility terms. At $\theta = 74°$ and $\theta = 126°$ the dispersive component of the susceptibility is seen to fully dominate the FMR detector signal as the amplitude of the dissipative term approaches zero.

Apart from described trends in amplitude and asymmetry Figure 5.10 illustrates anomalous trends in H_R and ΔH, as compared to the FMR response of the circular Py reference samples. As shown in Figure 5.10 (c) a small bump in the resonance field position is seen at $\theta \approx 50°$ and $\theta \approx 230°$. This perturbation was observed to stay approximately constant in both magnitude and angular position for all analyzed rectangular bilayer structures. The linewidth of rectangular FM/NM

[2]Due to a slight misalignment of the sample the angles reported in Figure 5.10 are shifted by approximately 10 degrees, the actual $\theta = 0$ corresponding to the maximum in amplitude

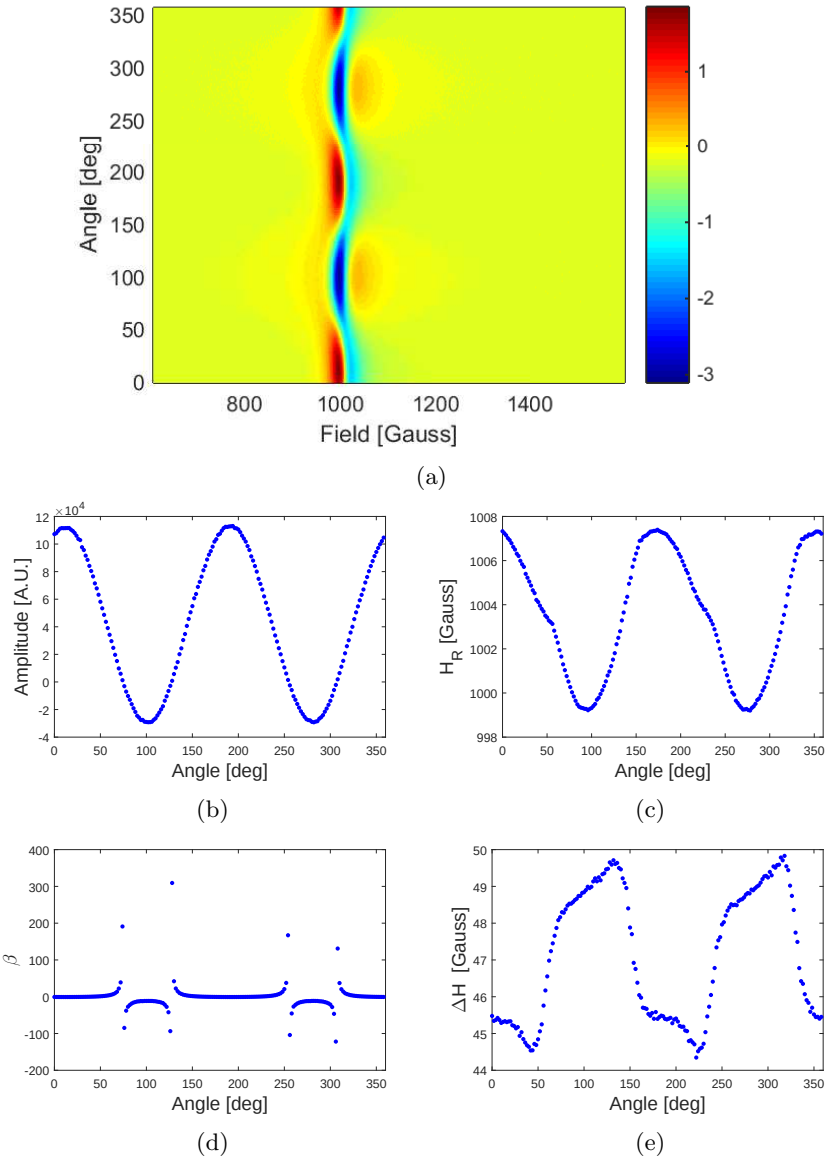

Figure 5.10: (a) Surface plot of FMR signal intensity for a rectangular Py/Au thin film stack of dimension 0.5x2.4mm. (b-e) illustrates how extracted FMR lineshape parameters depend on the orientation of the static magnetic field. Angle = 0 corresponds to an approximate field orientation along the short axis of the rectangular sample.

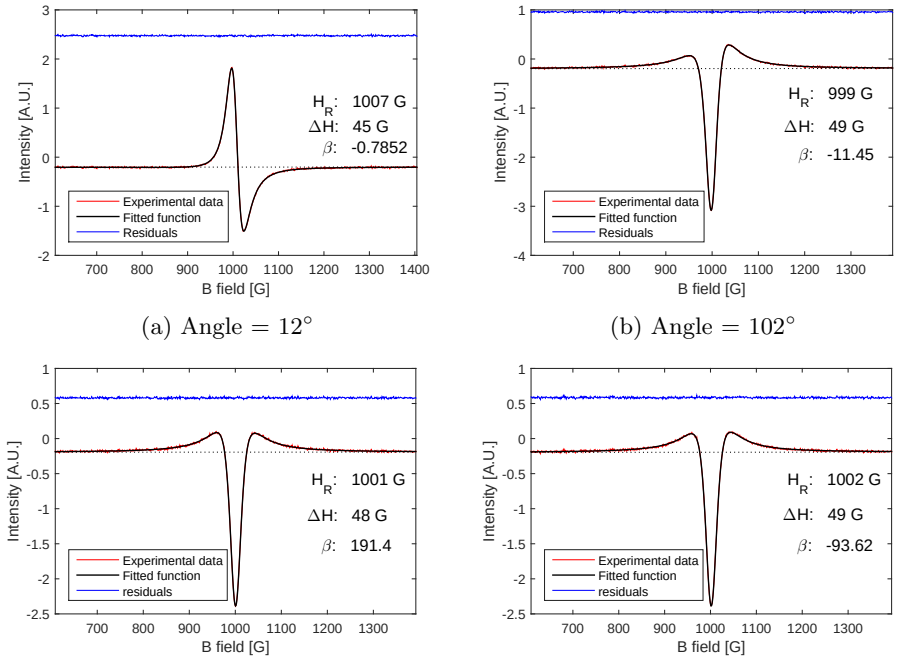

(a) Angle = 12°

(b) Angle = 102°

(c) Angle = 74°

(d) Angle = 126°

Figure 5.11: Selected absorption curves for a 0.5x2.4mm rectangular bilayer. (a) and (b) illustrates the absorption curves for a static field orientation along the short and long sample axes respectively, whereas (c) and (d) depicts extracted curves for angles corresponding to $A = 0$.

structures was also observed to be distinctly different from that of uncapped Py. As shown in Figure 5.10 (e) a significant increase in linewidth is observed when rotating the static field towards the long axis of rectangular bilayers, which could indicate an increase in damping along these directions. Furthermore, the angular variations in ΔH do not display rotational symmetry, this indicating that the phenomena inducing this enhancement in linewidth is not solely correlated to the geometry of deposited FM/NM structures. As the physical mechanisms responsible for observed angular variations in H_R and ΔH have not yet been identified these trends are merely noted.

To describe the observed angular dependence in the shape and magnitude of analyzed FMR absorption curves the spatial distribution of induced currents and associated magnetic fields must be considered. In the used experimental setup the RF magnetic field is directed along the thin film normal. As discussed in section 2.5, this will result in the induction of eddy currents in the plane of investigated bilayer structures, where the current density is expected to be highest along sample edges. The spatial distribution of induced eddy currents and associ-

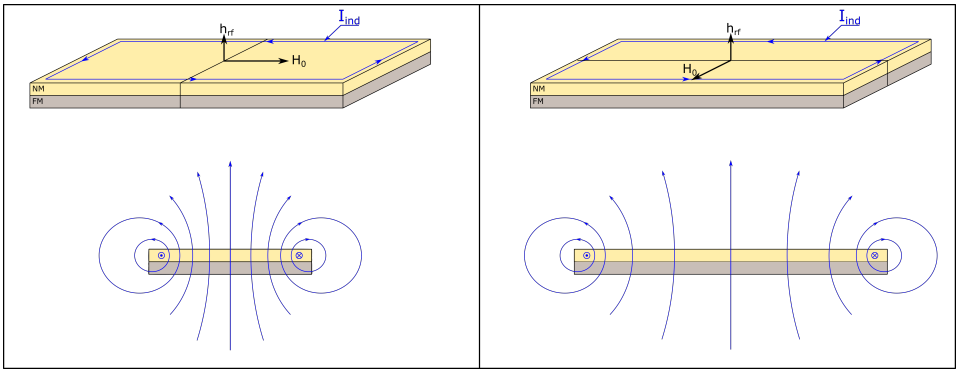

Figure 5.12: (Top) Illustration of eddy current induction in rectangular FM/NM bilayer structures when directing an RF magnetic field along the thin film normal. Induced currents are assumed to primarily flow along the edges of the structure. (Bottom) Sketch of induced magnetic field components normal to the applied static field for a static field oriented along the short and long axis of the sample.

ated magnetic fields is therefore expected to reflect the symmetries of the sample geometry. While eddy current excitations will result in both the Py and Au thin film layer, the current density is expected to be greater in Au due to differences in conductivity [29, 38]. Even though induction in the Py alone has been shown to significantly affect FMR, phase shifted eddy current fields will be considered to primarily originate from currents in the Au layer in the following discussion. Figure 5.12 illustrates the anticipated current flow along with a cross sectional sketch of induced magnetic field components oriented at right angles to the applied static field, considered field directions here being along the short and long axis of the sample. As shown, eddy current induction in the Au thin film will give rise to inhomogeneous phase shifted fields with components both in and out of the Py thin film plane. In-plane eddy current field components are also assumed to be oriented primarily along the short sample axis when the aspect radio differs from unity.

As discussed in Flovik et.al's initial work on this topic [10], the rotationally dependent FMR response of rectangular bilayer structures may be explained qualitatively by considering the spatial orientation of eddy current fields with respect to the static field direction. In section 2.4.3 it was found that for weak RF magnetic fields, the RF field component must be oriented at right angles to the static field for it to contribute to the effective driving field. While out of plane components will contribute regardless of static field orientation, the contribution from in-plane field components will be affected by the relative field alignment. As the right half of Figure 5.12 illustrates, a static field orientation along the short sample axis will result in a minimal effective field contribution from in-plane field components as a small fraction of the sample is exposed to these fields. When the static field is rotated towards the sample long axis the in-plane contribution to the driving field is expected to gradually increase due to an increasing fraction of the sample being

influenced by in-plane field components. This is in agreement with experimentally observed trends as FMR lineshapes become increasingly distorted when the static field is rotated from the short axis of the sample to the long.

To further discuss the observed FMR response in rectangular bilayer geometries the model derived in chapter 3 is considered. In doing so the lineshape amplitude A is expected to follow

$$A \propto \omega \Delta H |\kappa| \Bigg[h_{rf} V_{FM} + \int_{V_{FM}} h^x_{ind}(\mathbf{r}) cos(\phi_x(\mathbf{r})) dV - \frac{\eta_{xy}}{\eta_{xx}} \int_{V_{FM}} h^y_{ind}(\mathbf{r}) sin(\phi_y(\mathbf{r})) dV \Bigg] \tag{5.4}$$

where $\eta_{xy}/\eta_{xx} \approx 3.3653$ corresponds to the curve fit correction coefficients introduced in section 2.4.3. As previously discussed, the first term corresponds to the ideal FMR amplitude response in the absence of eddy current field interactions and the second term to the perturbation introduced by phase shifted eddy current field components oriented along the sample plane normal. The third term is here expected to describe the influence of in-plane field interactions on the FMR lineshape amplitude. To probe the implications of this third term the symmetry of induced eddy current fields is considered. As Figure 5.12 illustrates a closed loop current density along the sample edge will give rise to a symmetric magnetic field distribution, such that

$$h^y_{ind}(-\mathbf{r}) = -h^y_{ind}(\mathbf{r}) \tag{5.5}$$

This implies that the third term of equation (5.4) integrates to zero as symmetry demands an equal phase shift at opposite sides of the sample. The proposed model for the detector signal response thus fails at describing the FMR response of rectangular FM/NM bilayer structures as the resulting expression predicts the amplitude to be independent of the static field orientation.

To understand this lack of coherence between the presented model and experimental results one must recall the primary approximations made in its derivation. As discussed in chapter 3 the basis for both the presented model and the model applied in Flovik's initial work [10] is that one may describe the magnetodynamics of the system using the dynamic susceptibilities derived in section 2.4.3. As these susceptibilities were derived while assuming all magnetic field components to be homogeneous the modeled magnetic response does not necessarily correspond to excited magneto-dynamical modes in a system subject to inhomogeneous RF magnetic fields. This confirms that a numerical model is required to fully explain the interplay of applied RF field components and induced eddy current fields in FM/NM thin film structures.

While the presented model fails to provide an exact global magneto-dynamical description of the system, it could potentially describe the dynamics locally in a

qualitative manner. As Figure 5.12 illustrates, the in-plane magnetic field intensity is expected to be strongest directly below induced eddy currents. When assuming the density of these currents to primarily be located along the sample sides a highly localized in-plane field distribution is expected. Due to the close proximity between induced currents and the FM/NM interface the strength of these fields could potentially exceed that of the applied pumping field and thus locally dominate the effective driving field. In this event independent regions of FMR could result, the sides of the sample being dominated by a phase shifted in-plane driving field and the center region by the superposition of the applied RF field and out-of-plane eddy current field components. The separation into separate FMR domains could imply a decoupling of the side regions dominated by the in-plane driving fields. This would prevent interference between these regions, thus preventing the cancellation of in-plane signal contributions. If one now assumes the two regions to provide the same contribution to the FMR detector signal, equation (5.4) could be rewritten in terms of the contribution from one such region;

$$A \propto \omega \Delta H |\kappa| \Bigg[h_{rf} V_1 + \int_{V_1} h^x_{ind}(\mathbf{r}) cos(\phi_x(\mathbf{r})) dV \\ - 2\frac{\eta_{xy}}{\eta_{xx}} \int_{V_2} h^y_{ind}(\mathbf{r}) sin(\phi_y(\mathbf{r})) dV \Bigg] \tag{5.6}$$

V_1 here being the volume of the FMR domain dominated by the applied RF field, whereas V_2 corresponds to the in-plane dominated FMR volume located on the positive side of the y axis when defining the coordinate system according to Figure 5.12. As $h^y_{ind}(\mathbf{r})$ will be negative in the chosen domain volume, the integrand in the third term will be a positive entity as $\phi \sim -\pi$ is still assumed. The third term of equation (5.6) is therefore expected to grow increasingly negative when rotating the static field towards the long axis of the sample due to the resulting increase in h^y_{ind}. This is in agreement with experimentally observed trends, as the amplitude A is seen to diminish and eventually change sign during static field rotation. If equation (5.6) indeed provides an approximate description of the system dynamics the observed change in sign indicates that the system becomes increasingly dominated by in-plane field components, this implying $h^y_{ind} > h_{rf}$. It should also be noted that similar modifications to the expression for β would result in an increasingly positive numerator and a denominator described by equation (5.6). As such, the stated assumptions also agree qualitatively with the observed trends in lineshape asymmetry as it predicts the observed divergence. While the modified version of the FMR response model successfully replicates some aspects of observed FMR trends, it is based on highly speculative assumptions and should thus be verified numerically.

To further study the eddy current field interaction, the area of rectangular bilayers was varied to vary the magnetic flux acting on the sample. Figure 5.13 illustrates extracted FMR absorption curve parameters for samples of dimensions 0.5xLmm, L here being varied from 0.5 to 3.7, when directing the static magnetic field along

the short, $\theta = 0°$, and long, $\theta = 90°$, sample axis[3]. As shown in Figure 5.13 (a) a static field alignment along the short axis yields an increasing amplitude A for increasing sample area, whereas a decrease and eventual sign change is observed for a 90° field orientation. Furthermore, Figure 5.13 (c) illustrates a weak area dependence in the lineshape asymmetry parameter β for a 0° magnetic field alignment, whereas a significant dependence is observed for a 90° orientation. These trends are in agreement with the previous discussion regarding in-plane field contributions to the effective driving field and its dependence on static field orientation. When directing the static field along the short axis a minimum contribution from h_{ind}^{y} is expected, this leaving mostly contributions from h_{rf} and h_{ind}^{x}. As such, it is not unexpected that the corresponding area dependence of extracted FMR parameters resembles that of uncapped circular Py samples, for which a similar field configuration was assumed. When directing the static magnetic field along the long sample axis in-plane eddy current field components will start contributing to the driving field. As shown, this results in a departure from the previously described trend even for small rectangular samples, thus indicating that the dynamics of the system rapidly becomes dominated by in-plane field components. This could potentially be explained by a local in-plane amplification of the applied pumping field due to the close proximity between induced eddy currents and the FM/NM interface. The observed dominance of in-plane eddy current field components could potentially be of technological importance as it could be exploited to locally phase shift the magneto-dynamical response of a ferromagnetic domain relative to domains not influenced by in-plane eddy current fields. This trait could prove useful when incorporating magnetic devices on the same chip. Furthermore, the field coupling between an NM loop/sheet and an underlying FM domain is tunable as it depends on the orientation of the NM structure relative to applied static magnetic field. The area of incorporated NM loops/sheets could also be varied to tune the strength of this interaction.

Apart from noted trends in A and β the FMR absorption curve linewidth also shows an unexpected dependence on sample area. As illustrated in Figure 5.13 (d) an intermediate linewidth peak is observed for small sample sizes when directing the static field along the long axis, which could signifying an increase in damping. As a physical explanations for this phenomena has yet to be found the observed trend is merely noted.

In addition to the considered 0.5xLmm bilayer samples a second rectangular sample series of dimensions 1xLmm was analyzed as similar dimensions were used in Flovik et.al's initial study [10]. Figure 5.14 illustrates observed trends in extracted FMR parameters for said samples. When comparing these trends to results obtained for 0.5xLmm bilayers one may note that the increase in width had a significant impact on all recorded FMR lineshape parameters. As Figure 5.14 (a) illustrates,

[3]Due to sample alignment problems in the FMR setup the outup goniometer angle did not correspond to the angle enclosed by the static field and the sample short axis. In extracting the data presented in Figure 5.13 $\theta = 0°$ was instead defined by the field orientation producing the maximum value in lineshape amplitude A

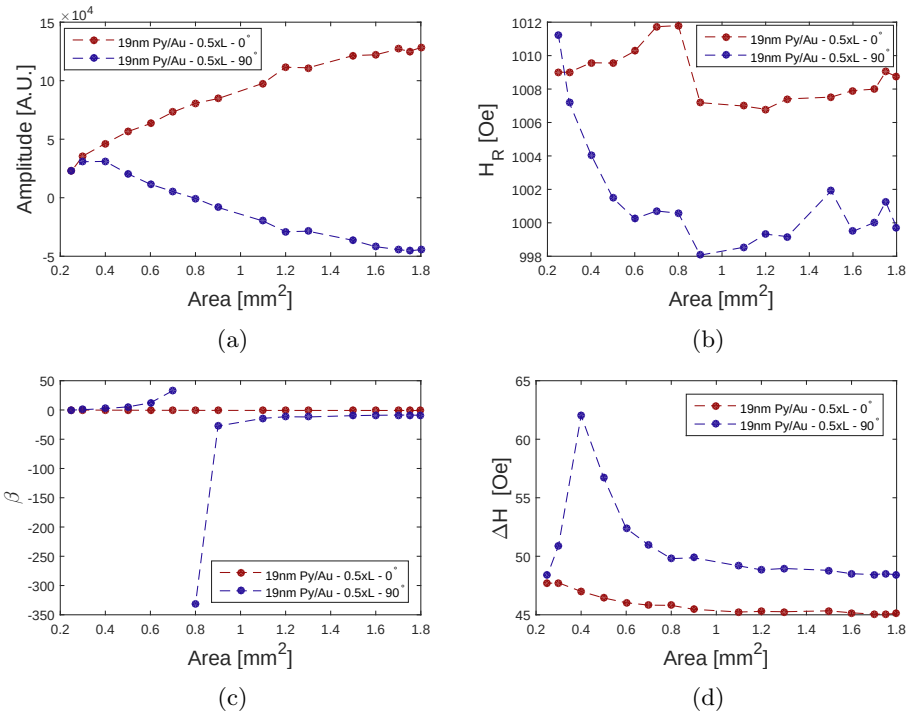

Figure 5.13: Extracted FMR parameters for rectangular bilayer geometries of dimensions 0.5xLmm where L is varied from 0.5mm to 3.6mm. $\theta = 0°$ here corresponds to a field orientation along the sample short axis whereas $\theta = 90°$ to a field orientation along the long axis.

the lineshape amplitude of 1xLmm samples is less influenced by the orientation of the static field (similar trends are seen for 0° and 90° as compared to the large variations seen in 0.5xLmm samples), which indicates a diminished influence from in-plane eddy current field components. This reduced influence is further emphasized in the lineshape asymmetry plots of Figure 5.14 (c). As shown, a 90° field alignment still results in significantly asymmetric lineshapes, though to a lesser degree as indicated by the absent β divergence. The observed trends in lineshape asymmetry for a 0° field alignment also deviates from previous results in that a positive shift is observed. These discrepancies contradict intuition as an increased area should result in stronger currents. This should in turn enhance the magnitude of in-plane field components and consequently its influence on FMR lineshapes.

To explain these trends the spatial distribution of induced currents must again be considered. As previously discussed the induced current density is expected to be localized primarily along the sides of the sample, this resulting in a highly localized in-plane field distribution. While an increased width should enhance the magnitude of these localized field components[4], the corresponding reduction in sample aspect ratio will also increase the fraction of the sample not influenced by these fields. As such, the signal contribution from regions dominated by in-plane field effects will constitute a lesser fraction of the total detector signal, thus yielding what appears to be a weakened eddy current field interaction. To further illustrate this point Figure 5.15 presents a comparison of $B = A\beta$ amplitudes for the two sample widths. As illustrated, an approximately continuous increase in the dispersive susceptibility amplitude is observed, which according to the presented model implies a continued increase in in-plane field interactions. This supports the assumption of a highly localized eddy current field distribution as a reduction in β is observed despite this increase.

As previously mentioned, Flovik et.al's initial study of eddy current effects in FMR considered rectangular bilayers prepared by scribing FM/NM thin film bilayers into 1xLmm rectangles [10]. As in this project the corresponding FMR analysis was performed using the same Bruker Elyxis EPR setup and the data analyzed by curve fitting the obtained FMR data to a functionally identical expression. In these experiments a similar divergence as seen in Figure 5.13 (c) was reported for bilayer lengths exceeding 3mm. This does not correspond to the trend observed in the 1xLmm bilayers studied in this thesis. Furthermore, no significant perturbations in FMR linewidths were reported in Flovik's study, contrary to the trends observed in this work. These discrepancies may be a result of differences in FM and or NM film thickness. Edge roughness effects due to scribing could also reduce the effective width of the sample.

An increase in rectangular bilayer width from 0.5mm to 1mm was also observed

[4] An increase in width will increase the area of the sample. This will in turn result in a larger net magnetic flux acting on the sample which should result in stronger currents. As such, an increased width should yield stronger magnetic fields.

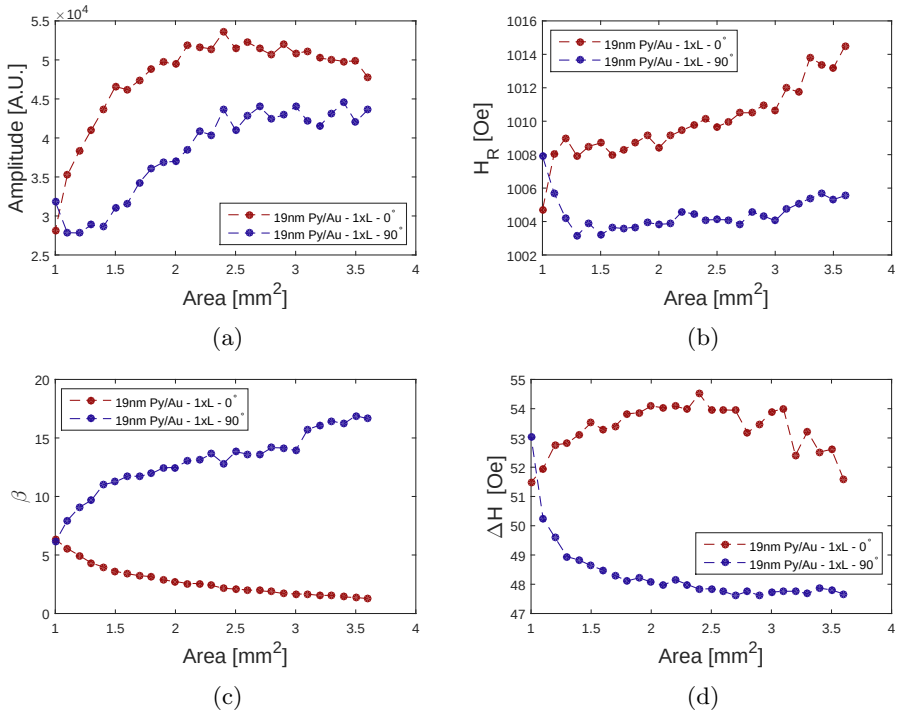

Figure 5.14: (a-d) Extracted FMR parameters for rectangular bilayer geometries of dimensions 1xLmm where L is varied from 0.5mm to 3.6mm. $\theta = 0°$ here corresponds to a field orientation along the sample short axis whereas $\theta = 90°$ to a field orientation along the long axis. $\theta = 0°$ here corresponds to a field orientation along the sample short axis whereas $\theta = 90°$ to a field orientation along the long axis.

to have a significant impact linewidth. Figure 5.14 (d) illustrates the observed linewidth trend when varying the length of a 1xLmm bilayer. As shown, the linewidth is larger for a static field oriented along the sample short axis, as compared to a 90° alignment. This contradicts the trend observed in 0.5xLmm samples where the opposite dependence was observed. The observed increase in linewidth for small sample sizes is also no longer observed. An explanation for these variations has not been found.

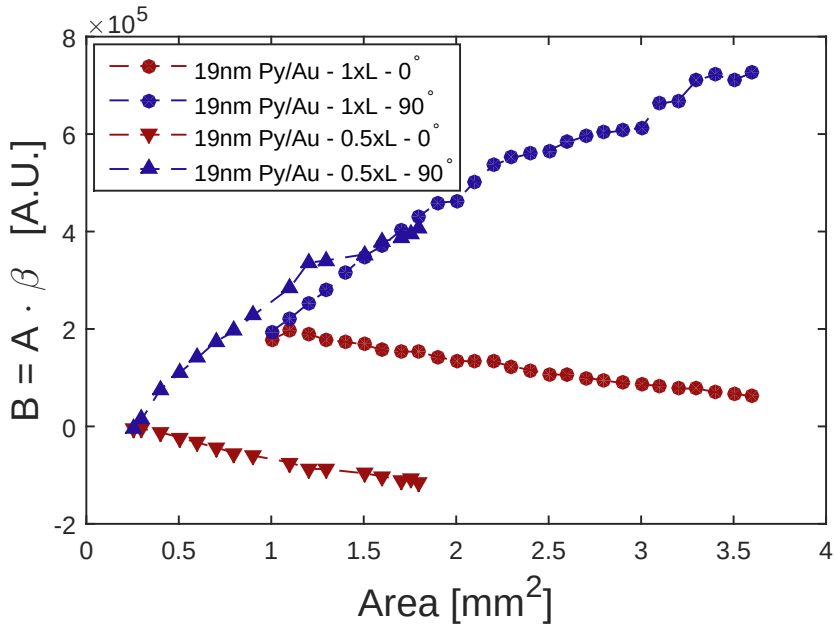

Figure 5.15: A comparison of the dispersive susceptibility amplitude B for 0.5xLmm and 1xLmm rectangular bilayers. $\theta = 0°$ here corresponds to a field orientation along the sample short axis whereas $\theta = 90°$ to a field orientation along the long axis.

5.2.4 Circular Py/Au Thin Film Structures

As previously mentioned, efforts were made to develop a COMSOL Multiphysics model to simulate the distribution of induced eddy currents and associated magnetic fields. To reduce the complexity of these simulations a 2D axi-symmetric formalism was employed, in which all physical entities were assumed to obey rotational symmetry. Circular FM/NM bilayer structures of varying radius were therefore analyzed to provide a physical system to which numerical results could be compared.

While the circular symmetry of the considered bilayer system does simplify numerical simulations, the qualitative analysis of obtained experimental results becomes less straight forwards due to differences in symmetries between induced current/-field distributions and the static field. The following section will therefore merely describe the observed trends for this sample series as a comparison to numerical results could not be achieved. In total, two circular FM/NM sample series were analyzed by FMR spectroscopy during the course of this thesis, one fabricated during the masters pre-project and one prepared in parallel with the circular Py reference samples. FMR results obtained from both sample series are compared in Figure 5.16 for an RF field orientation along the thin film normal. As shown, the two circular FM/NM samples display similar trends in all parameters, this providing some indication of the repeatability of conducted FMR experiments. Observed discrepancies between the two sample series could be explained by the difference in measured thickness.

The FMR lineshape amplitude dependence on sample area for investigated circular geometries is plotted in Figure 5.16 (a). As shown, small variations in lineshape amplitude are observed for a sample radii below $R = 0.5$mm. When increasing the sample radius beyond this threshold a marked increase in lineshape amplitude is observed for increasing radii. A similar shift in the lineshape asymmetry dependence on sample size is observed in Figure 5.16 (c). As shown, the β parameter grows increasingly positive with sample area up to a radius of approximately 0.5mm at which point an intermediate maximum is reached. For sample radii beyond this value the lineshape asymmetry is observed to decline. As the underlying physics responsible for this shift is not yet understood no further comment will be given regarding observed trends in A and β.

Apart from noted trends in lineshape amplitude and asymmetry the resonance field position displayed the expected radial invariance, as shown in Figure 5.16 (b). An intermediate peak in the FMR linewidth, as observed in rectangular bilayers of dimensions 0.5xLmm, was also observed for small sample radii.

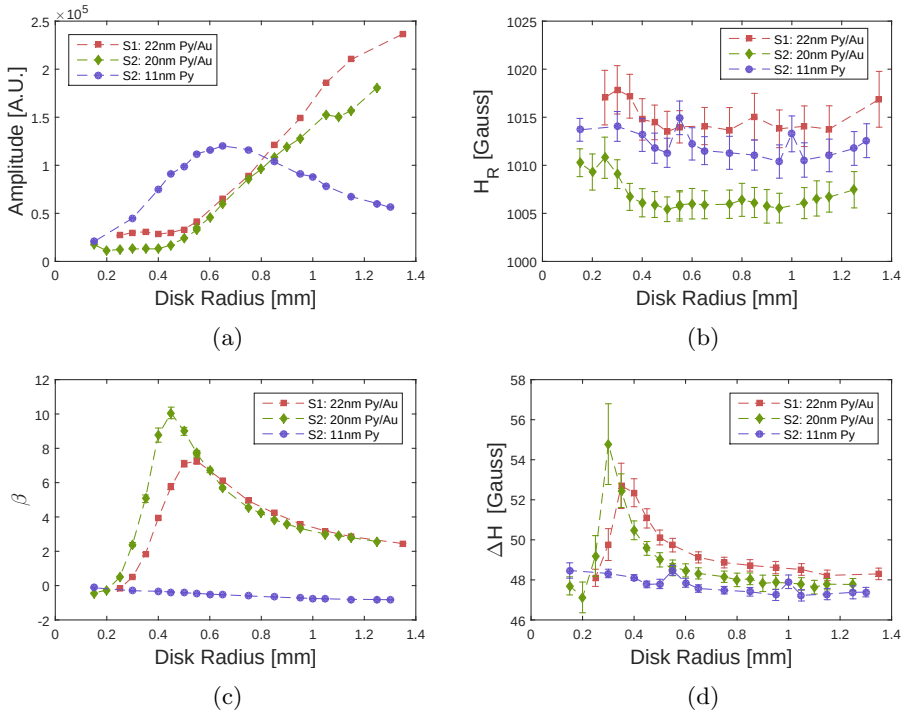

Figure 5.16: Averaged FMR lineshape parameters for disk shaped Py/Au thin film stacks of varying radius when rotating the static field in the thin film plane. Error bars of one standard deviation have been included to give an indication of spread.

Chapter 6

Conclusion

The aim of this thesis was to study the effects of phase shifted eddy current induced magnetic fields on the FMR response of FM/NM thin films structures, and to which degree these interactions could be tuned by varying the sample geometry. To accomplish this a range of 10nmPy/10nmAu thin film geometries were prepared by optical lithography, DC magnetron sputtering and E-beam evaporation. The FMR response of these structures was measured using a commercial EPR setup and the distortion of FMR absorption curves analyzed to probe the eddy current field effect.

The primary results of this study can be summarized:

- An analytical model was developed to interpret obtained FMR absorption data. While similar in functional form to the model developed in Flovik et.al's initial work on this topic the presented model more explicitly links curve fitted parameters to physical entities. The derived model was found to be in qualitative agreement with results obtained for some but not all analyzed test structures.

- Baseline FMR measurements on circular 10nmPy thin film structures of varying radius revealed convincing evidence for significant eddy current field interactions in Py alone. This result could be of importance as Permalloy is among the more common ferromagnetic materials employed in spintronics related research.

- In the study of FM/NM ring structures a significant suppression of the FMR signal amplitude was observed when increasing the width of the NM loop enveloping the inner FM sheet. This suggests that the magnitude of induced eddy current fields could be close to that of the applied rf field for Au loops of sufficient width.

- FMR analysis of rectangular Py/Au samples revealed a rotational dependence in the distortion of FMR lineshapes, this indicating that the magnetization dynamics to a large extent becomes dominated by eddy current field

components directed in the plane of the sample. These observations are in agreement with results reported in Flovik et.al's work [10]. Observed trends in lineshape distortion for varying sample area also suggested the in-plane field interactions to be localized primarily along the edges of studied thin film structures.

6.1 Further Work

To advance the understanding of eddy current field interactions in FM/NM thin film structures further knowledge regarding the distributions of induced eddy currents and associated magnetic fields is required. To first order this would require a numerical model capable of solving the corresponding Maxwell boundary problem in the thin film limit. A model capable of simultaneously solving the LLG equation and Maxwell's equations may also be required as FMR in the FM layer will likely influence induction in adjacent NM structures.

Since Permalloy is among the most commonly used ferromagnetic material systems in spintronics related research further studies should be conducted to better understand when eddy current effects in Py thin films become significant.

To simplify the interpretation of experimental results future experimental studies of eddy current field interactions in FM/NM thin film structures should attempt to limit eddy current excitations in the FM, this allowing one to isolate the FM-NM eddy current field interaction. This could be achieved by employing an insulating ferromagnetic oxide as the FM layer or by using patterned Permalloy thin films rather than a continuous thin film, thus disrupting the paths in which eddy currents may flow.

In the FMR analysis of rectangular FM/NM thin film bilayers observed trends suggest that the dynamics of the system is locally dominated by in-plane eddy current field components, this suggesting a local in-plane field amplification of the applied magnetic rf field. As such, this in-plane field interaction should be isolated and further studied. One way of achieving this would be through FM/NM bilayer structures as illustrated in Figure 6.1.

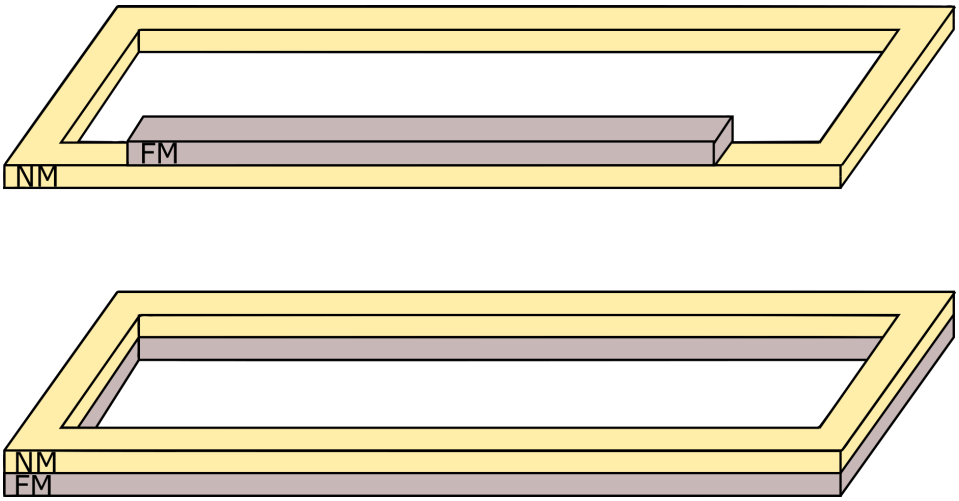

Figure 6.1: Illustration of FM/NM bilayer structures that would isolate the in-plane eddy current field interaction. (Top) structure would be preferable as it provides more control over the field distribution interacting with the FM layer. (Bottom) structure would also isolate the in-plane component, though with contributions from all loop edges during sample rotation, thereby somewhat complicating the analysis of data. This sample type could be manufactured using the mask used in this project by employing the pattern found in sector C2 in a lithography process, followed by the deposition of Py and Au.

Bibliography

[1] Spin transfer nano-oscillators. *Nanoscale*, 5(6), 2013.

[2] G. Binnig and C. F. Quate. Atomic Force Microscope. *Phys. Rev. Lett.*, 56(9), 1986.

[3] S. Blundell. *Magnetism in Condensed Matter*. Oxford University Press Inc, New York, 2006.

[4] B.H. Bransden and C.J. Joachain. *Quantum Mechanics*. Prentice Hall, Harlow, 2nd edition, 2000.

[5] P. Bruno. Physical Origins and Theoretical Models of Magnetic Anisotropy. In *Ferienkurse des Forschungszentrums*, chapter 24. Julich, 1984.

[6] Clairent. AZ5214E Datasheet. `http://www.first.ethz.ch/infrastructure/Chemicals/Photolithography/Data_AZ5214E.pdf`. [Online; accessed 26. December 2014].

[7] D.J. Craik, editor. *Magnetic Oxides*. J.W. Arrowsmith Ltd., Bristol, 1975.

[8] S Fahy, C. Kittel, and Louie S. G. Electromagnetic screening by metals. *Am. J. Phys.*, 56, 1988.

[9] M. Fitzsimmons, T. Silva, and T. Crawford. Surface oxidation of Permalloy thin films. *Phys. Rev. B*, 73(1), 2006.

[10] V. Flovik, F. Macià, A. D. Kent, and E. Wahlström. Eddy current interactions in a Ferromagnet-Normal metal bilayer structure, and its impact on ferromagnetic resonance lineshapes. *J. Appl. Phys.*, 117, 2015.

[11] F. Giesen. *Magnetization Dynamics of Nanostructured Ferromagnetic Rings and Rectangular Elements*. PhD thesis, Hamburg, 2005.

[12] T.L. Gilbert. A Phenomenological Theory of Damping in Ferromagnetic Materials. *IEEE Trans. Magn.*, 40(6):3443–3449, November 2004.

[13] H Glowinski, M Schmidt, I Goscianka, J Dubowik, and J-Ph Ansermet. Magnetic Nanostructures : Impact of Conducting Layers. *Appl. Phys. Lett.*, 116, 2014.

[14] D. J. Griffiths. *Introduction to Quantum Mechanics*. Pearson Prentice Hall, New Jersey, 2nd edition, 2005.

[15] A. G. Gurevich and G. A. Melkov. *Magnetization Oscillations and Waves*. CRC Press, 1996.

[16] J. D. Jackson. *Classical electrodynamics*. Wiley, New York, 1962.

[17] S. I. Kim, M. S. Seo, and S. Y. Park. Resonant cavity mode dependence of anomalous and inverse spin Hall effect. *J. Appl. Phys.*, 115(17), 2014.

[18] C. Kittel. On the Theory of Ferromagnetic Resonance Absorption. *Phys. Rev.*, 73(1948):155–161, 1947.

[19] C. Kittel. *Introduction to Solid State Physics*. Wiley, 8th edition, 2005.

[20] K. Kobayashi, N. Inaba, N. Fujita, Y. Sudo, T. Tanaka, M. Ohtake, M. Futamoto, and F. Kirino. Damping constants for permalloy single-crystal thin films. *IEEE Trans. Magn.*, 45(6):2541–2544, 2009.

[21] M. Krakowski. Eddy current losses in thin circular and rectangular plates. *Arch. für Elektrotechnik*, 64(6):307–311, 1982.

[22] V. V. Kruglyak, S. O. Demokritov, and D. Grundler. Magnonics. *J. Phys. D. Appl. Phys.*, 43(26), 2010.

[23] B. Lenk, H. Ulrichs, F. Garbs, and M. Münzenberg. The building blocks of magnonics. *Phys. Rep.*, 507(4), 2011.

[24] I. S. Maksymov, Z. Zhang, C. Chang, and M. Kostylev. Strong eddy current shielding of ferromagnetic resonance response in sub skin depth thick conducting magnetic multilayers. *IEEE Magn. Lett.*, 5, 2014.

[25] I. S. Maksymov, Z. Zhang, C. Chang, and M. Kostylev. Strong impact of the eddy current shielding on ferromagnetic resonance response of sub skin depth thick conducting magnetic multilayers. *IEEE Magn. Lett.*, 5, 2014.

[26] I.S. Maksymov and M. Kostylev. Broadband stripline ferromagnetic resonance spectroscopy of ferromagnetic films, multilayers and nanostructures. *Phys. E Low-dimensional Syst. Nanostructures*, 69, 2014.

[27] G. De Mey. A Method for Calculating Eddy Currents in Plates of Arbitrary Geometry. *Arch. für Elektrotechnik*, 56, 1974.

[28] O. Mosendz, V. Vlaminck, J. E. Pearson, F. Y. Fradin, G. E W Bauer, S. D. Bader, and A. Hoffmann. Detection and quantification of inverse spin Hall effect from spin pumping in permalloy/normal metal bilayers. *Phys. Rev. B - Condens. Matter Mater. Phys.*, 82(21), 2010.

[29] G. Nahrwold, J. M. Scholtyssek, S. Motl-Ziegler, O. Albrecht, U. Merkt, and G. Meier. Structural, magnetic, and transport properties of Permalloy for spintronic experiments. *J. Appl. Phys.*, 108(1), 2010.

[30] M. Quirk and J. Serda. *Semiconductor Manufacturing Technology*. Prentice Hall, New Jersey, 2001.

[31] J.M. Ribe. 1.4um AZ5214E Image Reversal Process. `https://github.com/NanoLabStaff/nanolab/wiki/Image-reversal`. [Online; accessed 26. December 2014].

[32] B.E.A. Saleh and M.C. Teich. *Fundamentals of Photonics*. Wiley, New Jersey, 2nd edition, 2007.

[33] R. L. Stamps, S. Breitkreutz, J. Å kerman, A. V. Chumak, Y. Otani, G. E. W. Bauer, J. Thiele, M. Bowen, S. Majetich, M. Kläui, I. L. Prejbeanu, B. Dieny, N. M. Dempsey, and B. Hillebrands. The 2014 Magnetism Roadmap. *J. Phys. D. Appl. Phys.*, 47(33), 2014.

[34] J. Stöhr and H. C. Siegmann. *Magnetism - From Fundamentals to Nanoscale Dynamics*. Springer, Berlin, 2006.

[35] S.V. Vonsovskii, editor. *Ferromagnetic Resonance*. Pergamon Press, Oxford, 1966.

[36] G. Woltersdorf. *Spin pumping and two magnon scattering in magnetic multilayers*. PhD thesis, Simon Fraser University, 2004.

[37] L. Yin, D. Wei, N. Lei, L. Zhou, C. Tian, G. Dong, X. Jin, L. Guo, Q. Jia, and R. Wu. Magnetocrystalline Anisotropy in Permalloy Revisited. *Physical Review Letters*, 97:067203, August 2006.

[38] T. Zychowicz, J. Krupka, and J. Mazierska. Measurements of conductivity of thin gold films at microwave frequencies employing resonant techniques. *Asia-Pacific Microw. Conf. Proceedings, APMC*, 1, 2006.

Appendix A

Power dissipation of time harmonic EM fields

The power dissipation of electromagnetic fields can be found from Maxwell's equations, which may be expressed according to

$$\nabla \times \mathbf{E} = -\frac{\partial \mathbf{B}}{\partial t} \tag{A.1}$$

$$\nabla \times \mathbf{H} = \frac{\partial \mathbf{D}}{\partial t} + \mathbf{J} \tag{A.2}$$

where the listed field quantities **E**, **D**, **H**, **B** and **J** are the electric-, displacement- and magnetic field, the magnetic flux density and current density respectively. By scalar multiplying equation (A.1) by $\mathbf{H}^*$ and the complex conjugate of equation (A.2) by **E** and subtracting the two expression the following is obtained:

$$\mathbf{E} \cdot \nabla \times \mathbf{H}^* - \mathbf{H}^* \cdot \nabla \times \mathbf{E} = \mathbf{E} \cdot \frac{\partial \mathbf{D}^*}{\partial t} + \mathbf{H}^* \cdot \frac{\partial \mathbf{B}}{\partial t} + \mathbf{E} \cdot \mathbf{J}^* \tag{A.3}$$

Using the vector identity $\nabla \cdot (\mathbf{A} \times \mathbf{B}) = \mathbf{B} \cdot (\nabla \times \mathbf{A}) - \mathbf{A} \cdot (\nabla \times \mathbf{B})$ and the divergence theorem one may write equation (A.3) as

$$-\frac{1}{2} \oint_s (\mathbf{E} \times \mathbf{H}^*) \cdot d\mathbf{s} = \frac{1}{2} \int_V (\mathbf{H}^* \cdot \frac{\partial \mathbf{B}}{\partial t} + \mathbf{E} \cdot \frac{\partial \mathbf{D}^*}{\partial t} + \mathbf{E} \cdot \mathbf{J}^*) dV \tag{A.4}$$

where V is a volume enclosed by the surface s. The integrand on the left hand side of equation (A.4) is the complex Poynting vector

$$\mathbf{S} = \frac{1}{2} \mathbf{E} \times \mathbf{H}^* \tag{A.5}$$

which describes the direction and magnitude of electromagnetic power flow [32]. The left hand side of equation (A.4) therefore describes the power flow through s whereas the right hand side is interpreted as the power absorbed within the volume

V enclosed by s. To find the time average power absorbed in a sample of volume V the identity [32]

$$\langle \mathbf{S} \rangle = \frac{1}{2} \Re\{\mathbf{E} \times \mathbf{H}^*\} \tag{A.6}$$

may be applied, where the time average Poynting vector is expressed by the real component of the complex Poynting vector. Applying equation (A.6) to equation (A.4) yields

$$\bar{P} = -\oint_s \langle \mathbf{S} \rangle \cdot d\mathbf{s} = \int_V \underbrace{\frac{1}{2} \Re\{\mathbf{H}^* \cdot \frac{\partial \mathbf{B}}{\partial t}\}}_{\bar{\rho}_M} + \underbrace{\frac{1}{2} \Re\{\mathbf{E} \cdot \frac{\partial \mathbf{D}^*}{\partial t}\}}_{\bar{\rho}_D} + \underbrace{\frac{1}{2} \Re\{\mathbf{E} \cdot \mathbf{J}^*\}}_{\bar{\rho}_J} dV \tag{A.7}$$

The terms on the right hand side of equation (A.7), denoted by $\bar{\rho}_M$, $\bar{\rho}_D$ and $\bar{\rho}_J$, represent the time averaged power per volume dissipated through magnetic, dielectric and joule loss respectively.

Appendix B

Photo Mask

To define relevant bilayer geometries a mask intended for optical lithography was designed during the masters pre-project leading up to this thesis. This appendix will present the layout of the mask along with included supporting structures. A brief description of designed bilayer geometries is also given.

The designed mask was manufactured by the Ångström microstructure laboratory in the form of a soda lime glass mask with a chromium pattern. The resolution of the designed chromium pattern was 1µm while the minimum feature size of the pattern itself was 5µm.

B.1 Mask Design

As described in section 4.4.3, analyzed FM/NM bilayers were mounted at the end of a cylindrical quartz rod before loading them into the microwave cavity. The primary constraint in designing relevant bilayer geometries was therefore that the silicon dies supporting the thin film structures fit at the end of this rod. Since the mounting rod had a diameter of approximately 5mm die size were chosen accordingly; rectangular bilayers were supported by 1.6x4mm rectangular silicon supports whereas circular geometries were supported by 3x3mm dies.

To simplify the fabrication of thin film structures, sample types sharing the same die size and fabrication procedure were arranged in arrays. Scribe marks were added along array edges to simplify the alignment of the automated scriber, thus enabling the accurate separation of samples produced on the same silicon wafer. Other supporting structures include alignment marks enabling precise alignment of the photomask to previously deposited thin film geometries. Figure B.1 shows the mask layout where arrays containing different sample types are divided into sectors whereas Figure B.2 illustrates bilayer samples corresponding to the mask patterns within respective mask sectors. The contents of each labeled sector will be discussed in the following subsections.

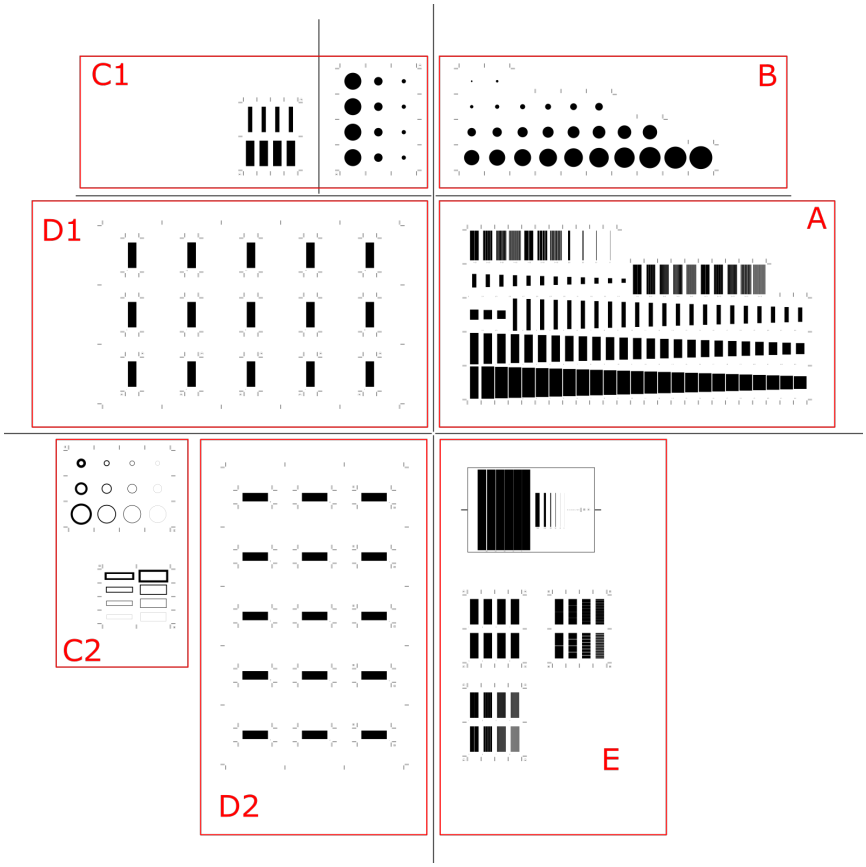

Figure B.1: Photomask layout. Indicated sectors show samples produced on the same silicon support.

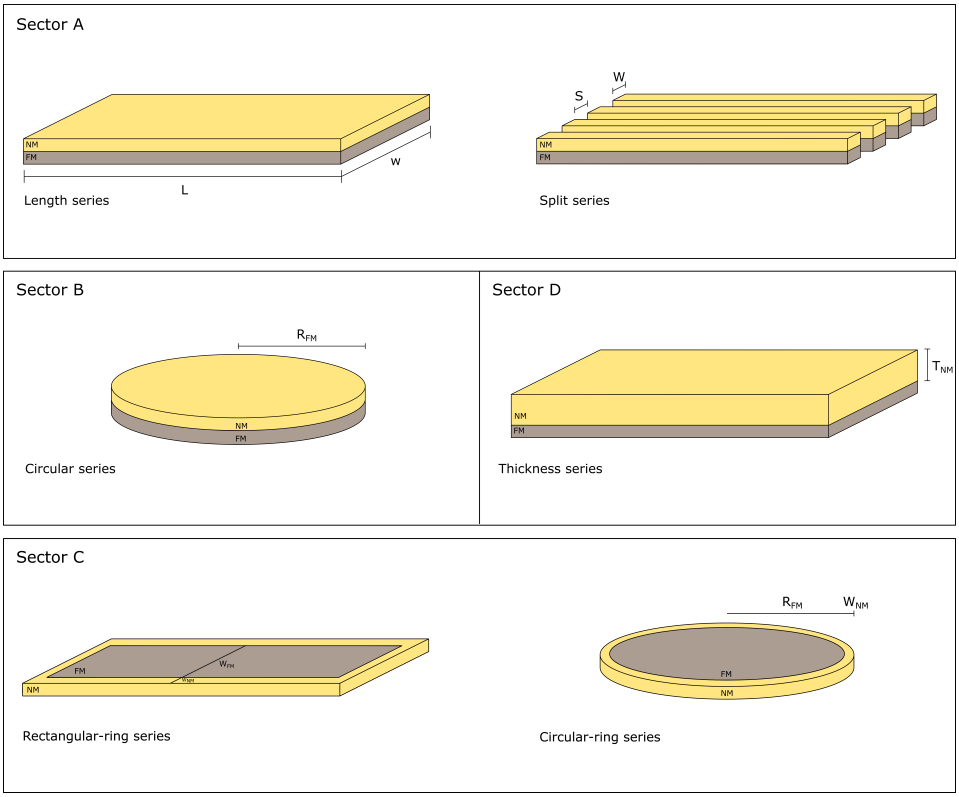

Figure B.2: Bilayer geometries within respective mask sectors. Labels indicate geometric features varied within each sample series. To best illustrate the intended geometry of produced bilayers the thickness of drawn samples was scaled by a factor of approximately 100000.

B.2 Mask Layout

Sector A

As Flovik et.al.s previous work on this topic investigated eddy current effects in rectangular FM/NM bilayers [10], several rectangular structures were designed and implemented in sector A. In total, 87 rectangular structures were included on the mask where the width and length of was varied according to Table B.1. The primary purpouse of these structures was to provide a reference to previous work on this topic.

In addition to rectangular geometries several split rectangular structures were included in sector A, as figure B.2 illustrates. These samples correspond to a 1x3.5mm rectangular thin film structures split along their length into progressively smaller

Table B.1: Geometric features of inclueded rectangular bilayer structures.

Width[mm]	L_{min}[mm]	ΔL[mm]	L_{max}[mm]	Total number
0.5	0.5	0.1	3.8	34
1.0	1.0	0.1	3.8	29
1.5	1.5	0.1	3.8	24

Table B.2: Geometric features, as labeled in Figure B.2, of included split samples. As the amount of deposited material was kept constant in this sample series (added togeather all segments correspond to a 1x3.5mm rectangular bilayer in volume) the number of segments corresponding to a given segment width W is given by 1000/W

Spacing [um]	W [um]	W [um]	W [um]	W [um]	W [um]
5	500	250	125	63	31
15	500	250	125	63	31
25	500	250	125	63	-
50	500	250	125	-	-

segments of varying separation. The purpose of this sample series was to observe weather disrupting the flow of eddy currents in the metal plane affected the perturbation of FMR lineshapes. The separation of segments was varied to provide information regarding the range of eddy current field interactions. The amount of deposited material was kept constant for all split samples. In total, 17 split samples were included in sector A. The geometric features of these samples are listed in Table B.2

Sector B

Circular mask features were included in sector B to provide a rotationally invariant system in which eddy current field interactions could be studied. This rotational symmetry should in principle simplify the analysis of experimental results. The radius of included circular samples was varied from R=0.1mm to R=1.35mm with a step size of 50µm.

Sector C

Sector C1 and C2 include the first and second mask geometries used in the fabrication of rectangular and disk shaped ferromagnetic thin film structures framed by a metallic ring, as Figure B.2 illustrates. These structures were included to allow one to apply closed form analytic expressions in the approximation of induced field strengths, this greatly simplifying the analysis of obtained results, thus simplifying the extraction of insights from experimental results. In the fabrication of these structures sector C1 was first used to define the lateral geometry of the ferromagnetic structure. Following lift off the pattern confined to sector C2 was aligned to alignment marks defined by C1. In total 12 circular ring structures and 8

rectangular structures were included in this sector. For circular ring structures the inner disk diameter was set to R_{FM}=0.25,0.5 and 1mm whereas inner rectangular structures measured 1x3mm and 0.5x3mm. The outer metal ring surrounding both sample types was varied as W_{NM}=10,50,100 and 250µm.

Sector D

Sectors D1 and D2 contain 1x3mm rectangular geometries. These rectangles were surrounded by two scribing grids allowing one to vary the thickness of the NM film while keeping the FM thickness constant without having to repeat the lithography step for each sample: By confining rectangles within a secondary scribing grid it is possible to first conduct a lift off process using the mask pattern in sector D1 where the fixed FM thickness is deposited in addition to a thin capping layer. If one subsequently applied a secondary lithography layer aligned to the first patter, using the mask patterin in D2, one may scribe the substrate before depositing the remaining NM thin film thickness. This leaves a number of identical small samples of fixed FM thickness, ready for thin film deposition.

Sector E

The primary function of geometries confined to sector E was the optimization of the lithography parameters. These structures contained a range of structures with closely spaced lines. The high line density made it easier to locate sidewall features during SEM cross section microscopy.

Appendix C

Thin film growth parameters

Table C.1: Thin film growth parameters for sample series 1: 10nm Py/10nm Au - Rectangular thin film geometry (Photo mask sector A)

Parameter	**Value**
Fabrication date	Nov. 2014
Chamber pressure	$5 \cdot 10^{-8}$Torr
Argon flow rate	67 ccm
Argon pressure	3mTorr
Pre-sputtering	
Recorded bias voltage	-
Recorded plasma power	-
Sputtering time	60s
Py deposition rate check	
Date of rate check	10.09.2014
Recorded deposition parameters	100W/360V/791mA
Measured deposition rate	0.5Ås^{-1}
Py sputter deposition	
Recorded deposition parameters	100W/365V/276mA
Deposition time	200s
Estimated film thickness	10nm

Table C.2: Thin film growth parameters for sample series 1: 10nm Py/10nm Au - Circular thin film geometry (Photo mask sector B)

Parameter	**Value**
Fabrication date	Nov. 2014
Chamber pressure	$5 \cdot 10^{-8}$Torr
Argon flow rate	67 ccm
Argon pressure	3mTorr
Pre-sputtering	
Recorded bias voltage	-
Recorded plasma power	-
Sputtering time	60s
Py deposition rate check	
Date of rate check	10.09.2014
Recorded deposition parameters	100W/360V/791mA
Measured deposition rate	0.5Ås^{-1}
Py sputter deposition	
Recorded deposition parameters	100W/365V/276mA
Deposition time	200s
Estimated film thickness	10nm

Table C.3: Thin film growth parameters for sample series 2: 10nm Py - Rectangular thin film geometry (Photo mask sector A)

Parameter	**Value**
Fabrication date	10.03.2015
Chamber pressure	$8 \cdot 10^{-8}$Torr
Argon flow rate	67 ccm
Argon pressure	3mTorr
Pre-sputtering	
Recorded bias voltage	353V
Recorded plasma power	50W
Sputtering time	60s
Py deposition rate check	
Date of rate check	10.03.2015
Recorded deposition parameters	100W/357V/281mA
Measured deposition rate	0.5Ås^{-1}
Py sputter deposition	
Recorded deposition parameters	100W/357V/281mA
Deposition time	200s
Estimated film thickness	10nm

Table C.4: Thin film growth parameters for sample series 2: 10nm Py/10nm Au - Rectangular thin film geometry (Photo mask sector A)

Parameter	**Value**
Fabrication date	10.03.2015
Chamber pressure	$9 \cdot 10^{-8}$Torr
Argon flow rate	67 ccm
Argon pressure	3mTorr
Pre-sputtering	
Recorded bias voltage	356V
Recorded power	50W
Sputtering time	60s
Py deposition rate check	
Date of rate check	10.03.2015
Recorded deposition parameters	100W/357V/281mA
Measured deposition rate	0.5Ås^{-1}
Py sputter deposition	
Recorded deposition parameters	100W/357V/281mA
Deposition time	200s
Estimated film thickness	10nm
Au E-beam evaporation	
Deposition rate	5Ås^{-1}
Thickness input	10nm

Table C.5: Thin film growth parameters for sample series 2: 10nm Py - Circular thin film geometry (Photo mask sector B)

Parameter	Value
Fabrication date	11.03.2015
Chamber pressure	$2 \cdot 10^{-8}$Torr
Argon flow rate	67 ccm
Argon pressure	3mTorr
Pre-sputtering	
Recorded bias voltage	358V
Recorded power	50W
Sputtering time	60s
Py deposition rate check	
Date of rate check	10.03.2015
Recorded deposition parameters	100W/357V/281mA
Measured deposition rate	$0.5 Å s^{-1}$
Py sputter deposition	
Recorded deposition parameters	100W/357V/281mA
Deposition time	200s
Estimated film thickness	10nm

Table C.6: Thin film growth parameters for sample series 2: 10nm Py/10nm Au - Circular thin film geometry (Photo mask sector B)

Parameter	Value
Fabrication date	11.03.2015
Chamber pressure	$2 \cdot 10^{-8}$Torr
Argon flow rate	67 ccm
Argon pressure	3mTorr
Pre-sputtering	
Recorded bias voltage	351V
Recorded power	50W
Sputtering time	60s
Py deposition rate check	
Date of rate check	10.03.2015
Recorded deposition parameters	100W/357V/281mA
Measured deposition rate	$0.5 Å s^{-1}$
Py sputter deposition	
Recorded deposition parameters	100W/357V/281mA
Deposition time	200s
Estimated film thickness	10nm
Au E-beam evaporation	
Deposition rate	$5 Å s^{-1}$
Thickness input	10nm

Table C.7: Thin film growth parameters for sample series 3: 10nm Py - Circular/rectangular ring geometry - Layer 1 (Photo mask sector C1)

Parameter	**Value**
Fabrication date	18.04.2015
Chamber pressure	$2 \cdot 10^{-7}$Torr
Argon flow rate	67 ccm
Argon pressure	3mTorr
Pre-sputtering	
Recorded bias voltage	353V
Recorded power	50W
Sputtering time	60s
Py deposition rate check	
Date of rate check	18.03.2015
Recorded deposition parameters	100W/355V/283mA
Measured deposition rate	0.5Ås^{-1}
Py sputter deposition	
Recorded deposition parameters	100W/355V/283mA
Deposition time	200s
Estimated film thickness	10nm

Table C.8: Thin film growth parameters for sample series 3: 3nm Ti/10nm Au - Circular/rectangular ring geometry - Layer 2 (Photo mask sector C2)

Parameter	**Value**
Fabrication date	20.04.2015
Chamber pressure	$7.5 \cdot 10^{-9}$Torr
Pre-sputtering	
Argon flow rate	67 ccm
Argon pressure	3mTorr
Recorded bias voltage	-
Recorded power	-
Sputtering time	60s
Ti E-beam evaporation	
Deposition rate	5Ås^{-1}
Thickness input	3nm
Au E-beam evaporation	
Deposition rate	5Ås^{-1}
Thickness input	10nm

Appendix D

Supplementary data

D.1 AFM thickness measurements

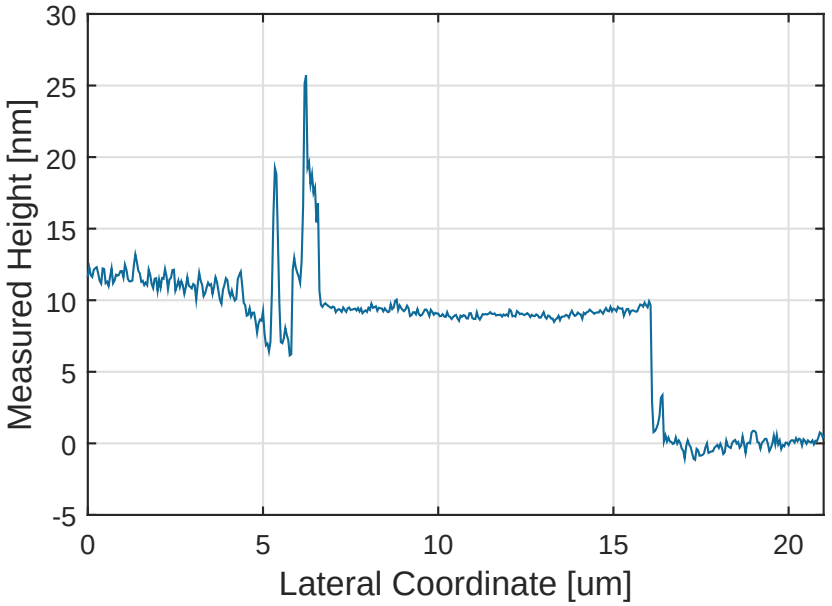

Figure D.1: Recorded AFM thicknesses for a rectangular ring sample. The thickness of the interior Py sheet was approximated to 11nm and the exterior Ti/Au stack measured to a thickness of 10nm.

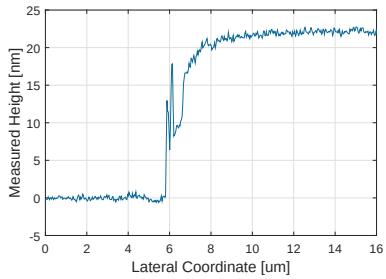

(a) Nov.2014-Circular-Py/Au-22nm

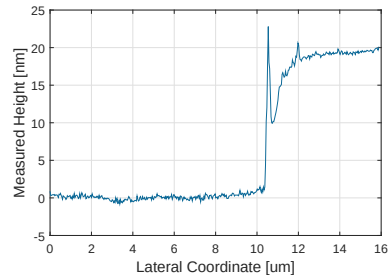

(b) Nov.2014-Rectangular-Py/Au-19nm

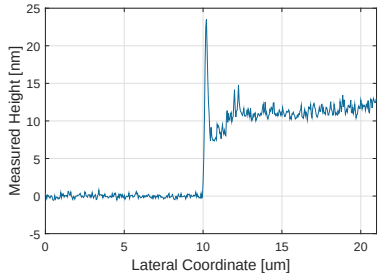

(c) 11.03.2015-Circular-Py-11nm

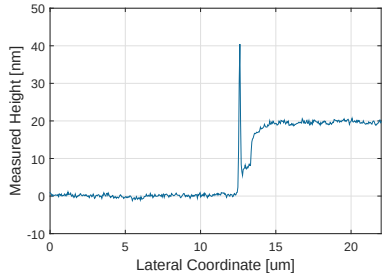

(d) 11.03.2015-Circular-Py/Au-20nm

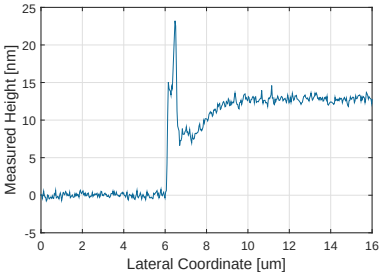

(e) 10.03.2015-Rectangular-Py-13nm

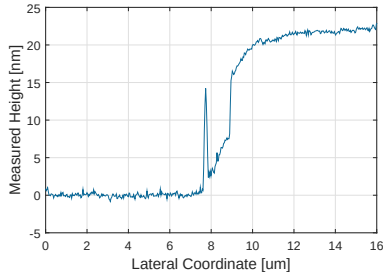

(f) 10.3.2014-Rectangular-Py/Au-22nm

Figure D.2: Recorded AFM thicknesses for circular and rectangular thin film samples. Respective captions list the date of manufactury, sample geometry, composition and approximated thickness.

D.2 Supplementary FMR parameterization data

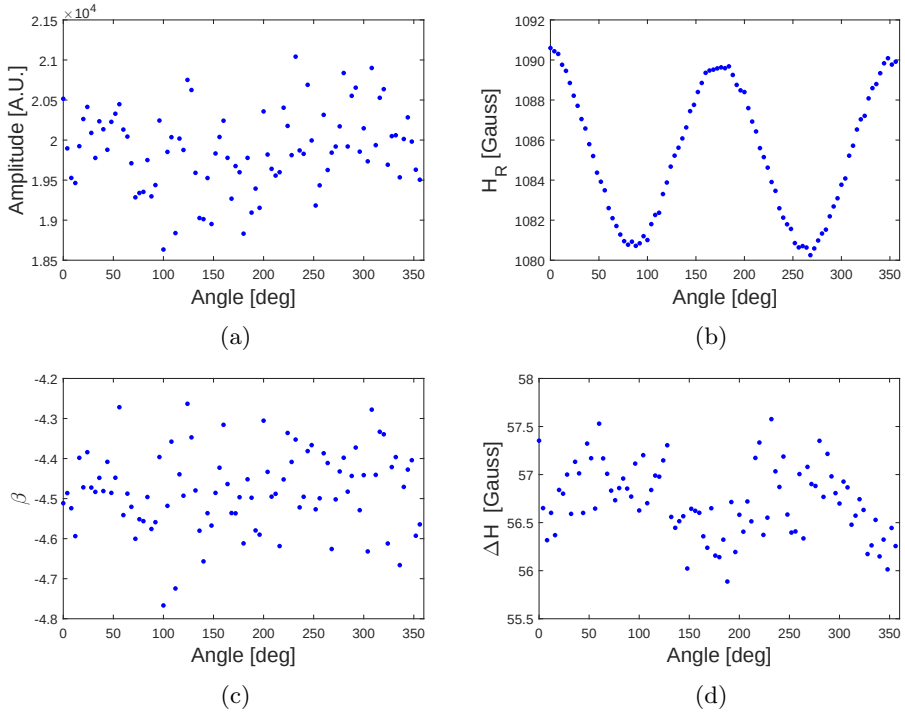

Figure D.3: Extracted FMR lineshape parameters for a circular Permalloy disk of radius 1mm enveloped by a 100mm wide Au/Ti ring when rotating the static field in the thin film plane

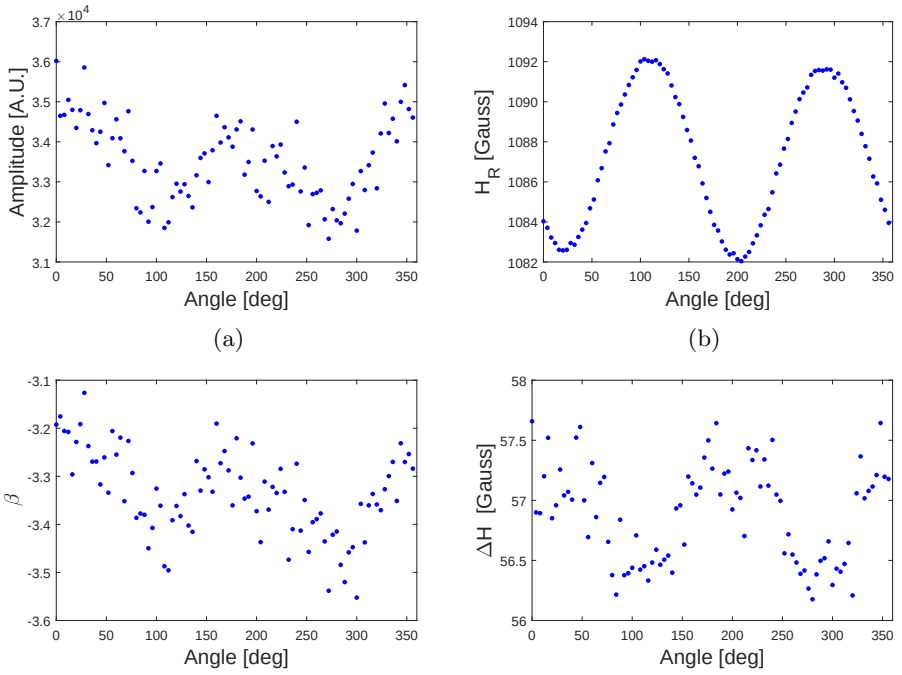

Figure D.4: Extracted FMR lineshape parameters for a 1x3mm rectangular Permalloy sheet enveloped by a 100mm wide Au ring when rotating the static field in the thin film plane

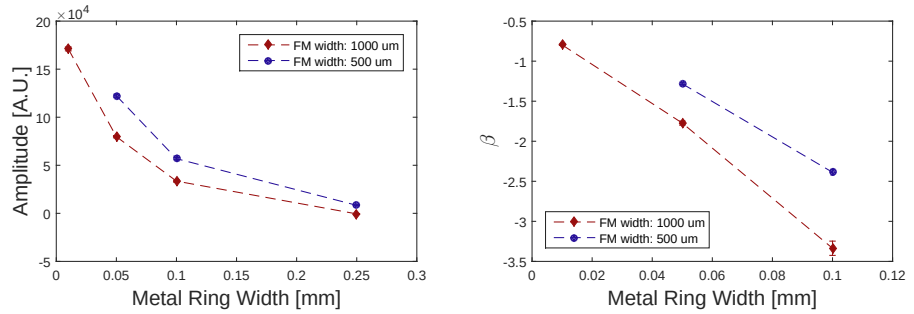

Figure D.5: (a-b) Averaged FMR lineshape amplitude and asymmetry parameter for a Wx3mm rectangular Permalloy sheets enveloped by a Ti/Au ring of varying width

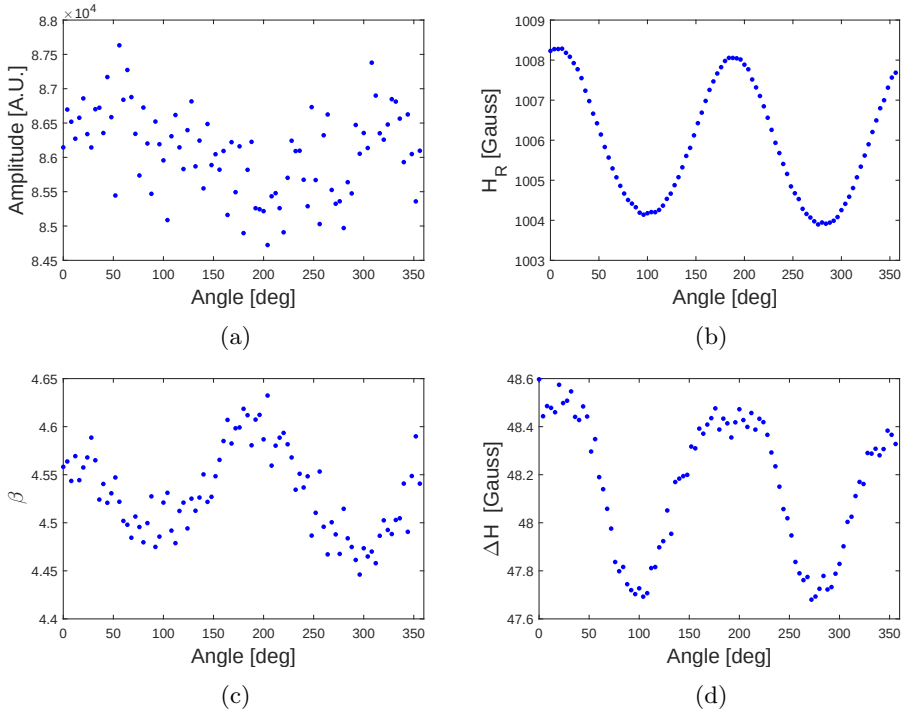

Figure D.6: Extracted FMR lineshape parameters for a 10nm Py/10nm Au disk of radius 0.75mm when rotating the static field in the thin film plane.

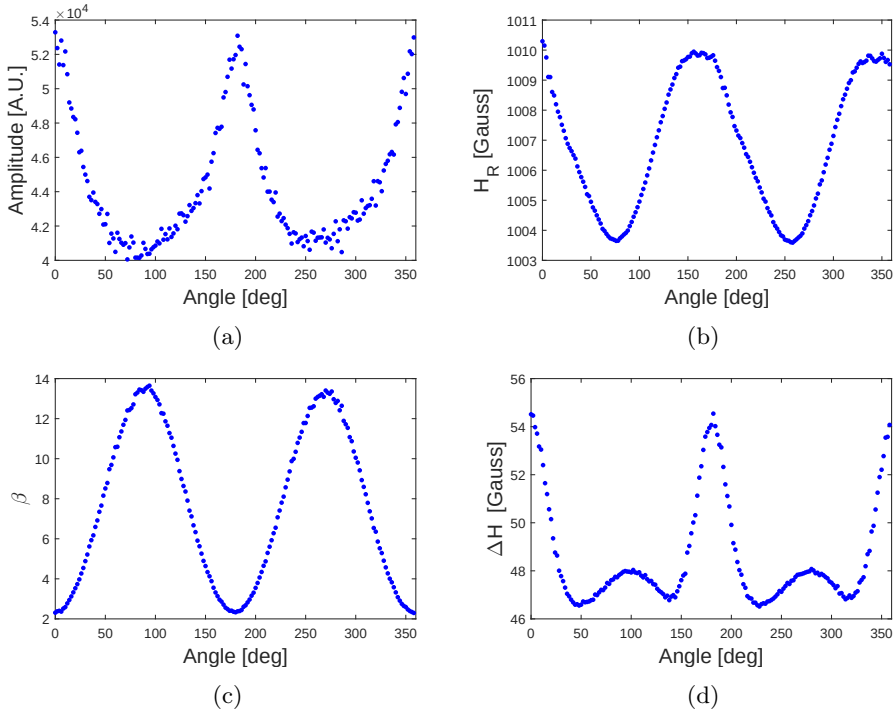

Figure D.7: Extracted FMR lineshape parameters for a 19nm Py/Au rectangular bilayer of dimensions 1x2.3mm when rotating the static field in the thin film plane.

Appendix E

Materials

The following section lists the materials used in the experimental work of this thesis.

E.0.1 Intrinsic Silicon Substrates

To eliminate the possibility of eddy current excitations in the substrate, highly resistive N-type single crystal silicon wafers were chosen to support the studied thin film structures. Specification for the used silicon wafers can be found in Table E.1

Table E.1: Substrate specifications

Supplier	FAB Support AB
Diameter	4" (100 ±0.3mm)
Doping	N-type (Ph)
Orientation	(100) ±0.5°
Resistivity	>5000Ω cm
Thickness	525 ±25µm
Surface	Single side polished

E.0.2 List of Materials

Table E.2: List of used materials

Materials	Manufacturer
Consumables	
Ethanol 96%	Sigma Aldrich
Isopropanol	Sigma Aldrich
Acetone	Sigma Aldrich
Thin film deposition targets	
Permalloy (81%Ni/19%Fe)	Kurt J. Lesker
Gold (E-beam) (19.32g/cm^3)	Kurt J. Lesker
Photolithography	
Photoresist: AZ 5214 E IR	Clarient AG
Developer: AZ 726 MIF	Clarient AG